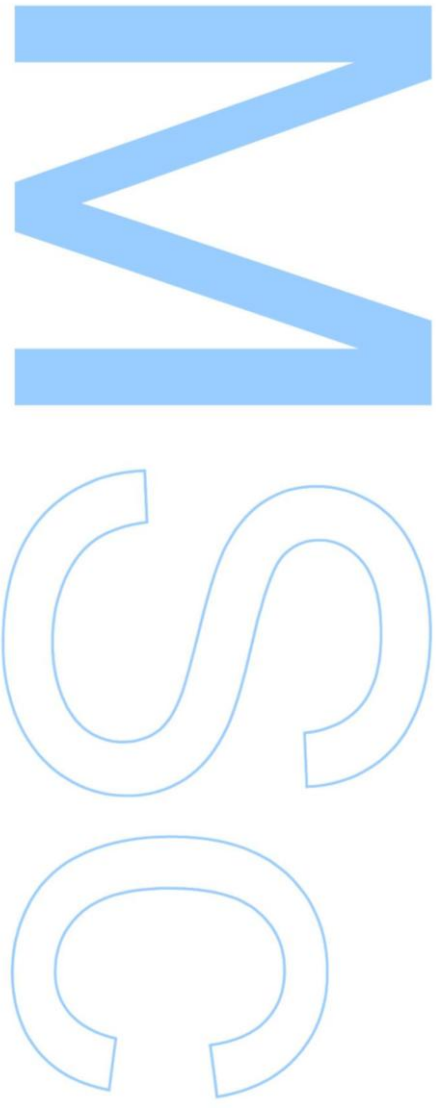
Graphene Nanoplasmonics

Paulo André Dias Gonçalves

Mestrado em Física
Departamento de Física e Astronomia
2014

Orientador
Nuno Miguel Machado Reis Peres, Professor Catedrático, Escola de Ciências da Universidade do Minho

Coorientador
João Manuel Borregana Lopes dos Santos, Professor Catedrático, Faculdade de Ciências da Universidade do Porto





Todas as correções determinadas pelo júri, e só essas, foram efetuadas.

O Presidente do Júri,

Porto, _____/_____/_____

U.PORTO

FACULDADE DE CIÊNCIAS
UNIVERSIDADE DO PORTO

Graphene Nanoplasmonics



Paulo André Dias Gonçalves

Departamento de Física e Astronomia
Faculdade de Ciências da Universidade do Porto
Porto, 2014

Paulo André Dias Gonçalves

Graphene Nanoplasmonics



Thesis submitted to the Faculdade de Ciências da Universidade do Porto in partial fulfillment of the requirements for the degree of Master in Physics

Departamento de Física e Astronomia
Faculdade de Ciências da Universidade do Porto
Porto, 2014

"Science knows no country, because knowledge belongs to humanity, and is the torch which illuminates the world".

Louis Pasteur

Acknowledgments

First of all, I would like to thank my advisors, professor Nuno Peres and professor João Lopes dos Santos for guiding me through this journey. I could not have asked for better tutors, whose invaluable knowledge and enthusiasm about physics I will never forget. In particular, I must offer my sincerest gratitude to professor Nuno Peres, for his continuous support, patience and inspiring dedication. I will always be grateful to have had the opportunity to work with you.

Additionally, I want to acknowledge all the colleagues and friends whom I had the priviledge to meet during my MSc studies at FCUP. Special thanks to Artur Amorim for all the amusing lunches talking about physics and the simple joys of life. Likewise, many thanks to Nuno Rodrigues for his friendship and relaxing conversations.

Furthermore, I would like to express my gratitude towards professor José Carlos Gomes, Fábio Hipólito, and all the people at the Graphene Research Centre in Singapore, for their hospitality and all the good times we have spent during my research stay in Singapore.

Finally, I must thank my parents, brother and grandparents for their affection and for always being there for me. Last, but not least, I am thankful to Inês for her unconditional love, kindness and wholehearted support.

I acknowledge the Calouste Gulbenkian Foundation for finacial support through grant "*Prémio Estímulo à Investigação 2013*", No. 132394.

Resumo

Nos últimos anos, a plasmónica em grafeno tem recebido uma elevada atenção por parte da comunidade científica. Esta área ainda jovem mas em rápido crescimento, que resulta da sobreposição entre a física do grafeno e a plasmónica, centra-se no estudo e exploração de plasmões-polaritões de superfície suportados pelo grafeno (*graphene surface plasmon-polaritons*) (GSPs) com o intuito de controlar interacções luz-matéria e manipular radiação electromagnética à nanoescala.

Nesta tese, depois de introduzirmos os conceitos elementares em plasmónica baseada em metais, procedemos à derivação da relação de dispersão de GSPs tranversos magnéticos (TM) numa monocamada de grafeno. O espectro plasmónico é primeiramente calculado numericamente, sendo posteriormente obtido por meios analíticos em alguns casos limites, aos quais se segue a definição de quantidades físicas relevantes como o comprimento de propagação dos GSPs a o grau de confinamento dos respectivos campos electromagnéticos. Resultados semelhantes são também apresentados para o caso de uma dupla camada de grafeno; neste caso, devido à interação de Coulomb inter-camada entre GSPs em diferentes folhas de grafeno, a relação de dispersão correspondente consiste em dois ramos: um plasmão óptico com dispersão tipo raíz quadrada e um ramo acústico com dispersão linear. De modo a acoplar GSPs a radiação electromagnética propagante, revemos também as técnicas mais comuns para excitar GSPs. Acresce, ainda, o estudo teórico do lançamento de GSPs por um contacto metálico colocado sobre uma folha de grafeno, motivado por um trabalho experimental recente. Finalmente, é apresentada uma descrição detalhada da física fundamental subjacente à excitação de GSPs numa estrutura periódica composta por fitas de

grafeno, bem como a sua dependência em vários parâmetros. De seguida, os resultados teóricos obtidos usando o modelo analítico desenvolvido são comparados com os resultados experimentais publicados na literatura, tendo-se obtido um acordo notável entre teoria e experiência.

Abstract

Over the last few years, graphene plasmonics has been receiving a lot of attention from the scientific community. This still young but rapidly growing field, resulting from the overlap between graphene physics and plasmonics, deals with the investigation and exploitation of graphene surface plasmon-polaritons (GSPs) for controlling light-matter interactions and manipulating light at the nanoscale.

In this thesis, after introducing the elementary concepts in conventional metal-based plasmonics, we move on to the derivation of the dispersion relation of transverse magnetic (TM) GSPs in single-layer graphene. The plasmonic spectrum is first computed numerically and then obtained analytically in some limiting cases, followed by the definition of relevant quantities such as GSP propagation length and a measure of the degree of field confinement. Similar results are also presented for double-layer graphene; in this case, due to the inter-layer Coulomb interaction among GSPs in different graphene sheets, the corresponding dispersion relation consists in two branches: one optical plasmon with square-root dispersion and one acoustic branch with linear dispersion. We also briefly review the most common techniques for effectively exciting GSPs, since they cannot couple directly to free propagating electromagnetic waves. Further, motivated by a recent experimental work, we theoretically study the launching of GSPs by a metallic contact placed on top of monolayer graphene. Finally, a detailed discussion of the physics underlying GSPs excitations in a periodic array of graphene ribbons is presented, and the dependence of the GSP-induced absorption peak on a wide range of parameters is investigated. We then compare the theoretical results yielded by our analytical framework against available experimental

data, having achieved a remarkable agreement between theory and experiment.

Contents

Acknowledgments **iii**

Resumo **v**

Abstract **vii**

List of Figures **xiv**

List of Acronyms **xv**

1 Introduction **1**

1.1 Context 1

1.2 Structure of this thesis 4

2 Electromagnetic Properties of Solids **7**

2.1 Classical Electrodynamics 7

2.1.1 Maxwell's equations 8

2.1.2 Boundary conditions 11

2.2 Drude Model 11

2.3 Graphene for Plasmonics 13

2.3.1 Optical conductivity of graphene 14

3 Surface Plasmon Polaritons at Dielectric-Metal Interfaces **17**

3.1 Single Dielectric-Metal Interface 17

3.1.1 Dispersion relation 18

3.1.2 Propagation length and field confinement 25

3.2 Multilayer Structures: Double Interface 29
3.2.1 Dispersion relation 30

4 Graphene Surface Plasmons 39
4.1 Monolayer Graphene 40
4.1.1 Spectrum of TM GSPs 40
4.1.2 Field profile of GSPs in single-layer graphene 48
4.1.3 A word on TE GSPs 51
4.2 Double-Layer Graphene 52
4.2.1 Dispersion relation 53
4.2.2 Field profile of GSPs in double-layer graphene 57

5 Excitation of Graphene Surface Plasmons 61
5.1 Grating Coupling 61
5.2 Prism Coupling 62
5.3 Near-field Excitation and Imaging of GSPs 64
5.4 Others 66

6 Launching Plasmons using a Metal Contact 67

7 Plasmonics in Periodic Graphene-based Structures 81
7.1 Theoretical Model 82
7.1.1 Setting up the model 82
7.1.2 The scattering problem 85
7.2 Applications and Results 87
7.2.1 Periodic array of graphene ribbons 87
7.2.2 Theory *versus* experiment 94

8 Concluding Remarks 101

A Supplementary Material for Chapter 7 103
A.1 Derivation of the expressions for the transmittance and reflectance 103
A.2 Modes contributing to each resonance 105

Bibliography **108**

List of Figures

2.1 Optical conductivity of graphene 16

3.1 Dielectric-metal interface. 18
3.2 Dispersion relation of TM SPPs at a dielectric-metal interface (zero damping). 21
3.3 Dispersion relation of TM SPPs in air/Ag and SiO_2/Ag interfaces (finite damping). 23
3.4 $\Re\{q\}$ and $\Im\{q\}$ of TM SPPs at an air/Ag interface. 24
3.5 Propagation lengths of SPPs at dielectric/metal interfaces. . . 27
3.6 Penetration depths of the EM fields due to SPPs at an interface between air and silver. 28
3.7 Double DMD/MDM interface. 30
3.8 Dispersion relation of TM SPPs in a thin film. 34
3.9 Electric field profile of SPPs in a double interface: symmetric and antisymmetric modes 35
3.10 Experimentally obtained dispersion curve of SPPs in a thin Al film. 35
3.11 Propagation length of LRSPPs and SRSPPs in Ag thin films. 37

4.1 Graphene between two dielectric media 40
4.2 Dispersion relation of TM GSPs. 43
4.3 Dispersion relation of TM GSPs (finite $\gamma \neq 0$). 44
4.4 Electric (vector) field due to TM GSPs. 50
4.5 Double-layer graphene structure 53
4.6 Dispersion relation of TM GSPs in double-layer graphene. . . 56

4.7 GSPs' electric field corresponding to the optical mode 58
4.8 GSPs' electric field corresponding to the acoustic mode 59

5.1 Configuration for grating coupling. 62
5.2 Diagram of the prism coupling technique. 63
5.3 Infrared nano-imaging of GSPs. 65

6.1 Metal contact on top of graphene. 68
6.2 In-plane electric field due to the contact inhomogeneity. 76
6.3 Intensity plots of the $\mathbf{E}^{2D}$ components. 79
6.4 Electric field lines of $\mathbf{E}^{2D}(x, z)$. 80

7.1 Graphene with a spatially-dependent periodic conductivity. . . 82
7.2 Periodic array of graphene ribbons. 88
7.3 Unit cell of the periodic structure. 89
7.4 Absorbance, transmittance and reflectance of a p-polarized wave through a periodic structure of graphene ribbons. 90
7.5 Dependence of the GSP frequency on the electronic density. . 91
7.6 Dependence of the GSP frequency on the periodicity of the system. 92
7.7 Absorbance of a grid of graphene ribbons for varying θ and d_g/R ratio. 93
7.8 Experimental setup of an array of graphene micro-ribbons. . . 94
7.9 Transmittance change spectrum, $-\Delta T/T_{CNP} = 1 - T/T_{CNP}$: theory and experiment. 96
7.10 Normalized spectra of $-\Delta T$ for arrays of ribbons with different widths: theory and experiment. 98

A.1 Relative contribution of different harmonics to the resonances. 106

List of Acronyms

2D two-dimensional

2DEG two-dimensional electron gas

AFM atomic force microscope

ATR attenuated total reflection

CNP charge neutral point

EELS electron energy loss spectroscopy

EM electromagnetic

GSP graphene surface plasmon-polariton

IR infrared

LDOS local density of states

LRSPP long-range surface plasmon-polariton

LSP localized surface plasmon

SNOM scanning near-field optical microscope

SPP surface plasmon-polariton

SRSPP short-range surface plasmon-polariton

TE transverse electric

THz terahertz

TM transverse magnetic

Chapter 1

Introduction

1.1 Context

Despite the recent burst of interest in plasmonics, plasmon-related effects can be traced back to the turn of the twentieth century through the works of A. Sommerfeld and J. Zenneck on the propagation of electromagnetic waves along the surface of a conductor [1, 2]. Concurrently, in 1902, R. H. Wood reported the observation of anomalous intensity drops in the spectrum of visible light diffracted by a metallic grating, which became known as Wood's anomalies [3]. However, Wood was unable to came up with an interpretation for this phenomenon. The first effort to provide a theoretical explanation was conducted by Lord Rayleigh [4], albeit with limited success, followed by the works of Fano a few decades later [5], which led to subsequent improvements [6]. Some of these breakthroughs took place during the 1950s and 1960s [7, 8], along with the development of the concept of *surface plasmon-polariton* and its excitation using fast electrons [9, 10] and via prism coupling [11, 12, 13].

Surface plasmon-polaritons (SPPs) are electromagnetic surface waves coupled to collective excitations of the conduction electrons, propagating along the interface between a dielectric and a conductor. When this coupled excitations occur in metallic nanostructures, the corresponding non-propagating plasmon-polaritons are generally coined as localized surface plasmons (LSPs).

Notwithstanding, modern plasmonics as we know it emerged in the turn

of the 21st century with the observation, by T. W. Ebbesen *et al*, of an "extraordinary optical transmission through sub-wavelength hole arrays" in a periodically patterned metal film [14]. Shortly after, a theoretical account for the referred experiment was developed invoking the role SPPs [15]. One notable feature of SPPs (and LSPs) modes is that their momentum is larger than light's momentum corresponding to photons with the same frequency [16]. As a consequence, these are bound modes whose fields decay exponentially away from the interface, exhibiting subwavelength confinement and field enhancement (which can be several orders of magnitude) beyond the reach of conventional optics [16, 17, 18]. Thus, plasmonics opened up the possibility for manipulating light and control light-matter interactions at scales well below the diffraction limit, being one of the most promising research topics in the field of nanophotonics and also an important ingredient in the design and implementation of metamaterials [19, 20, 21].

Nowadays, plasmonics plays a leading role towards the miniaturization of photonic structures and circuitry, along with their integration with current semiconductor technologies [22]. As far as telecommunications and/or information processing are concerned, photonics offers high speeds and large bandwidths, but this comes with the cost of bulky components (in comparison to chip-based nanoelectrics); on the other hand, although electronics provides miniaturization and good carrying capacities, its ability to deal with huge amounts of information is limited by the number of connections, resulting in transmission bottlenecks. Therefore, the hybrid nature of SPPs (being half-light, half-matter bosonic quasiparticles, i.e. polaritons) makes them an attractive route to close the gap between optical and electronic circuits, by combining the advantages of both "worlds".

The revival of the field over the past decade was, to a large extent, due to rapid development of nanoscale fabrication techniques and experimental tools, together with the implementation of powerful numerical modelling based on full-wave electromagnetic simulations. These triggered the emergence of a plethora of exciting applications (which are often strong motivators by themselves), such as spectroscopy and biochemical sensing [19, 23, 24], optical tweezers [25, 26], photovoltaics and energy harvesting [27, 28], diagnos-

tics and nanomedicine [29, 30, 31], SPP-based amplifiers and lasers [32, 33], Fourier and transformation optics [34, 35], etc. Yet, the field of plasmonics is far from being exhausted and continues to thrive. Recently, special attention has been given to forefront research topics including ultrafast plasmonics [36], non-linear phenomena with SPPs [37] and quantum plasmonics [38]. The latter studies the quantum properties of SPPs, setting up novel pathways to investigate new fundamental physics and to fuel the prospection for plasmonic devices operating at the quantum regime [39, 40]. Several quantum optics experiments with SPPs have been reported [41, 42, 43, 44].

In the present work, we are concerned with graphene as a plasmonic material – graphene plasmonics [45]. Discovered in 2004 [46], graphene – a two-dimensional (2D) crystal made up of carbon atoms arranged in a honeycomb lattice – has been one of the hottest topics in condensed matter physics, owing to its remarkable electronic, mechanical and optical properties [47, 48]. As in the case of plasmonics, the number of publications on graphene physics has escalated during the past decade. However, the two fields have evolved quite independently up until recently.

Doped graphene is capable of sustaining SPPs [49, 50, 51, 52, 53, 54, 55], which can be actively controlled and tuned through chemical doping or electrical gating almost in real time. This contrasts with conventional metal-based plasmonics, where the tunability is usually limited. Furthermore, graphene surface plasmon-polaritons (GSPs) enable higher levels of spatial confinement and suffer from relatively low losses when compared with traditional plasmonic materials, thereby making graphene an appealing candidate for nanoplasmonics and nanophotonics. Additionally, although the frequency of GSPs scales with momentum as $\sqrt{q}$ like in classic 2DEGs (two-dimensional electron gases), the GSP frequency is proportional to the electronic density as $n_e^{1/4}$, which is specific of graphene (for 2DEG, a $n_e^{1/2}$ scaling is observed instead). This is a direct consequence of the unique electronic properties of graphene, whose electrons behave like relativistic Dirac fermions following a linear dispersion (at low energies in the vicinity of the Dirac point) [48]. Another peculiarity of graphene is its ability to support transverse electric (TE) SPP modes [56], which do not occur in ordinary metal/dielectric structures

[16].

The frequencies of transverse magnetic (TM) GSP typically lie between the terahertz (THz) and mid-infrared regions of the electromagnetic spectrum. While the THz spectral region remains relatively unexplored, THz photonics is becoming an active field of research over the last few years [57]. Here too, graphene plasmonics may contribute to the development of the aforementioned subject [58, 59].

Research on graphene plasmonics is intense and likely to remain one of the hottest topics in nanophotonics in the forthcoming years. In addition, the exploration of the unique properties of graphene surface plasmons may lead to a new gold rush with high impact both in fundamental science as well as in technology and industry, ultimately leading to the appearance of the next generation of devices with tailored optoelectronic properties.

1.2 Structure of this thesis

This thesis is organised as follows. In Chapter 2 we lay down the theoretical foundations of classical electrodynamics and solid state physics, accompanied with a concise introduction to graphene with particular attention given to the description of its dynamical conductivity. Then, in Chapter 3 we review the fundamental properties of SPPs in conventional metal-dielectric interfaces, while introducing key concepts in plasmonics. The study of graphene surface plasmons, which is the main focus of this dissertation, begins in Chapter 4. Here, we investigate the general properties of GSPs in extended monolayer graphene sandwiched between two insulating media and also in double-layer graphene (where the graphene sheets are separated by a core dielectric layer), including the calculation of the corresponding dispersion relations and the computation and plotting of the full vectorial fields in both cases. Along the way, some analytical results in closed-form are obtained by employing some approximations. In Chapter 5 we give some examples of the most popular techniques to bypass the missing momentum (between light and SPPs) and effectively excite GSPs. Chapter 6 is devoted to the investigation of the assisted launching of GSPs in continuous graphene by resonant light

impinging on an infinitely long metal contact localized on top of graphene, thereby making the stripe behave as a dipole antenna. Finally, in Chapter 7, we present an extensive and detailed study of the coupling of free propagating electromagnetic radiation to (localized) GSPs in graphene ribbons, namely in a periodic system formed by a set of graphene micro-ribbons akin to a diffraction grating. After building the theoretical framework, we compare our analytical results against experimental data in order to validate our model.

In this work we have covered many aspects of the physics governing the properties and the nature of SPPs supported by graphene. A number of problems were addressed, ranging from rather generic systems to particular, well-defined problems involving GSPs in graphene-based structures. Throughout this thesis we tried to present the solutions to the above-mentioned problems with a fair amount of detail (yet without prejudice to the readability of the text), with the aim to make this document as self-contained as possible. Special attention was also given to the interpretation and clarity of the results. Therefore, we hope that this dissertation will not only serve as a springboard for any newcomer in graphene nanoplasmonics, but also a valuable tool for the advanced researcher to keep at hand.

Chapter 2

Electromagnetic Properties of Solids

In this Chapter, we lay the foundations which will constitute the framework of the work developed in later Chapters. Here, we shall provide a brief overview on elementary concepts in classical electromagnetism and condensed matter physics.

2.1 Classical Electrodynamics

Nowadays, the quest for a unified theory, commonly known as *"Theory of Everything"*, remains the Holy Grail of Theoretical Physics. The first step towards this end was taken by James Clerk Maxwell, in 1864, with the publication of his famous article entitled "A Dynamical Theory of the Electromagnetic Field" [60]. By unifying electricity and magnetism, Maxwell headed one of the greatest scientific achievements of the 19th century. In fact, classical electrodynamics can be regarded as the first (classical) unified field theory. Today, within the standard model, classical electromagnetism corresponds to a limit of quantum electrodynamics (QED) [61], dubbed by Richard Feynmann as the "jewel of physics" owing to the level of agreement between its predictions and experiment. Still, at macroscopic and mesoscopic scales, provided that the number of photons is large and that momentum and energy

transfers are small, the classical formalism often suffices [62]. This regime is satisfied throughout this work.

2.1.1 Maxwell's equations

In the scope of Maxwell's classical electrodynamics, light is described as an electromagnetic wave in the form of a three-dimensional electromagnetic field. Within this framework, light-matter interactions are governed by Maxwell's equations. In SI units, the macroscopic Maxwell's equations read [62]

$$\nabla \cdot \mathbf{D} = \rho \ , \tag{2.1}$$

$$\nabla \times \mathbf{H} = \frac{\partial \mathbf{D}}{\partial t} + \mathbf{J} \ , \tag{2.2}$$

$$\nabla \times \mathbf{E} = -\frac{\partial \mathbf{B}}{\partial t} \ , \tag{2.3}$$

$$\nabla \cdot \mathbf{B} = 0 \ , \tag{2.4}$$

where $\mathbf{E} \equiv \mathbf{E}(\mathbf{r}, t)$ denotes the electric field, $\mathbf{D} \equiv \mathbf{D}(\mathbf{r}, t)$ the electric displacement, $\mathbf{H} \equiv \mathbf{H}(\mathbf{r}, t)$ the magnetic field and $\mathbf{B} \equiv \mathbf{B}(\mathbf{r}, t)$ the magnetic induction[1]. In turn, $\rho \equiv \rho(\mathbf{r}, t)$ and $\mathbf{J} \equiv \mathbf{J}(\mathbf{r}, t)$ refer to the (free) charge density and current density, respectively, satisfying the continuity equation (charge conservation)

$$\frac{\partial \rho}{\partial t} + \nabla \cdot \mathbf{J} = 0 \ . \tag{2.5}$$

It should be noted that in the case of graphene (or a 2DEG), lying in a $z = const.$ plane, we have

$$\rho = \rho_{\mathrm{2D}} \delta(z) \qquad \text{and} \qquad \mathbf{J} = \mathbf{J}_{\mathrm{2D}} \delta(z) \ , \tag{2.6}$$

at a given time. Limiting ourselves to media that are linear, uniform and isotropic, and also non-magnetic, one can prescribe the following constitutive

[1] Remark: we will refer to $\mathbf{B}$ as being the "magnetic field" multiple times throughout this work, though this is technically inaccurate.

relations

$$\mathbf{D} = \epsilon\epsilon_0\mathbf{E} \ , \tag{2.7}$$

$$\mathbf{H} = \frac{1}{\mu_0}\mathbf{B} \ , \tag{2.8}$$

where ϵ_0 is the electric permittivity of vacuum and μ_0 its magnetic permeability; these relate to the speed of light in vacuum via $c^{-2} = \epsilon_0\mu_0$. The quantity ϵ represents the relative permittivity or dielectric constant. Another important constitutive relation, for conducting materials, is the generalized Ohm's law,

$$\mathbf{J} = \sigma\mathbf{E} \ . \tag{2.9}$$

with σ being a frequency-dependent conductivity. We note that, in general, the linear relationships expressed through equations (2.7) and (2.9) should be understood as

$$\mathbf{D}(\mathbf{r},t) = \epsilon_0 \int d\mathbf{r}'dt'\epsilon(\mathbf{r}-\mathbf{r}',t-t')\mathbf{E}(\mathbf{r}',t') \ , \tag{2.10}$$

$$\mathbf{J}(\mathbf{r},t) = \int d\mathbf{r}'dt'\sigma(\mathbf{r}-\mathbf{r}',t-t')\mathbf{E}(\mathbf{r}',t') \ , \tag{2.11}$$

where ϵ stands now as a function – dielectric function. Equations (2.10) and (2.11) simply state that the value of $\mathbf{D}$ and $\mathbf{J}$ at a given position $\mathbf{r}$ and time t, depends on the value of $\mathbf{E}$ at all positions $\mathbf{r}'$ and times $t' < t$ (to preserve causality) via the response functions $\epsilon(\mathbf{r}-\mathbf{r}',t-t')$ and $\sigma(\mathbf{r}-\mathbf{r}',t-t')$, respectively. Consequently, this accounts for both temporal dispersion and non-local effects in space (spatial dispersion), meaning that the optical response is frequency- and momentum-dependent. While the former is usually evident, the latter can be safely neglected in most cases (as long as the corresponding wavelength is larger than the electron's mean free path).

In Fourier space, the above equations translate to

$$\mathbf{D}(\mathbf{r},\omega) = \epsilon_0\epsilon(\mathbf{r},\omega)\mathbf{E}(\mathbf{r},\omega) \ , \tag{2.12}$$

$$\mathbf{J}(\mathbf{r},\omega) = \sigma(\mathbf{r},\omega)\mathbf{E}(\mathbf{r},\omega) \ , \tag{2.13}$$

in the long-wavelength limit ($q \to 0$), i.e. local response. Also, the Fourier transform

$$\mathbf{E}(\mathbf{r},\omega) = \int \mathbf{E}(\mathbf{r},t)e^{-i\omega t}dt \ , \tag{2.14}$$

is implicit, and similar relations apply for the remaining fields.

Furthermore, notice that in the absence of free charges and currents (as in free space or dielectric media), Maxwell's equations reduce to

$$\nabla \cdot \mathbf{E} = 0 \ , \tag{2.15}$$

$$\nabla \times \mathbf{B} = \frac{\epsilon}{c^2}\frac{\partial \mathbf{E}}{\partial t} \ , \tag{2.16}$$

$$\nabla \times \mathbf{E} = -\frac{\partial \mathbf{B}}{\partial t} \ , \tag{2.17}$$

$$\nabla \cdot \mathbf{B} = 0 \ . \tag{2.18}$$

In addition, expressions (2.16) and (2.17) can be written as

$$\nabla \times \mathbf{B} = -i\frac{\epsilon\omega}{c^2}\mathbf{E} \ , \tag{2.19}$$

$$\nabla \times \mathbf{E} = i\omega\mathbf{B} \ , \tag{2.20}$$

$$\tag{2.21}$$

where a harmonic time dependence in the form of $e^{-i\omega t}$ is assumed [or, equivalently, allowing a decomposition of the fields in terms of a plane-wave expansion – cf. equation (2.14)].

To conclude, let us just mention that by combining the curl equations (2.16) and (2.17), one arrives at the following Helmholtz equations for the electric and magnetic fields,

$$\left(\nabla^2 - \frac{1}{v^2}\frac{\partial^2}{\partial t^2}\right)\left\{ \begin{array}{c} \mathbf{E}(\mathbf{r},t) \\ \mathbf{B}(\mathbf{r},t) \end{array} \right\} = 0 \ , \tag{2.22}$$

which is a wave equation describing an electromagnetic wave travelling at $v = c/\sqrt{\epsilon}$.

2.1.2 Boundary conditions

Up to now we have considered electromagnetic fields in homogeneous media. Whenever the physical system under consideration involves more than one material, we must introduce the appropriate boundary conditions at each interface. These are obtained by applying the divergence theorem and Stoke's theorem to Maxwell's equations, yielding [62]

$$\mathbf{n} \cdot (\mathbf{D}_1 - \mathbf{D}_2) = \rho_s \ , \tag{2.23}$$

$$\mathbf{n} \cdot (\mathbf{B}_1 - \mathbf{B}_2) = 0 \ , \tag{2.24}$$

$$\mathbf{n} \times (\mathbf{B}_1 - \mathbf{B}_2) = \mu_0 \mathbf{J}_s \ , \tag{2.25}$$

$$\mathbf{n} \times (\mathbf{E}_1 - \mathbf{E}_2) = 0 \ , \tag{2.26}$$

where $\mathbf{n}$ is a unit vector normal to the interface (pointing from medium 2 to medium 1), whereas ρ_s and $\mathbf{J}_s$ are the (idealized) surface charge and surface current densities on the boundary, respectively.

2.2 Drude Model

Shortly after J. J. Thomson's discovery of the electron, Paul Drude came up with a model for the description of the electrical and thermal conduction in metals, borrowing the basic ideas of the successful kinetic theory of gases [63]. The Drude model attempts to explain the elementary properties of metals by regarding a metal as being essentially a *free electron gas*. Within this description, the loosely bound conduction electrons form an electron gas moving against a lattice of widely spaced, small ionic cores (encompassing both the nucleus and the tightly bound core electrons) in response to an applied electromagnetic field. The only interaction is via (instantaneous) collisions of electrons with the fixed ions, which occur with probability per unit time τ^{-1}, where τ is a phenomenological parameter known as the relaxation time. Therefore, the equation of motion for an electron of the metal subjected to

an external electric field $\mathbf{E}(t) = \mathbf{E}_0 e^{-i\omega t}$, becomes [64]

$$\frac{d\mathbf{p}(t)}{dt} = -\frac{\mathbf{p}(t)}{\tau} - e\mathbf{E}(t) \ , \tag{2.27}$$

where e is the elementary charge. We are now looking for a steady-state solution exhibiting the same harmonic time dependence of the driving field, so that the Fourier transform of equation (2.27) yields

$$-i\omega\mathbf{p}(\omega) = -\frac{\mathbf{p}(\omega)}{\tau} - e\mathbf{E}(\omega) \ , \tag{2.28}$$

whose solution is

$$\mathbf{p}(\omega) = \frac{e\mathbf{E}(\omega)}{i\omega - \tau^{-1}} \ . \tag{2.29}$$

Moreover, notice that the current density due to n_e electrons per unit volume, travelling with net velocity $\mathbf{v}$, is $\mathbf{J} = -en_e\mathbf{v}$. Hence, one can write

$$\mathbf{J}(\omega) = -\frac{en_e\mathbf{p}(\omega)}{m_e} = \frac{e^2 n_e}{m_e}\frac{1}{\gamma - i\omega}\mathbf{E}(\omega) \ , \tag{2.30}$$

where m_e is the mass of the electron and we have introduced the scattering rate, defined as $\gamma = \tau^{-1}$. By comparing the result (2.30) with the relation (2.9), the expression for the optical conductivity can be determined

$$\sigma(\omega) = \frac{e^2 n_e/m_e}{\gamma - i\omega} \ . \tag{2.31}$$

It will be useful for what follows to note that the conductivity and the dielectric function are linked through the following relationship[2]

$$\epsilon(\omega) = 1 + i\frac{\sigma(\omega)}{\epsilon_0\omega} \ , \tag{2.32}$$

allowing us to write

$$\epsilon(\omega) = 1 - \frac{\omega_p^2}{\omega^2 + i\gamma\omega} \ , \tag{2.33}$$

[2]This can be readily shown by working through Maxwell's equation using the constitutive relation (2.30) [64].

where $\omega_p^2 = \frac{e^2 n_e}{m_e \epsilon_0}$ denotes the *plasma frequency* of the free electron gas.

Despite its simplicity, the Drude model provides fairly good results for many metals (specially alkali metals) in the red and infrared region, where their optical properties are frequently dominated by the role of conduction electrons – intraband transitions. For noble metals, it fails to a great extent due to the onset of interband transitions in the visible and ultraviolet regions, and to other details of the bandstructure. These interband transitions can be accounted, while maintaining the classical picture, by adding a resonant contribution (whose resonant frequency corresponds to the transition energy) to the equation of motion, leading to a dielectric function containing a Lorentz-oscillator term.

Nevertheless, a fully and accurate description of the physics governing the optical response of metals requires a quantum mechanical formulation. Still, this is often circumvented by employing clever effective/phenomenological parameters and/or extra terms "by hand".

2.3 Graphene for Plasmonics

Graphene is a two-dimensional allotrope of carbon, where the carbon atoms are arranged in a honeycomb lattice. Being one-atom-thick, it can be regarded as a truly 2D material. Since its discovery in 2004 [46], graphene has been capitalizing a lot of the scientific community's atention due to its remarkable properties: it is stronger than steel and harder than diamond, but also flexible [65]; it exhibits an extremely large thermal conductivity [66] and sustains high current densities; its charge carriers are massless Dirac fermions obeying a Dirac-like relativistic equation, showing ballistic transport with huge electronic mobilities [67] even at room temperature; and the list goes on [47]. Owing to these unique properties, graphene has been dubbed a "*wonder material*".

Graphene's structural integrity is a direct consequence of the σ-bonds between its carbon atoms. Three out of its four valence electrons (belonging to $2s$, $2p_x$ and $2p_y$ orbitals) form hybridized sp^2 orbitals that make up the

σ-bonds, resulting in a trigonal planar structure where each carbon atom is covalently bonded to three neighbouring atoms via 1.42 Å long σ-bonds. The remaining electron contributes to the $2p_z$ orbital, which is perpendicular to the sp^2 orbitals' plane. The former can further bind with another $2p_z$ orbital from a neighbour carbon atom, leading to the formation of a π-bond. Since the unit cell contains two atoms, each contributing with one electron from the corresponding $2p_z$ orbital, graphene has a half-filled π band. Most of the electron dynamics and optical properties of graphene are determined by the nature of these π-bonds.

The low-energy physics of graphene takes place in the vicinity of the Dirac points (where the filled valence band touches the empty conduction band, for undoped, pristine graphene). Here, the spectrum of the Dirac fermions is linear, following $E(k) = \hbar v_F k$ with $v_F \approx \frac{c}{300} = 10^6$ m/s [48]. This makes graphene a suitable platform for relativistic tabletop experiments.

In this work, we shall focus on graphene as being a plasmonic material. As far as graphene plasmonics is concerned, all we need to describe its electromagnetic properties and light-matter interactions is encompassed within graphene's optical conductivity. Thus, further details on graphene will be overlooked. For a detailed treatment of graphene physics, please refer to [47, 48, 68].

2.3.1 Optical conductivity of graphene

Graphene's optical conductivity plays a key role in graphene optics and plasmonics. This important physical quantity can be split into two distinct contributions: one describing intraband transitions and another accounting for interband transitions, that is

$$\sigma_g(\omega) = \sigma_{\text{intra}}(\omega) + \sigma_{\text{inter}}(\omega) \ . \tag{2.34}$$

In writing the last expression it is implicit that we will ignore spatial dispersion (i.e. non-local effects) henceforth. An analytical expression for the dynamical conductivity of graphene can be obtained under the random phase

approximation (RPA) or via Kubo's formula [69, 70, 71, 72, 73], namely

$$\sigma_{\text{intra}}(\omega) = \frac{\sigma_0}{\pi}\frac{4}{\hbar\gamma - i\hbar\omega}\left[E_F + 2k_BT\ln\left(1+e^{-E_F/k_BT}\right)\right] , \tag{2.35}$$

characterizing intraband processes, where $\sigma_0 = e^2/(4\hbar)$, k_B is Boltzmann's constant and $E_F \approx |\mu|$, while for interband transitions we have

$$\sigma_{\text{inter}}(\omega) = \sigma_0\left[G(\hbar\omega/2) + i\frac{4\hbar\omega}{\pi}\int_0^\infty dE\frac{G(E)-G(\hbar\omega/2)}{(\hbar\omega)^2-4E^2}\right] , \tag{2.36}$$

with

$$G(x) = \frac{\sinh\left(\dfrac{x}{k_BT}\right)}{\cosh\left(\dfrac{E_F}{k_BT}\right)+\cosh\left(\dfrac{x}{k_BT}\right)} . \tag{2.37}$$

At zero temperature, or at least as long as the condition $E_F \gg k_BT$ is verified, the above equations reduce to

$$\sigma_{\text{intra}}(\omega) = \frac{\sigma_0}{\pi}\frac{4E_F}{\hbar\gamma - i\hbar\omega} , \tag{2.38}$$

$$\sigma_{\text{inter}}(\omega) = \sigma_0\left[\Theta(\hbar\omega - 2E_F) + \frac{i}{\pi}\ln\left|\frac{\hbar\omega-2E_F}{\hbar\omega+2E_F}\right|\right] , \tag{2.39}$$

where $\Theta(x)$ stands for the Heaviside step function. Notice that for $2E_F > \hbar\omega$ and $E_F \gg \hbar\omega$, the term describing interband transitions gives a negligible contribution – Pauli blocking. Therefore, we note that for frequencies in the terahertz (THz) and mid-IR spectral region – the regime that we are interested in this work –, at room temperature and under typical doping levels, graphene's optical conductivity is dominated by term describing intraband electronic processes, following the Drude-like expression

$$\sigma_g(\omega) \approx \frac{\sigma_0}{\pi}\frac{4E_F}{\hbar\gamma - i\hbar\omega} , \tag{2.40}$$

with good accuracy. The results for the conductivity of graphene are summarized in figure 2.1.

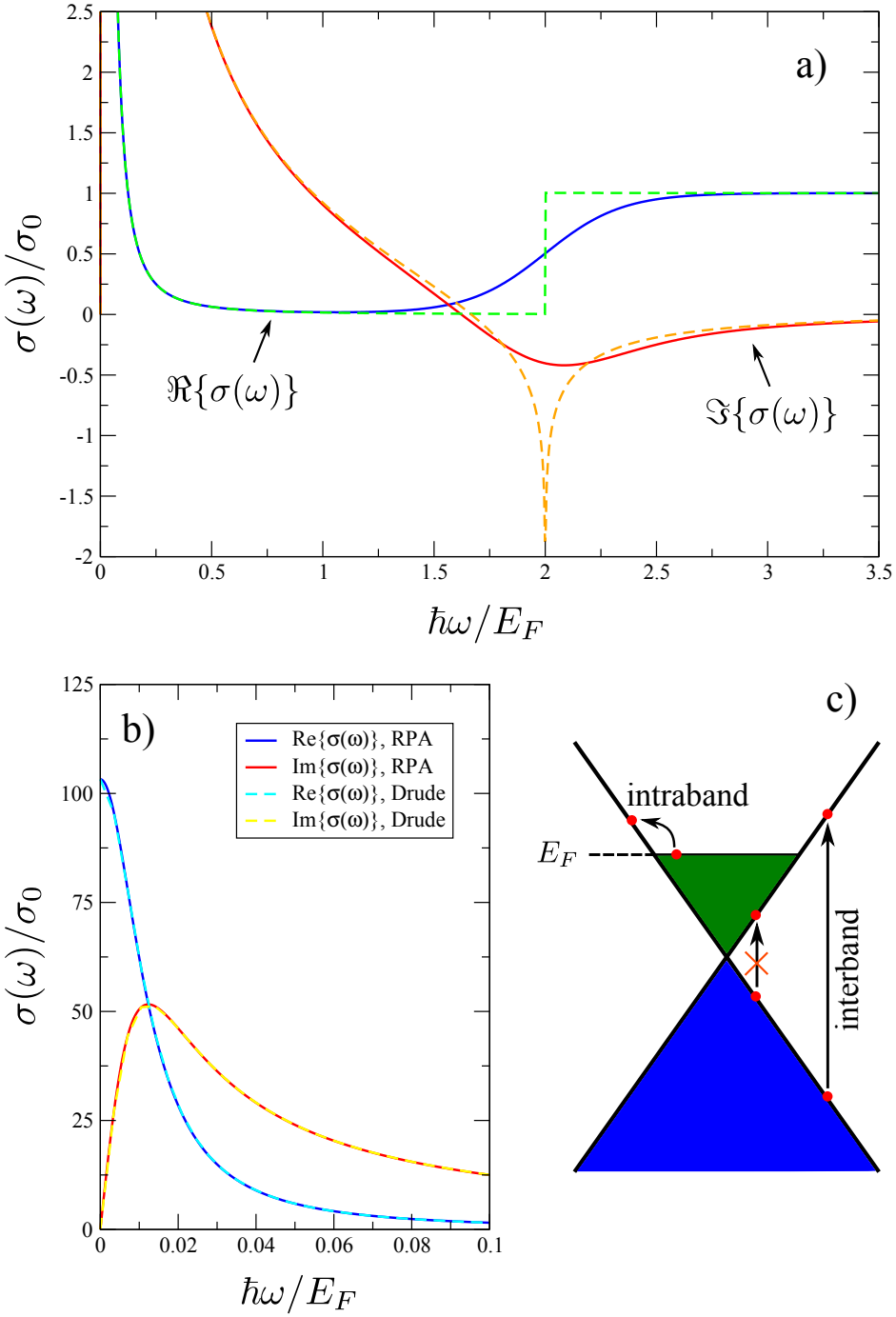


Figure 2.1: Optical conductivity of graphene: a) real and imaginary parts of the conductivity computed using the full local-RPA expression [equations (2.35) and (2.36)] at $T = 300$ K (continuous) and at $T = 0$ K (dashed); b) graphene's optical conductivity in the THz regime, obtained via RPA (continuous) and using Drude's expression (2.40) (dashed); c) schematic illustration of the transition processes in doped graphene. Parameters: $E_F = 0.3$ eV and $\hbar\gamma = 3.7$ meV.

Chapter 3

Surface Plasmon Polaritons at Dielectric-Metal Interfaces

Before jumping to graphene plasmonics, it is instructive to begin our study with the well known surface plasmon-polaritons (SPPs) at dielectric-metal interfaces. In this chapter, we will introduce the basic concepts in plasmonics and see how the main features of SPPs arise from the formalism of classical electrodynamics reviewed in the previous Chapter.

3.1 Single Dielectric-Metal Interface

In order to get acquainted with surface plasmon-polaritons, we begin our investigation by considering the simplest system capable of supporting SPPs. This corresponds to the case of a single (planar) interface between a dielectric and a metal. For our convenience, we shall assume that both media are semi-infinite, with the dielectric occupying the half-region defined by $z < 0$ and the metal occupying the half-region where $z > 0$, as depicted in figure 3.1. Additionally, the system is isotropic along the $\hat{\mathbf{y}}$ direction.

The dielectric medium is characterized by a real and positive dielectric constant, ϵ_1, whereas the electromagnetic properties of the metal will be taken into account by a complex, frequency-dependent dielectric function,

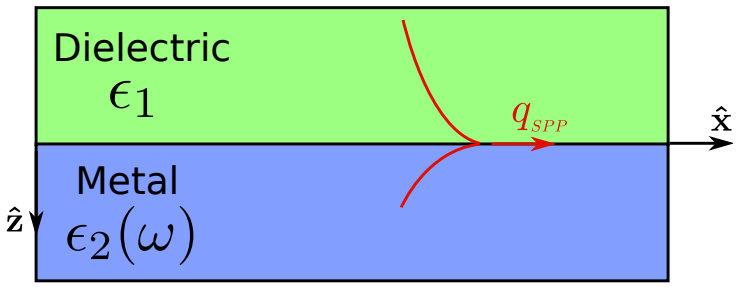


Figure 3.1: Schematic representation of a surface plasmon-polariton at an interface between a dielectric and a metal. The field profile is shown qualitatively for guidance.

$\epsilon_2(\omega)$, of the form

$$\epsilon_2(\omega) = 1 - \frac{\omega_p^2}{\omega^2 + i\omega\gamma} \ . \tag{3.1}$$

Recall that equation (3.1) is just the dielectric function of the metal within the free electron gas model [cf. equation (2.33)]. Furthermore, for the sake of simplicity, we assume that both ϵ_1 and $\epsilon_2(\omega)$ are isotropic – homogeneous and isotropic media.

The electromagnetic field due to a SPP can be obtained from the solution of Maxwell's equations, in each medium, in the form of a propagating surface electromagnetic wave which is confined to the whereabouts of the interface, and whose fields decay exponentially along the direction perpendicular to the interface (see, for instance, figure 3.1).

3.1.1 Dispersion relation

Let us first consider transverse magnetic (TM) solutions. These can be written as

$$\mathbf{E}_j(\mathbf{r},t) = (E_{j,x}\hat{\mathbf{x}} + E_{j,z}\hat{\mathbf{z}})\, e^{-\kappa_j|z|} e^{i(qx-\omega t)} \ , \tag{3.2}$$

$$\mathbf{B}_j(\mathbf{r},t) = B_{j,y}\hat{\mathbf{y}}\ e^{-\kappa_j|z|} e^{i(qx-\omega t)} \ , \tag{3.3}$$

where the index $j = 1, 2$ identifies the medium as in figure 3.1. Inserting equations (3.2) and (3.3) into Maxwell's equations (while assuming that the

materials are non-magnetic)

$$\nabla \times \mathbf{E}_j = -\frac{\partial \mathbf{B}_j}{\partial t} \ , \tag{3.4}$$

$$\nabla \times \mathbf{B}_j = \frac{\epsilon_j}{c^2}\frac{\partial \mathbf{E}_j}{\partial t} \ , \tag{3.5}$$

yields

$$B_{j,y} = \frac{\omega \epsilon_j}{c^2 q} E_{j,z} \ , \tag{3.6}$$

$$B_{j,y} = -i\,\mathrm{sgn}(z)\frac{\omega \epsilon_j}{c^2 \kappa_j} E_{j,x} \ , \tag{3.7}$$

$$E_{j,x} = -i\,\mathrm{sgn}(z)\frac{\kappa_j}{q} E_{j,z} \ , \tag{3.8}$$

$$\kappa_j = \sqrt{q^2 - \epsilon_j \omega^2/c^2}. \tag{3.9}$$

The boundary conditions of the problem require the continuity of the tangential components (relative to the interface) of the electric and magnetic fields across the interface (i.e. at $z = 0$),

$$E_{1,x} = E_{2,x} \ , \tag{3.10}$$

$$B_{1,y} = B_{2,y} \ , \tag{3.11}$$

(note that for non-magnetic media $H_{1,y} = H_{2,y} \Leftrightarrow B_{1,y} = B_{2,y}$). Writing the amplitudes of the magnetic field in terms of the corresponding electric field's amplitudes in the second boundary condition, using equation (3.7), we arrive at the following pair of equations:

$$E_{1,x} = E_{2,x} \ , \tag{3.12}$$

$$\frac{\epsilon_1}{\kappa_1} E_{1,x} = -\frac{\epsilon_2(\omega)}{\kappa_2} E_{2,x} \ . \tag{3.13}$$

The linear system composed by equations (3.12) and (3.13) has a non-trivial solution if

$$\boxed{\frac{\epsilon_1}{\kappa_1(q,\omega)} + \frac{\epsilon_2(\omega)}{\kappa_2(q,\omega)} = 0} \ , \tag{3.14}$$

from which we obtain the dispersion relation for TM surface plasmon-polaritons at a dielectric-metal interface. Note that in equation (3.14) we emphasized the fact that $\kappa_{1,2}$ depends on the frequency as well as on the wavevector in accordance to equation (3.9). Moreover, in order to have a confined electromagnetic surface wave, it follows from equation (3.14) that if $\epsilon_1 > 0$, then we must have $\Re\{\epsilon_2(\omega)\} < 0$ [since we need to meet the requirement that $\Re\{\kappa_{1,2}\} > 0$; see equations (3.2) and (3.3)]. This means that SPPs can only exist at interfaces between materials whose (real parts of the) dielectric permittivities have opposite signs, such as an interface between an insulator and a metal.

We can write a more explicit relation for the SPPs' wavevector, q_{SPP} , as a function of the frequency, by subtituting equation (3.9) into equation (3.14), obtaining

$$\boxed{q_{SPP} = \frac{\omega}{c}\sqrt{\frac{\epsilon_1\epsilon_2(\omega)}{\epsilon_1 + \epsilon_2(\omega)}}} \,. \tag{3.15}$$

We stress that equation (3.15) remains valid even for $\epsilon_2(\omega)$ with non-zero imaginary part, that is, for metals with damping. To better illustrate this result, we shall analyse separately the cases with and without attenuation.

Zero damping ($\gamma = 0$)

In the case of a lossless conductor, its corresponding Drude's dielectric function takes the simplified form

$$\epsilon_2(\omega) = 1 - \frac{\omega_p^2}{\omega^2} \,. \tag{3.16}$$

Figure 3.2 shows the dispersion relation obtained from inserting equation (3.16) into equation (3.15). The continuous curves represent the real part of the plasmon's wavevector and the dashed green curve its imaginary part. It is clear that whenever the value of q is a pure imaginary number, the existence of propagating modes is forbidden. In figure 3.2, this corresponds to the region between the two horizontal dashed-dotted lines. Outside this region, we can identify two kinds of fundamentally different plasmons: bulk plasmons (red

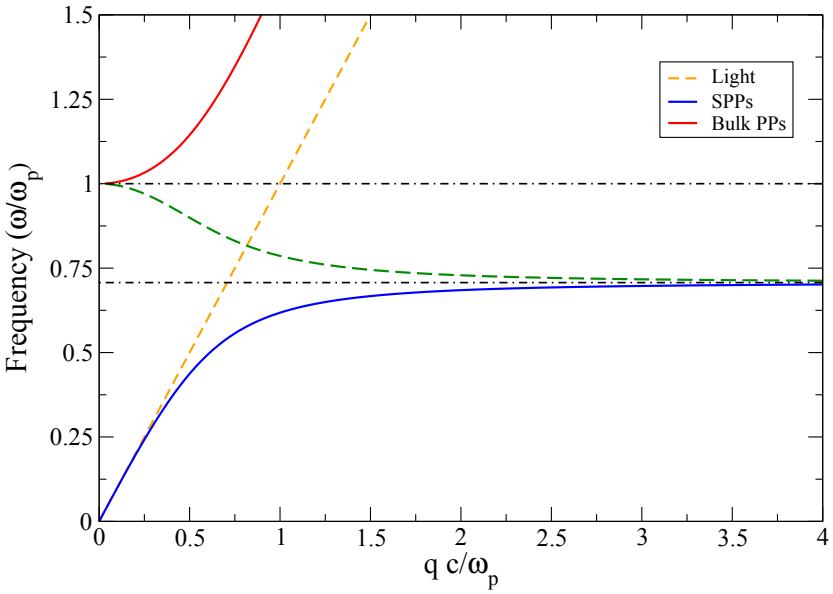


Figure 3.2: Dispersion relation of TM SPPs at an interface between air and a Drude metal without damping. We can identify essentially three different regions: an upper branch with radiative modes (red curve); a lower branch with bound SPPs modes (blue curve); and an intermediate region, with $\Re\{q\} = 0$, where propagation is forbidden (green dashed curve).

curve) and surface plasmon-polaritons (blue curve). The former consists in collective oscillations of the free electrons within the metal (also called volume plasmons), while the latter corresponds to bound excitations confined at the interface. In addition, in the upper branch of the dispersion relation relative to bulk plasmons, we have $\omega > \omega_p$, so that radiation propagates through metal - radiative modes - with q being real and $\kappa_j \rightarrow i\kappa_j$. On the other hand, since SPPs correspond to bound modes with both q and κ_j real, its dispersion curve must lie to the right of the light line in the dielectric (yellow line). Consequently, SPPs cannot be readily excited simply by impinging light onto the system, so that one has to come up with a mechanism capable of coupling light to surface plasmons. Examples of such techniques are prism and grating coupling, which will be described in more detail in Chapter 5.

Before moving on to the discussion of the case with a real (lossy) metal, let us take a closer look at the behaviour of SPPs in two limiting cases, those

of small and large wavevectors. In the regime of small wavevectors, the SPPs dispersion curve is close to the light line, and the SPP resembles an incident light wave tangent to the interface – Sommerfeld-Zenneck wave. Thus, $\kappa_1 \ll 1$ [cf. equation (3.9)] and the electromagnetic field is poorly confined, penetrating deep inside the dielectric. Conversely, for large wavevectors, it is apparent from figure 3.2 that the SPPs dispersion curve approaches a limiting frequency as $q \to \infty$. This frequency can be obtained from equation (3.15) by setting $\epsilon_1 + \epsilon_2(\omega) = 0$, yielding

$$\omega_{sp} = \frac{\omega_p}{\sqrt{1+\epsilon_1}} \ , \tag{3.17}$$

which is known as the *surface plasmon frequency* and corresponds to the lower horizontal line in figure 3.2. Note, however, that in this regime the group velocity $v_g = \frac{\partial \omega}{\partial q} \to 0$. Therefore this is a dispersionless mode with an electrostatic character, dubbed a *surface plasmon*.

Finite damping ($\gamma \neq 0$)

In real metals, there is often a miscellania of damping mechanisms which contribute to the attenuation of SPPs, ranging from electron-electron interactions to impurity and lattice scattering, just to mention a few. Within the framework of the Drude model, one attemps to account for all these phenomena by introducing a phenomenological parameter, γ, as in equation (3.1). Nevertheless, although the model captures fairly well the dominant features of noble metals at low frequencies, it fails (to a significant extent) with the onset of interband transitions at higher frequencies. In order to avoid further complications, we shall use the actual values of the dielectric function taken from experiments. In figures 3.3 and 3.4 is plotted the dispersion relation of SPPs using experimental data obtained from Ref. [74]. The most striking feature is that in this case there is a finite, maximum allowed wave vector for the SPPs, in contrast with the previous undamped case (compare, for instance, figures 3.2 and 3.3). This not only sets up a lower bound for the SPPs wavelength, given by $\lambda_{SPP} = 2\pi/\Re\{q\}$, but also limits the degree of

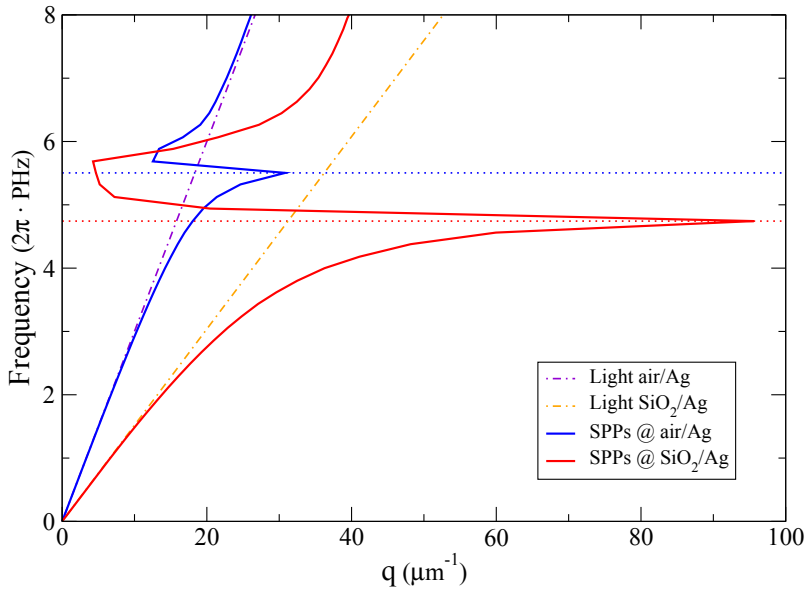


Figure 3.3: Dispersion relation of TM SPPs in air/Ag (blue) and SiO_2/Ag (red) interfaces, where we have used experimental data from Ref. [74] to account for silver's dielectric function. Owing to damping, the wavevector of the bounded SPPs modes is now limited to a maximum value at ω_{sp} (dotted lines).

confinement of the mode. Additionally, due to the non-vanishing γ, we now have the more general situation where the dielectric function of the conductor is a complex-valued function, and, therefore, so it is q, as illustrated in figure 3.4. Thus, the SPPs will be attenuated, losing energy as they travel along the system until they eventually fade away. Finally, note that unlike the case of a lossless metal - in which there was a gap, between ω_{sp} and ω_p, where the existence of modes was prohibited (i.e. with a purely imaginary propagation constant) - we now observe the emergence of *quasibound modes* in the aforementioned region.

Before moving on with our study of the basic features of SPPs, let us take a step back to analyse the case of a s-polarized, transverse electric (TE) surface electromagnetic wave. These modes have the electric field perpendicular to

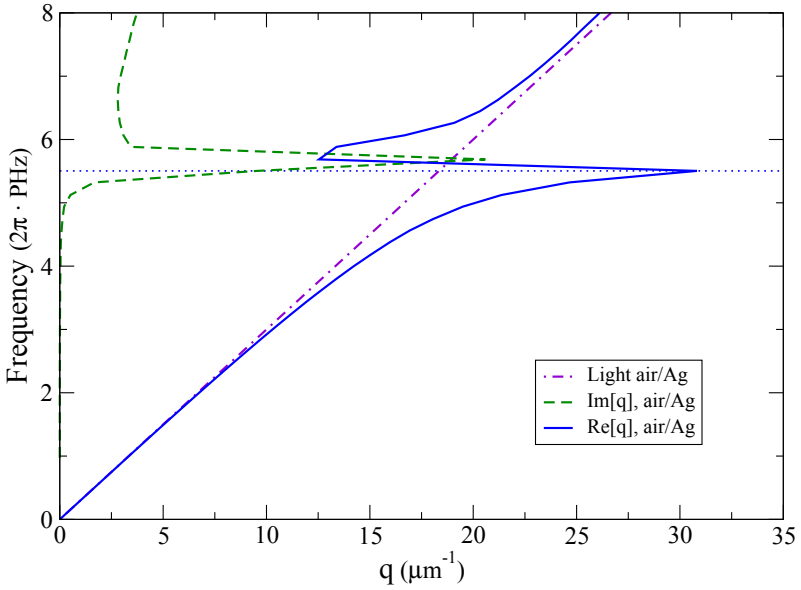


Figure 3.4: Dispersion relation with both real and imaginary parts of the propagation constant, q, of TM SPPs at an interface between air and silver, using experimental data from Ref. [74].

the plane of incidence, so that we will be seeking solutions of the type

$$\mathbf{E}_j(\mathbf{r},t) = E_{j,y}\hat{\mathbf{y}}\; e^{-\kappa_j|z|}e^{i(qx-\omega t)}\;, \tag{3.18}$$

$$\mathbf{B}_j(\mathbf{r},t) = (B_{j,x}\hat{\mathbf{x}} + B_{j,z}\hat{\mathbf{z}})\, e^{-\kappa_j|z|}e^{i(qx-\omega t)}\;. \tag{3.19}$$

As before, we substitute the fields (3.19) and (3.18) into Maxwell's equations (3.4) and (3.5), obtaining

$$B_{j,z} = \frac{q}{\omega}E_{j,y}\;, \tag{3.20}$$

$$B_{j,x} = -i\,\mathrm{sgn}(z)\frac{\kappa_j}{\omega}E_{j,y}\;, \tag{3.21}$$

$$B_{j,x} = -i\,\mathrm{sgn}(z)\frac{\kappa_j}{q}B_{j,z}\;, \tag{3.22}$$

$$\kappa_j = \sqrt{q^2 - \epsilon_j\omega^2/c^2}. \tag{3.23}$$

The boundary conditions at $z = 0$, read

$$E_{1,y} = E_{2,y} \ , \tag{3.24}$$

$$B_{1,x} = B_{2,x} \ . \tag{3.25}$$

Introducing equation (3.21) into the second boundary condition (3.25), and further combining equations (3.24) and (3.25), we arrive at the following condition:

$$(\kappa_1 + \kappa_2)E_{1,y} = 0 \ . \tag{3.26}$$

This condition may be satisfied if either $E_{1,y} = 0$ or $\kappa_1 + \kappa_2 = 0$. Note, however, that we must have $\Re\{\kappa_1\} > 0$ and $\Re\{\kappa_2\} > 0$ since we are looking for solutions confined to the dielectric-metal interface. Thus, the condition given by equation (3.26) can only be fulfilled if $E_{1,y} = E_{2,y} = 0$, that is, *TE surface plasmon-polaritons cannot exist* at interfaces between a dielectric and a conductor.

3.1.2 Propagation length and field confinement

In the above discussion of TM surface plasmon-polaritons, we claimed that the inherent Ohmic losses in metals render a complex-valued dielectric function. Thus, from equation (3.15) it can be seen that q will also be complex, $q = q' + iq''$, so that the attenuation of the SPPs solutions will be caracterized by an exponentially decaying term as $\exp(-q''x)$.

In particular, defining $\epsilon_2(\omega) = \epsilon_2' + i\epsilon_2''$ and inserting this into equation (3.15), we obtain

$$q = \frac{\omega}{c}\sqrt{\frac{\epsilon_1(\epsilon_2' + i\epsilon_2'')}{\epsilon_1 + \epsilon_2' + i\epsilon_2''}} \approx \frac{\omega}{c}\sqrt{\frac{\epsilon_1\epsilon_2'}{\epsilon_1 + \epsilon_2'}}\left[1 + i\frac{\epsilon_1\epsilon_2''/\epsilon_2'}{\epsilon_1 + \epsilon_2'}\right]^{1/2} \ , \tag{3.27}$$

where we have explicitly assumed that $|\epsilon_2'| > \epsilon_2''$ (condition satisfied from frequencies up to about ω_{sp}, i.e. the SPPs region) and we have also ignored

the terms of order $\mathcal{O}\left([\epsilon_2'']^2\right)$. Expanding equation (3.27), yields

$$q \approx \frac{\omega}{c}\sqrt{\frac{\epsilon_1\epsilon_2'}{\epsilon_1+\epsilon_2'}}\left[1+\frac{i}{2}\frac{\epsilon_1\epsilon_2'}{\epsilon_1+\epsilon_2'}\frac{\epsilon_2''}{(\epsilon_2')^2}\right] , \tag{3.28}$$

from which we identify

$$q' = \frac{\omega}{c}\sqrt{\frac{\epsilon_1\epsilon_2'}{\epsilon_1+\epsilon_2'}} \qquad \text{and} \qquad q'' = \frac{1}{2}\frac{\omega}{c}\left(\frac{\epsilon_1\epsilon_2'}{\epsilon_1+\epsilon_2'}\right)^{3/2}\frac{\epsilon_2''}{(\epsilon_2')^2} . \tag{3.29}$$

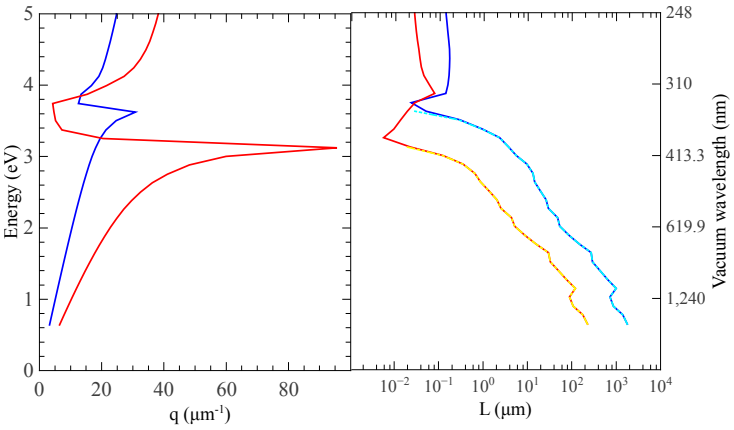
Since the electromagnetic field intensity of SPP decreases as $\exp(-2q''x)$, its characteristic propagation length is given by

$$\boxed{L_{SPP} = \frac{1}{2\Im\{q\}} \approx \frac{1}{2q''} = \frac{c}{\omega}\left(\frac{\epsilon_1+\epsilon_2'}{\epsilon_1\epsilon_2'}\right)^{3/2}\frac{(\epsilon_2')^2}{\epsilon_2''}} , \tag{3.30}$$

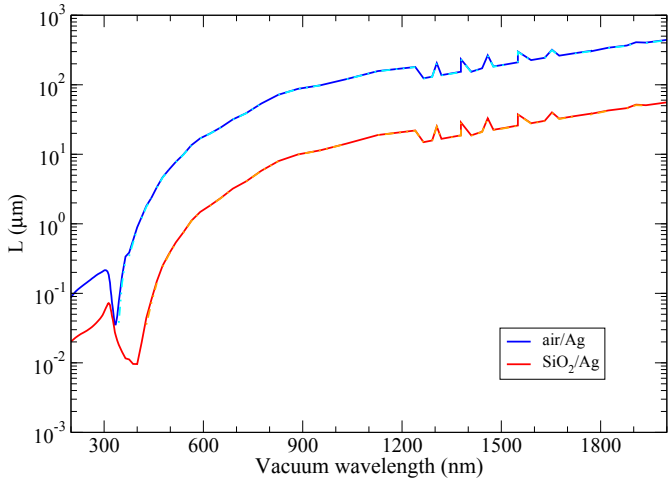
which defines the distance that the SPP travels until its intensity (along $\hat{\mathbf{x}}$) falls by $1/e$. Figure 3.5 shows the propagation lengths for surface plasmon-polaritons at air/silver and silica/silver interfaces (blue and red curves, respectively). Note that for wavelengths within the visible region, the propagation distances are of the order of a few micrometers up to 100 μm, whereas in the infrared they can reach values between 100 and 1000 μm. Naturally, these values depend upon the specific dielectric/metal involved[1]. Additionally, we find that the propagation length attains its minimum value as the frequency approaches ω_{sp}, as we had already anticipated in the previous subsection.

One of the most interesting properties of SPPs is their ability to confine the electromagnetic field, in the direction perpendicular to the interface, down to subwavelength scales beyond the diffraction limit. Since along this direction the fields fall off as $\exp(-\kappa_j|z|)$, we can quantify the "degree of field

[1] We further note that even for the very same metal we can come up with different results depending on the source of empirical data retrieved from the literature - e.g. compare figures 3.5a and 3.5b, obtained using data taken from Refs. [74] and [75], respectively. The reasons for the discrepancies observed among several experimental data available in the literature are still motif of debate and we shall not enter in such muddy waters.



(a) Left panel: dispersion relation of TM SPPs at air/Ag and SiO_2 interfaces (similar to figure 3.3). Right panel: corresponding propagation lengths. The full curves were obtained directly from $L = (2\Im\{q\})^{-1}$, while the dot-dashed curves were computed using the approximate expression presented in equation (3.30). The dielectric data was taken from Ref. [74].



(b) The same as in figure 3.5a (right panel) but now using the experimental data from Ref. [75].

Figure 3.5: Propagation lengths of SPPs at dielectric/metal interfaces.

confinement" by introducing the penetration depth, ζ, defined as

$$\zeta_j = \frac{1}{\Re\{\kappa_j\}} \ . \tag{3.31}$$

We can obtain an approximate expression for ζ in equation (3.31), by substituting equation (3.15) into equation (3.9), from which we arrive to

$$\zeta_{\text{diel.}} = \frac{c}{\omega}\sqrt{\frac{|\epsilon_2'| - \epsilon_1}{\epsilon_1^2}} \qquad \text{and} \qquad \zeta_{\text{metal}} = \frac{c}{\omega}\sqrt{\frac{|\epsilon_2'| - \epsilon_1}{(\epsilon_2')^2}} \tag{3.32}$$

for both the dielectric and the metal, as indicated by the subscripts in (3.32). In writing these expressions, we explicitly used the fact that ϵ_2' must be negative in order for SPPs to exist [recall our discussion after equation (3.14)], and we have neglected ϵ_2''. The behaviour of the penetration depths (also called attenuation length) of the electromagnetic field due to SPPs as a function of the corresponding vacuum wavelength is depicted in figure 3.6. In the metal,

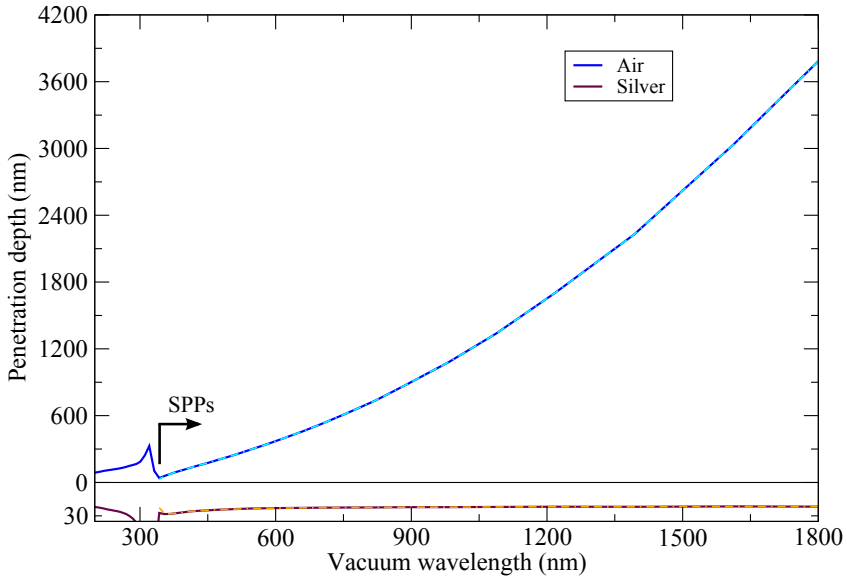


Figure 3.6: Penetration depths of the EM fields due to SPPs into air (blue curve) and silver (maroon curve), calculated using the optical constants from Ref. [74]. Note that we have plotted the penetration into the metal below the $\zeta = 0$ line, and notice the different scale in that region. The dot-dashed curves correspond to the approximate values obtained using expressions (3.32).

the penetration length is roughly constant for wavelengths below the surface plasmon frequency and it can be several orders of magnitude smaller than

in the dielectric. In contrast, the penetration depth of the electromagnetic field into the dielectric grows with increasing wavelength. This means that the ability of SPPs to confine the electromagnetic field deteriorates as the wavelength (frequency) increases (decreases).

We end our preliminary discussion of the basic properties of SPPs at single interfaces by noting that while the field confinement is weaker at lower frequencies (as we have just seen), the corresponding propagation length is larger (cf. figure 3.5). Thus, higher field localization comes hand in hand with larger losses. This trade-off between field confinement and propagation length is characteristic of plasmonics.

3.2 Multilayer Structures: Double Interface

Up to now, we have only treated the simplest case of a single flat dielectric-metal interface. Nevertheless, the landscape encompassing SPPs turns out to be much richer. The natural next step is to pursue our studies on SPPs in more complex (but still planar) geometries, such as systems containing several interfaces. From our previous endeavour, we expect that these multilayer structures have the capacity to sustain SPPs modes whenever there is an interface between a dielectric and a conductor. However, as we shall see ahead, SPPs in such heterostructures may exhibit interesting phenomena out of reach of ordinary SPPs at single interfaces. For the sake of clarity and pedagogy, as well as historical significance, here we will consider essentially two different systems: a thin metal film cladded between two semi-infinite dielectric media - dielectric/metal/dielectric (DMD) structure - and its "image", that being a dielectric layer sandwiched between two semi-infinite metallic layers - metal/dielectric/metal (MDM) structure. The common denominator is that both heterostructures can be regarded as three-layer systems with a double interface. In the case of a thin film, we already antecipated that bound SPPs solutions should exist at each of its interfaces. The novelty emerges when the thickness of the metallic film, d, becomes sufficiently small[2] to

[2]To be more quantitative, by sufficiently small we mean $\kappa_2 d \ll 1$.

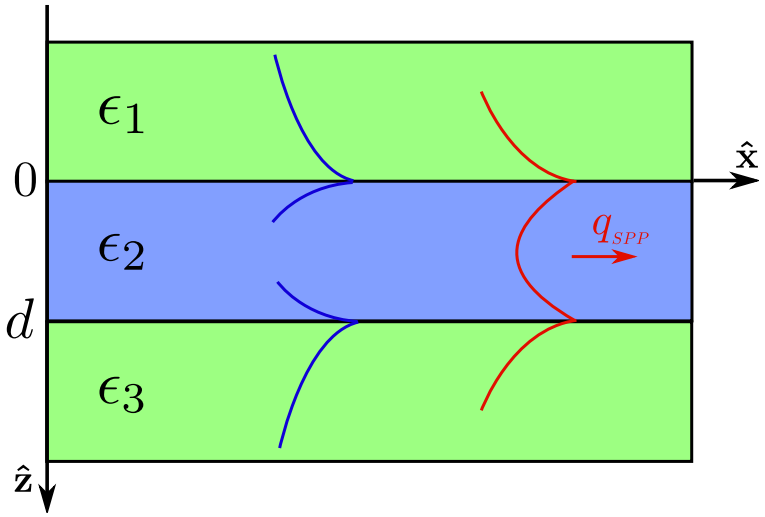


Figure 3.7: Schematic representation of a three-layer heterostructure - either DMD or MDM - capable of supporting surface plasmon-polaritons at each of its dielectric/metal interfaces. For metallic media it is implicit that its corresponding dielectric function is frequency-dependent, i.e. $\epsilon_m(\omega)$, where the subscript stands for "metal". The width of the core layer is caracterized by d, and the cladding media are assumed to be semi-infinite. In addition, the field of both two non-interacting surface plasmon-polaritons and a hybridized mode are qualitatively illustrated for eye guidance.

enable the communication between the electromagnetic fields of the SPPs modes at opposite interfaces. The result of this interaction will be the splitting of the *retarded* SPP condition, given by equation (3.15), into a set of two distinct new modes.

3.2.1 Dispersion relation

The procedure to derive the dispersion relation of surface plasmon-polaritons in a double interface will follow, in essence, the same steps as in subsection 3.1.1 for one dielectric-metal interface. The electromagnetic fields in the top and bottom media have the usual form of a TM surface wave

$$\mathbf{E}_j(\mathbf{r},t) = (E_{j,x}\hat{\mathbf{x}} + E_{j,z}\hat{\mathbf{z}})\, e^{-\kappa_j|z|} e^{i(qx-\omega t)} \ , \tag{3.33}$$

$$\mathbf{B}_j(\mathbf{r},t) = B_{j,y}\hat{\mathbf{y}}\ e^{-\kappa_j|z|} e^{i(qx-\omega t)} \ , \tag{3.34}$$

with

$$B_{j,y} = \frac{\omega\epsilon_j}{c^2 q} E_{j,z} \ , \tag{3.35}$$

$$B_{j,y} = -i\,\mathrm{sgn}(z)\frac{\omega\epsilon_j}{c^2\kappa_j} E_{j,x} \ , \tag{3.36}$$

$$E_{j,x} = -i\,\mathrm{sgn}(z)\frac{\kappa_j}{q} E_{j,z} \ , \tag{3.37}$$

$$\kappa_j = \sqrt{q^2 - \epsilon_j\omega^2/c^2}. \tag{3.38}$$

now for $j = 1, 3$ only [where $z < 0$ in region 1 and $z > d$ in region 3 [3] (see figure 3.7)]. The situation becomes different for medium $j = 2$ (where $0 < z < d$). Here, the fields can be described as a superposition of an exponentially growing wave with an exponentially decaying wave, of the form

$$\mathbf{E}_2(\mathbf{r},t) = \left\{ \left(E^{(+)}_{2,x}\hat{\mathbf{x}} + E^{(+)}_{2,z}\hat{\mathbf{z}}\right) e^{\kappa_2 z} \ + \ \left(E^{(-)}_{2,x}\hat{\mathbf{x}} + E^{(-)}_{2,z}\hat{\mathbf{z}}\right) e^{-\kappa_2 z} \right\} \ e^{i(qx-\omega t)} \ , \tag{3.39}$$

$$\mathbf{B}_2(\mathbf{r},t) = \left(B^{(+)}_{2,y} e^{\kappa_2 z} + B^{(-)}_{2,y} e^{-\kappa_2 z}\right)\hat{\mathbf{y}} \ e^{i(qx-\omega t)} \ , \tag{3.40}$$

satisfying the relations

$$B^{(+)}_{2,y} = -\frac{\omega\epsilon_2}{c^2 q} E^{(+)}_{2,z} \ , \tag{3.41}$$

$$B^{(+)}_{2,y} = i\frac{\omega\epsilon_2}{c^2\kappa_2} E^{(+)}_{2,x} \ , \tag{3.42}$$

$$B^{(-)}_{2,y} = -\frac{\omega\epsilon_2}{c^2 q} E^{(-)}_{2,z} \ , \tag{3.43}$$

$$B^{(-)}_{2,y} = -i\frac{\omega\epsilon_2}{c^2\kappa_2} E^{(-)}_{2,x} \ , \tag{3.44}$$

$$\kappa_2 = \sqrt{q^2 - \epsilon_2\omega^2/c^2} \ , \tag{3.45}$$

connecting the amplitudes of the magnetic field with the corresponding amplitudes of the electric field. Since now we have two interfaces, we will need

[3] Note that in the latter we could also have written the z-dependence of the fields in equations (3.33) and (3.34) as $e^{-\kappa_3(z-d)}$. As written in the text, the factor $e^{\kappa_3 d}$ is taken into account "inside" the amplitudes.

to employ two sets of boundary conditions, one at $z = 0$,

$$E_{1,x} = E_{2,x}^{(+)} + E_{2,x}^{(-)} \ , \tag{3.46}$$
$$B_{1,y} = B_{2,y}^{(+)} + B_{2,y}^{(-)} \ , \tag{3.47}$$

and the other at $z = d$,

$$E_{2,x}^{(+)} e^{\kappa_2 z} + E_{2,x}^{(-)} e^{-\kappa_2 z} = E_{3,x} e^{-\kappa_3 z} \ , \tag{3.48}$$
$$B_{2,y}^{(+)} e^{\kappa_2 z} + B_{2,y}^{(-)} e^{-\kappa_2 z} = B_{3,y} e^{-\kappa_3 z} \ . \tag{3.49}$$

Using expressions (3.35-3.38) and (3.41-3.45), one arrives at the following homogeneous linear system of equations

$$\begin{pmatrix} -1 & 1 & 1 & 0 \\ -\frac{\epsilon_1}{\kappa_1} & \frac{\epsilon_2}{\kappa_2} & -\frac{\epsilon_2}{\kappa_2} & 0 \\ 0 & e^{\kappa_2 d} & e^{-\kappa_2 d} & -e^{-\kappa_3 d} \\ 0 & \frac{\epsilon_2}{\kappa_2} e^{\kappa_2 d} & -\frac{\epsilon_2}{\kappa_2} e^{-\kappa_2 d} & \frac{\epsilon_3}{\kappa_3} e^{-\kappa_3 d} \end{pmatrix} \begin{pmatrix} E_{1,x} \\ E_{2,x}^{(+)} \\ E_{2,x}^{(-)} \\ E_{3,x} \end{pmatrix} = 0 \ . \tag{3.50}$$

The dispersion relation for transverse magnetic SPPs in a double interface is then obtained by solving the condition that the determinant of the matrix in (3.50) must be zero in order to exist a non-trivial solution, yielding

$$\boxed{\left(1 + \frac{\epsilon_2 \kappa_1}{\epsilon_1 \kappa_2}\right)\left(1 + \frac{\epsilon_2 \kappa_3}{\epsilon_3 \kappa_2}\right) = \left(1 - \frac{\epsilon_2 \kappa_1}{\epsilon_1 \kappa_2}\right)\left(1 - \frac{\epsilon_2 \kappa_3}{\epsilon_3 \kappa_2}\right) e^{-2\kappa_2 d}} \ . \tag{3.51}$$

This expression must be solved numerically, and it is implicit that $\kappa_j \equiv \kappa_j(q, \omega)$ and that $\epsilon_j \equiv \epsilon_j(\omega)$ for j referring to metallic media. Note that in the limit $d \to \infty$ (or $\kappa_2 d \gg 1$), corresponding to thick films in DMD heterostructures or to thick dielectric cores in MDM heterostructures, we get from equation (3.51) the conditions

$$\frac{\epsilon_1}{\epsilon_2} + \frac{\kappa_1}{\kappa_2} = 0 \qquad \text{and/or} \qquad \frac{\epsilon_3}{\epsilon_2} + \frac{\kappa_3}{\kappa_2} = 0 \ , \tag{3.52}$$

which are just the decoupled dispersion relations of the individual TM SPPs at each interface [cf. (3.14)].

It is interesting to consider the particular case of a symmetrical environment, in which the substrate and the superstrate are made of the same material, and thus $\epsilon_1 = \epsilon_3$ and $\kappa_1 = \kappa_3$. Under these circumstances, the dispersion relation (3.51) can be further simplified, and splits into two modes delivered by the following pair of equations:

$$\omega_+ : \quad \tanh(\kappa_2 d/2) = -\frac{\epsilon_2 \kappa_1}{\epsilon_1 \kappa_2} \ , \tag{3.53}$$

and

$$\omega_- : \quad \coth(\kappa_2 d/2) = -\frac{\epsilon_2 \kappa_1}{\epsilon_1 \kappa_2} \ , \tag{3.54}$$

corresponding to a high-frequency mode and a low-frequency mode, as indicated by the subscripts. In addition, it is also common to encounter these solutions in literature classified as an odd mode, where the tangential component of the electric field (E_x) is antisymmetric with respect to the plane $z = d/2$; and an even mode, in which the tangential component of the electric field is symmetric relative to the $z = d/2$ plane. Figure 3.8 shows the dispersion relation of non-radiative[4] SPPs in silver thin films (DMD heterostructures) free-standing in air, computed using equations (3.53) and (3.54) for several different widths. Silver's dielectric function, $\epsilon_2(\omega)$, is modeled as a free electron gas with negligible damping [see, for instance, equation (3.16)]. From figure 3.8 we see that in the case of the thickest film (orange dot-dashed line), its dispersion curve consists in two almost decoupled, degenerate modes (due to the symmetrical environment) and is indistinguishable to the one of a single air/Ag interface (black curve). However, as the film thickness is decreased, the evanescent tails of the SPPs in each interface overlap and hybridize, modifying the (independent) SPP dispersion. This interaction between the electromagnetic fields on different interfaces act as a perturbation which removes the degeneracy of the spectrum, splitting the original dispersion relation into two branches, ω_+ and ω_-, corresponding to modes in which the component of the electric field along the propagation direction is

[4]We mention that in this geometry the dispersion relation also returns solutions between ω_p and the curves plotted in figure 3.8 (not shown for clarity). These are highly damped, short-lived modes [76] (even when $\gamma \to 0$), so that we shall ignore them onwards.

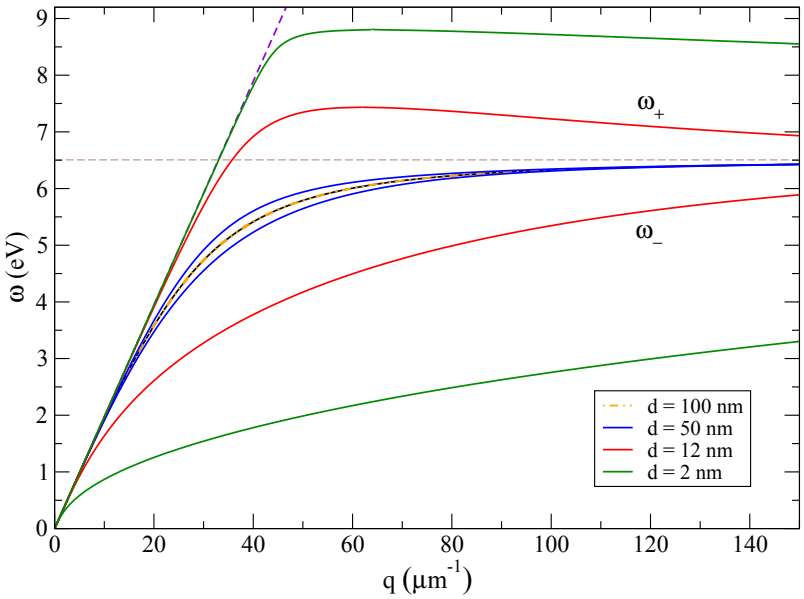


Figure 3.8: Dispersion relation of TM SPPs in a thin film, namely an air/silver/air multilayer structure, showing the hybridized, coupled modes for various mettalic layer thicknesses, d, indicated in the plot. The black curve represents the dispersion curve of SPPs in a single air/silver interface and the dashed violet line the dispersion of light in the dielectric. The broken horizontal line indicates the asymptotic surface plasmon frequency. Here, silver is assumed to be a lossless Drude metal with $\omega_p = 9.2$ eV.

an odd and an even function of $z - d/2$, respectively, as figure 3.9 illustrates. Furthermore, for sufficiently thin films, the antisymmetric solution exhibits an obvious maxima at frequencies above ω_{sp} in contrast both to the symmetric solution and to the single-boundary dispersion curve. Recall that for the latter, there is a gap between ω_{sp} and ω_p where propagation is not allowed (cf. figure 3.2). Additionally, note that the odd mode approaches the asymptotic surface plasmon frequency from above, with negative group velocity. On the other hand, the even mode has the ability to achieve large wavevectors at frequencies well below ω_{sp}, meaning that the corresponding SPP wavelengths will be extremely short.

The splitting of the SPPs dispersion curve due to the two coupled (bounded) modes in a thin oxydized aluminum film was experimentally demonstrated by

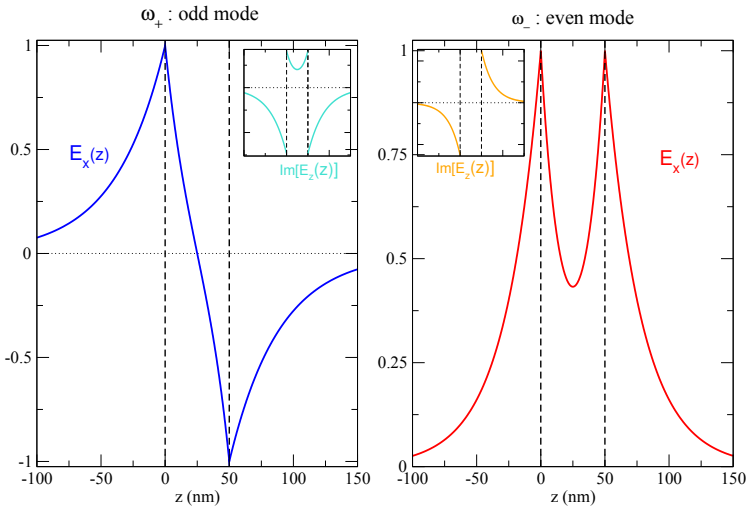


Figure 3.9: Profile of the tangential component of the electric field of SPPs in a double interface: air/silver/air. The insets also show $E_z(z)$ for completeness. Left: antisymmetric (odd) mode. Right: symmetric (even) mode. Parameters: $d = 50$ nm and $\omega = 5.5$ eV (yielding $q_{\text{odd}} = 38\ \mu\text{m}^{-1}$ and $q_{\text{even}} = 46\ \mu\text{m}^{-1}$).

Pettit *et al* [77] using electron-loss spectroscopy. Their results are shown in figure 3.10, where the typical dispersion of the hybridized ω_+ and ω_- modes can be clearly seen and follows closely the theoretical model.

So far for this geometry, we have limited our discussion to the ideal case of a lossless conductor. In general, as discussed earlier in the previous section, the metal's dielectric function will be described by a complex-valued function, which in turn can modify significantly the SPP dispersion relation.

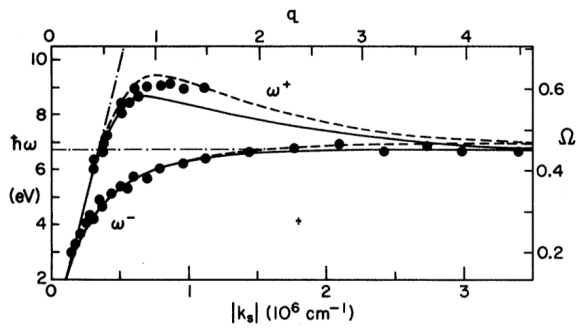


Figure 3.10: Experimental data of the SPPs dispersion in an oxydized 16 nm thin Al foil. The curves correspond to a theoretical fit of the two coupled modes for a 12 nm Al film sandwiched between two oxydized layers with a nominal thickness of 4 nm (continuous curve: α-Al_2O_3; dashed curve: amorphous aluminum). After Ref. [77].

Thus, and in parallel with what we have seen in the case of a single interface, we expect that q will approach a maximum value before folding back (eventually crossing the light line) to smaller wavevectors. An interesting feature of this type of three-layer system is that losses do not affect the two modes in the same way. For the odd mode, it can be shown that the imaginary part of the propagation constant decreases with decreasing film thickness. According to equation (3.30), this results in very long propagation distances and for that reason this mode was named *long-range surface plasmon-polariton* (LRSPP). In fact, multicentimeter propagation lengths were achieved experimentally, thus making it a good candidate for waveguiding applications. This behaviour can be understood by noting that the fraction of the field in the metal decreases with decreasing thickness, owing to the presence of a node in the longitudinal electric-field component at the film's midplane. The consequence of a smaller portion of the electric field inside the mettalic layer is a weaker interaction of the mode with the dissipative mechanisms of the film. Nevertheless, the reduction in attenuation comes along a concomitant decrease in field confinement, resembling a plane wave travelling in the homogeneous dielectric media in the limit of a very thin film [16, 76]. Conversely, the even mode is more and more attenuated as the film width is reduced (due to an increasingly higher fraction of the tangential electric-field component within the conductor), leading to short propagation distances – *short-range surface plasmon-polariton* (SRSPP). The dependence of both modes on the thickness of the core conductive layer is summarized in figure 3.11.

Throughout this Chapter we have briefly reviewed the fundamental concepts underlying the field of metal plasmonics. A lot more could have been told about this vast subject, like the discussion of the results for MDM heterostructures and also the case with $\epsilon_1 \neq \epsilon_3$, or even the blooming branch of metal-nanoparticles plasmonics. However, without these omissions this thesis would be otherwise too long and, perhaps more importantly, we remark that this is a work on graphene plasmonics. The first step towards that end shall be taken in the next Chapter.

An extensive description of plasmonics in metals and dielectrics can be

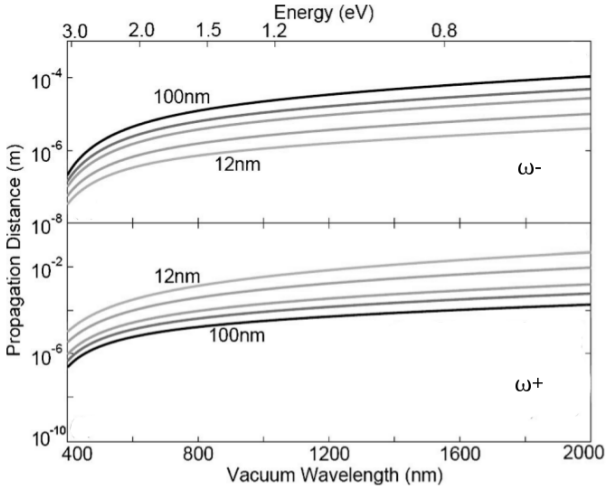


Figure 3.11: Propagation distance of even (top panel) and odd (bottom panel) SPPs modes in SiO_2/silver/SiO_2 for different thicknesses (d = 12, 20, 35, 50 and 100 nm), computed using optical constants retrieved from experiments. Adapted from Ref. [76].

found in Ref. [16].

Chapter 4

Graphene Surface Plasmons

In recent years we have been witnessing an impressive outburst in the field of plasmonics, with papers on the subject being published everyday at a great pace. On the other hand, graphene has been one of the most active topics in (but not limited to) the condensed matter physics community since its discovery in 2004, and ten years later our interest in the wonder material still thrives as it continues to present new challenges to us. The prediction of graphene surface plasmon-polaritons (GSPs) and its experimental observation led to the emergence of the field of graphene nanoplasmonics, which combines two of the most vibrant topics in physics today, and promises a huge impact in future technologies ranging from novel optoelectronic devices to applications in nanomedicine.

The main purpose of this chapter is to describe the physics governing surface plasmon-polaritons in simple graphene-based systems, before moving on to the treatment of more complex structures. In particular, we shall obtain the dispersion relation of GSPs in monolayer and double-layer graphene embedded in dielectric media, and investigate their properties, e.g. propagation length, field confinement, versatility, tunability, etc.

4.1 Monolayer Graphene

We begin our study of surface plasmon-polaritons in graphene by considering a system consisting in a single graphene sheet cladded between two semi-infinite dielectric media, characterized by the real dielectric constants ϵ_1 and ϵ_2, referring respectively to the top and bottom dielectrics, as depicted in figure 4.1.

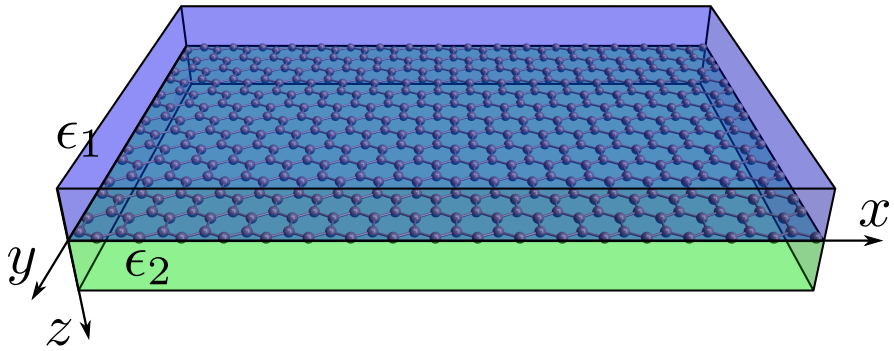


Figure 4.1: Illustration of a single graphene sheet sandwiched between two semi-infinite insulators with dielectric constants ϵ_1 and ϵ_2. Medium 1 occupies the $z < 0$ half-space and the $z > 0$ half-space is occupied by medium 2. The graphene sheet is located at the $z = 0$ plane.

4.1.1 Spectrum of TM GSPs

Let us assume a solution of Maxwell's equations, in the form of a p-polarized electromagnetic wave (TM wave). As in Chapter 3, we use the ansatz

$$\mathbf{E}_j = (E_{j,x}\hat{\mathbf{x}} + E_{j,z}\hat{\mathbf{z}})\, e^{iqx} e^{-\kappa_j |z|} \ , \tag{4.1}$$

$$\mathbf{B}_j = B_{j,y} e^{iqx} e^{-\kappa_j |z|} \hat{\mathbf{y}} \ , \tag{4.2}$$

where $j = 1, 2$ refers to the dielectric media with relative permittivities ϵ_1, ϵ_2. Equations (4.1) and (4.2) describe an electromagnetic surface wave which is confined to the neighbourhood of the graphene sheet and propagates along the $\hat{\mathbf{x}}$-direction. Due to the translational invariance of the system, the linear momentum along the propagation direction must be conserved, enabling us to write $q \equiv q_1 = q_2$. Moreover, we note that in writing these equations it

should be understood that they correspond to the spatial components of the fields. The time dependence, in what follows, is assumed to be of the typical harmonic form, i.e. $e^{-i\omega t}$.

Introducing equations (4.1) and (4.2) into Maxwell's equations for dielectric media

$$\nabla \times \mathbf{E}_j = -\frac{\partial \mathbf{B}_j}{\partial t} \ , \tag{4.3}$$

$$\nabla \times \mathbf{B}_j = \frac{\epsilon_j}{c^2}\frac{\partial \mathbf{E}_j}{\partial t} \ , \tag{4.4}$$

yields

$$-\operatorname{sgn}(z)\kappa_j E_{j,x} - iqE_{j,z} = i\omega B_{j,y} \ , \tag{4.5}$$

$$\operatorname{sgn}(z)\kappa_j B_{j,y} = -i\omega\epsilon_j/c^2 E_{j,x} \ , \tag{4.6}$$

$$iqB_{j,y} = -i\omega\epsilon_j/c^2 E_{j,z} \ , \tag{4.7}$$

which can be rewritten with respect to the magnetic field amplitudes, while also obtaining an expression for $\kappa_j(q,\omega)$

$$E_{j,x} = i\operatorname{sgn}(z)\frac{\kappa_j c^2}{\omega\epsilon_j}B_{j,y}, \tag{4.8}$$

$$E_{j,z} = -\frac{qc^2}{\omega\epsilon_j}B_{j,y}, \tag{4.9}$$

$$\kappa_j^2 = q^2 - \omega^2\epsilon_j/c^2 \ . \tag{4.10}$$

The boundary conditions linking the electromagnetic fields at $z = 0$ read[1]

$$E_{1,x}(x,z)|_{z=0} = E_{2,x}(x,z)|_{z=0} \ , \tag{4.11}$$

$$B_{1,y}(x,z)|_{z=0} - B_{2,y}(x,z)|_{z=0} = \mu_0 J_x(x,y) = \mu_0\sigma_{xx}E_{2,x}(x,z)|_{z=0} \ , \tag{4.12}$$

which assures the continuity of the tangential component of the electric field and the discontinuity of the tangential component of the magnetic field across the interface. Additionally, we further assume that graphene is a truly two-

[1]Within the linear response regime. This holds and gives accurate results is most situations.

dimensional material[2], whose entire electromagnetic properties are accounted in its frequency-dependent conductivity, $\sigma(\omega)$. Letting $\sigma(\omega) \equiv \sigma_{xx} = \sigma_{yy}$, meaning that graphene's conductivity is isotropic (which is true for unstrained graphene) and substituting the fields into the boundary conditions (4.11) and (4.12), we arrive to

$$\boxed{\frac{\epsilon_1}{\kappa_1(q,\omega)} + \frac{\epsilon_2}{\kappa_2(q,\omega)} + i\frac{\sigma(\omega)}{\omega\epsilon_0} = 0}\,, \tag{4.13}$$

which describes the dispersion relation, $\omega(q)$, of graphene TM surface plasmon-polaritons. Note that this is an implicit equation, in the sense that the conductivity depends on the frequency, and κ_j, given by equation (4.10), is a function of both momentum and frequency. Hence, despite the simple geometry of the system, the dispersion relation (4.13) does not have an analytical solution and must be solved by numerical means. In addition, it is clear that equation (4.13) only has real solutions when the imaginary part of the conductivity is positive and its real part vanishes. On the other hand, if the real part of the conductivity is non-zero, then, in general, the solutions will be complex. We shall discuss both cases separately in the next lines.

Recall that, in the spectral region in which we are interested in this work, that being in the terahertz to mid-IR regime, the conductivity of graphene is dominated by Drude's contribution

$$\sigma(\omega) = \sigma_0 \frac{4i}{\pi} \frac{E_F}{\hbar\omega + i\hbar\gamma}\,, \tag{4.14}$$

provided that $E_F \gg k_B T$ and $E_F \gg \hbar\omega$ (cf. section 2.3.1).

Figure 4.2 shows the spectrum of TM graphene surface plasmon-polaritons, obtained from the numerical solution of equation (4.13), where we have neglected absorption. Note that, once again, the dispersion curves lie to the right of the light lines in the dielectrics (due to the bound nature of SPPs). Thus, as we have seen in Chapter 3 when we studied SPPs in dielectric-metal interfaces, it is not possible to excite GSPs simply by directly shining electro-

[2]In this case, the (surface) current density is given by $\mathbf{J}(\mathbf{r}) = \mathbf{J}_s(x,y)\delta(z)$.

magnetic radiation on the structure. Moreover, in this case ($\gamma = 0$), for doped graphene, the conductivity is a purely imaginary function of the frequency, so that the wavevector, q, coming out of (4.13) is real. Conversely, in the

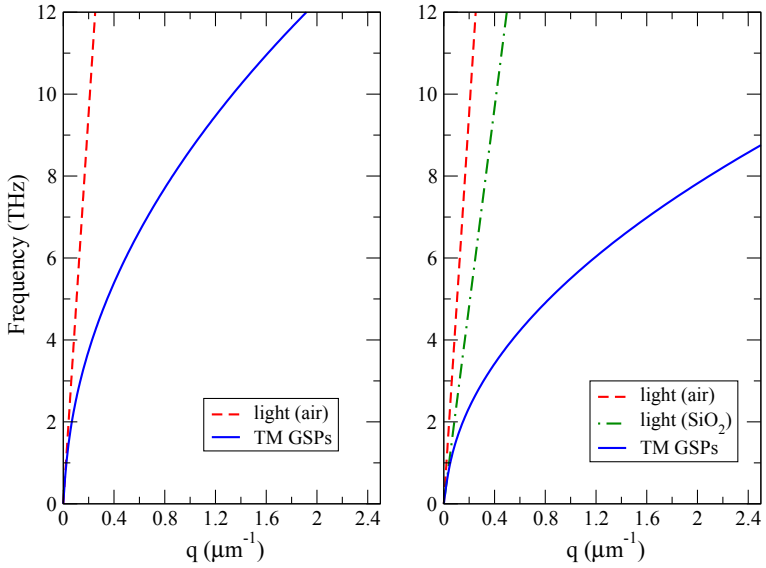


Figure 4.2: Dispersion relation of TM graphene surface plasmon-polaritons (GSPs) in a dielectric/graphene/dielectric heterostructure, as depicted in figure 4.1. Left: free-standing graphene in air; right: air/graphene/SiO_2. Here graphene's conductivity is assumed to be given by equation (4.14) without damping ($\gamma = 0$), so that the conductivity only has an imaginary part. We have used the following parameters: $E_F = 0.45$ eV, $\epsilon_{\text{air}} = 1$ and $\epsilon_{SiO_2} = 3.9$.

general (and more authentic) case where absorption is present, i.e. for finite γ, the dispersion relation yields a complex-valued wavevector, $q = q' + iq''$, whose imaginary part characterizes the attenuation of the SPP, as we shall see further ahead in the text. In figure 4.3 we present the dispersion curve of TM SPPs in graphene, retrieved from equation (4.13) using different values for the damping parameter entering in the conductivity (4.14). From the figure it is apparent that the GSP dispersion relation is shifted toward higher frequencies with respect to the dispersion curve with $\Gamma = \hbar\gamma = 0$, and that this effect is larger as Γ increases. The value $\Gamma = 3.7$ meV corresponds to a typical damping parameter obtained from transport measurements [78],

while $\Gamma = 20$ meV corresponds to a prohibitively high value for plasmonics. Nevertheless, taking absorption into account only changes the spectrum significantly in the region of low wavevectors, shown in the inset of figure 4.3. Looking at this figure at first glance, one might think that it should be possible to excite GSPs directly using three-dimensional EM beams, since the GSPs dispersion curves cross the light lines at some point. However, that is indeed not the case. Here, the usual reasoning fails because the region plotted

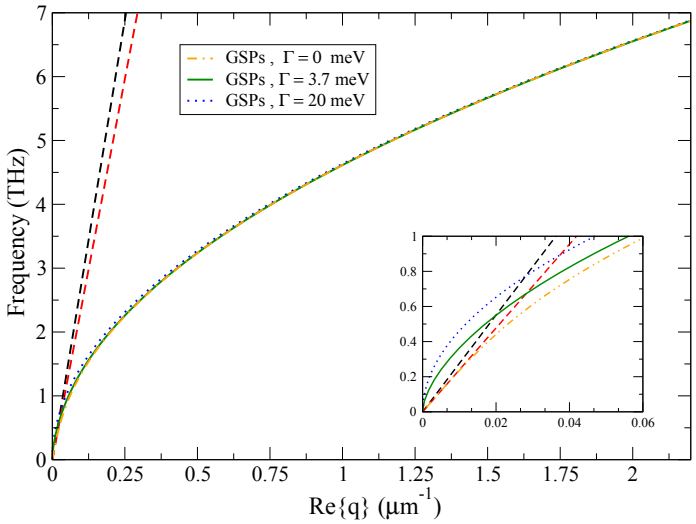


Figure 4.3: TM GSPs dispersion curves obtained from equation (4.13) using different values for the damping parameter, $\Gamma = \hbar\gamma$. For comparison, we have also included the dispersion relation with $\Gamma = 0$ (orange dot-dashed curve). The dashed lines represent the light dispersion in the cladding dielectrics. The inset shows a close-up of the low-q' region (the axis labels are the same as in the main figure). Parameters: $\epsilon_1 = 3$ (ion gel), $\epsilon_2 = 4$ (SiO_2) and $E_F = 0.45$ eV.

in the inset of figure 4.3 falls within the *overdamped* regime ($\omega_{SPP}/\gamma \lesssim 1$), in which GSPs (and SPPs in general) cannot be sustained[3]. We should stress that although the presence of a non-zero Γ does not significantly alter the aspect of the dispersion curve, it plays a leading role in the attenuation of SPPs, which increases with increasing Γ. Losses are often the main limiting factor in plasmonic-based systems, so that one usually wants a Γ value as

[3]In fact, for the exagerated $\Gamma = 20$ meV value, the overdamped regime extends beyond the inset of figure 4.3, up to most of the frequency range visible in the main figure.

small as possible.

Albeit by now we have essentially all we need in order to describe SPPs in single-layer graphene, in the end we still must rely on numerical means to solve equation (4.13). For pratical matters this does not constitute a problem *per se*, since any personal laptop will be able to compute the plasmonic spectrum with little effort. It is instructive, however, to analyse a couple of limits and simplifications where it is possible to obtain approximate expressions in closed-form. This will not only allow the reader to gain a deeper understanding of the theoretical framework, but also to build an intuition on the physics governing SPPs in graphene.

We start by assuming that the graphene sheet is embedded in a symmetrical dielectric environment ($\epsilon \equiv \epsilon_1 = \epsilon_2$), which is the degenerate case of the more general situation where the dielectric constants of each media are replaced by their average value, i.e. $\epsilon = (\epsilon_1 + \epsilon_2)/2$. In this limit, the dispersion relation (4.13) simplifies to

$$1 + i\frac{\sigma(\omega)}{2\omega\epsilon\epsilon_0}\sqrt{q^2 - \epsilon\omega^2/c^2} = 0 \ , \tag{4.15}$$

but still needs to be solved numerically. On the other hand, in the non-retarded regime where $q \gg \sqrt{\epsilon}\omega/c$, equation (4.15) reduces to

$$q \approx i\frac{2\omega\epsilon\epsilon_0}{\sigma(\omega)} \ . \tag{4.16}$$

Ignoring absorption, graphene's conductivity (4.14) becomes

$$\sigma(\omega) = 4i\alpha\epsilon_0 c\frac{E_F}{\hbar\omega} \ , \tag{4.17}$$

where $\alpha = \frac{e^2}{4\pi\epsilon_0\hbar c}$ is the fine-structure constant, and expression (4.16) transforms to

$$\hbar\omega_{GSP} \approx \sqrt{\frac{2\alpha}{\epsilon}E_F\hbar cq} \ , \tag{4.18}$$

with the typical $\omega_{GSP} \propto \sqrt{q}$ scaling. Furthermore, since for graphene we

have $E_F = v_F \hbar k_F$ with $k_F \propto n_e^{1/2}$, then the GSPs' frequency depends on the electronic density as

$$\omega_{GSP} \propto n_e^{1/4} \ . \tag{4.19}$$

While the plasmon dispersion $\omega_p \propto \sqrt{q}$ is inherent to all two-dimensional electronic systems [79], the behaviour portrayed in equation (4.19) is exclusive of graphene and has been confirmed by several experiments [52, 53].

We now take one step further in our analysis by including absorption. This is particularly important, since it will allow us to define the GSPs propagation length. Inserting Drude's full expression (4.14) for the conductivity into equation (4.15), we obtain

$$\kappa(q,\omega) = \frac{\epsilon\hbar}{2\alpha c}\frac{1}{E_F}\left(\omega^2 + i\gamma\omega\right) \ . \tag{4.20}$$

From equation (4.20), we can quantify the degree of confinement of the electromagnetic fields of GSPs in the dielectrics using the penetration depth, defined as

$$\zeta_{GSP} = \frac{1}{\Re\{\kappa\}} = \frac{2\alpha}{\epsilon}\hbar c\frac{E_F}{(\hbar\omega)^2} \ . \tag{4.21}$$

Note that for the same level of doping, the field confinement (penetration depth) is a monotonically increasing (decreasing) function of the frequency.

As we have mentioned before, for a non-zero damping parameter the dispersion relation returns a complex-valued wavevector, $q = q' + iq''$, which introduces the exponentially decaying term $\exp(-q''x)$ in the fields, and characterizes the attenuation of SPPs as they propagate along the graphene sheet. In the electrostatic limit ($\kappa \to q$), the dispersion relation (4.20) reduces to

$$q' + iq'' \approx \frac{\epsilon\hbar}{2\alpha c}\frac{1}{E_F}\left(\omega^2 + i\gamma\omega\right) \ , \tag{4.22}$$

(assuming $\gamma \ll \omega$) from which we retrieve

$$q' = \frac{\epsilon}{2\alpha\hbar c}\frac{(\hbar\omega)^2}{E_F} \ , \tag{4.23}$$

and

$$q'' = \frac{\epsilon\hbar}{2\alpha c}\frac{\gamma\omega}{E_F} \ . \tag{4.24}$$

Thus, it follows from equation (4.24) that the propagation length of SPPs in single-layer graphene (defined as the distance covered by GSPs when its intensity falls by $1/e$) is given by

$$L_{GSP} = \frac{1}{2q''} = \frac{\alpha}{\epsilon}\frac{\hbar c}{\Gamma}\frac{E_F}{\hbar\omega} \ , \tag{4.25}$$

which decreases with increasing Γ as expected. Additionally, notice that expression (4.23) has the same functional form as equation (4.18). Using the former, one can relate the GSP wavelength $\lambda_{GSP} = 2\pi/\Re\{q\} \approx 2\pi/q'$ to its corresponding light wavelength in vacuum, λ_0, namely[4]

$$\frac{\lambda_{GSP}}{\lambda_0} = \frac{2\alpha}{\epsilon}\frac{E_F}{\hbar\omega} \ . \tag{4.26}$$

Let us now consider an example: taking $\omega/(2\pi) = 10$ THz, $E_F = 0.3$ eV and $\epsilon = 4$, we obtain $\lambda_{GSP}/\lambda_0 \approx 0.026$; that is, the plasmon-polariton wavelength is almost two orders of magnitude shorter than the incident light wavelength, which is a respectable amount of localization far beyond the diffraction limit. For frequencies around $\omega_F = E_F/\hbar$ (usually in the mid-IR under typical doping concentrations), the sub-wavelength confinement is even stronger, being of the order of $\alpha \approx 1/137 \approx 0.007$. This is often the maximum attainable confinement for such a dielectric/graphene/dielectric system since for frequencies $\omega > \omega_F$ GSPs become severely damped due to the onset of interband Landau damping [53].

The ability of GSPs to achieve such high levels of spatial confinement in the THz and mid-IR regime is specially relevant, since in this spectral range SPPs in noble metals have a light-like behaviour and poor confinement, with wavelengths close to $\lambda_0/\sqrt{\epsilon}$ (at those frequencies the SPPs dispersion curve is indistinguishable of the light line; cf. figure 3.3). Moreover, the concentration

[4]It is worth to point out that it is possible to correct equation (4.26) for the case with asymmetric dielectric environments ($\epsilon_1 \neq \epsilon_2$) upon the replacement $\epsilon \to (\epsilon_1 + \epsilon_2)/2$ (but still in the non-retarded regime!). The same holds for relations (4.16) and (4.22)-(4.25).

of charge carriers in graphene can be easily controlled by electrical or chemical doping, allowing the realization of GSPs with tunable properties. All of the above makes graphene an attractive material for THz plasmonics.

4.1.2 Field profile of GSPs in single-layer graphene

Having obtained the dispersion relation of p-polarized SPPs in single-layer graphene, we now want to know in more detail what is the behaviour of the electromagnetic fields owing to this type of surface waves. In what follows, we will show how one can work through the equations obtained in the last subsection in order to reconstruct the fields. This exercise will also help us to better visualize, in an explicit fashion, the electromagnetic fields of GSPs. For the sake of clarity, here we will only consider the electric field[5].

With that in mind, let us pick a *characteristic* frequency, say $\omega_c = 2\pi \times 1\text{THz}$; we can then find the corresponding momentum $\omega_c(q_c)$ by solving numerically the dispersion relation [see, for instance, equation (4.13)]. At this point, we only need to set up the expressions for amplitudes of the fields. Recall that, from equations (4.8) and (4.9), we have

$$E_{j,z} = i\,\mathrm{sgn}(z)\frac{q}{\kappa_j}E_{j,x}\ . \tag{4.27}$$

Note that we can compute the field amplitudes up to a proportionality constant, that is, we have the freedom to normalize the fields as we wish (at least from a theoretical point of view). Normalizing the amplitudes of the fields with respect to $E_{1,x}$, we obtain

$$E_{1,x} = 1\ , \tag{4.28}$$
$$E_{1,z} = -i\frac{q_c}{\kappa_1}\ , \tag{4.29}$$
$$E_{2,x} = 1\ , \tag{4.30}$$
$$E_{2,z} = i\frac{q_c}{\kappa_2}\ , \tag{4.31}$$

[5]The magnetic field can be obtained in a similar manner. Additionally, one may use the electric-field amplitudes to build the corresponding amplitudes of the magnetic field.

where $E_{1,x} = E_{2,x}$ follows from the first boundary condition (4.11). Once again, the dependence of $\kappa_{1,2}$ on the frequency (and wavevector) is implicit, i.e. $\kappa_{1,2} \equiv \kappa_{1,2}(q_c, \omega_c)$. Therefore, we now have everything we need to construct the electric field, namely a pair (q_c, ω_c) which satisfies the dispersion relation, the parameters $\kappa_{1,2}(q_c, \omega_c)$ and the electric-field amplitudes, given by equations (4.28)-(4.31). Plugging all these into

$$\mathbf{E}_{GSP}\left(\mathbf{r}\right) = E_x(x,z)\ \hat{\mathbf{x}} + E_z(x,z)\ \hat{\mathbf{z}}\ , \tag{4.32}$$

where

$$E_\nu(x,z) = \begin{cases} \Re\left\{E_{1,\nu} e^{iqx} e^{-\kappa_1 |z|}\right\}\ , & \text{for } z \leq 0 \\ \Re\left\{E_{2,\nu} e^{iqx} e^{-\kappa_2 |z|}\right\}\ , & \text{for } z > 0 \end{cases}\ , \tag{4.33}$$

with $\nu = x, z$ [cf. equation (4.1)], allows us to compute the electric vectorial field and its corresponding magnitude at any given point. The results are summarized in figure 4.4. In the top panel we show the (normalized) absolute value of the electric field in the xz-plane, with its respective field lines superimposed. On the other hand, in the central panel we have plotted $\mathrm{sgn}(z)E_z(x,z)$, which enables us to get a clearer picture of the coherent charge-density fluctuations, differentiating the locations with higher density of electrons (blue) and holes (red) [notice the direction of the field lines]. Finally, in the bottom panels we have density plots of the x- and z-components of the individual electric field.

Further, from figure 4.4 we can observe the surface-wave character of GSPs, since the magnitude of the field decays exponentially as we move away from the graphene plane (shown as a horizontal black line at $z = 0$ in the figure). Also apparent is the collective behaviour of these electronic density oscillations.

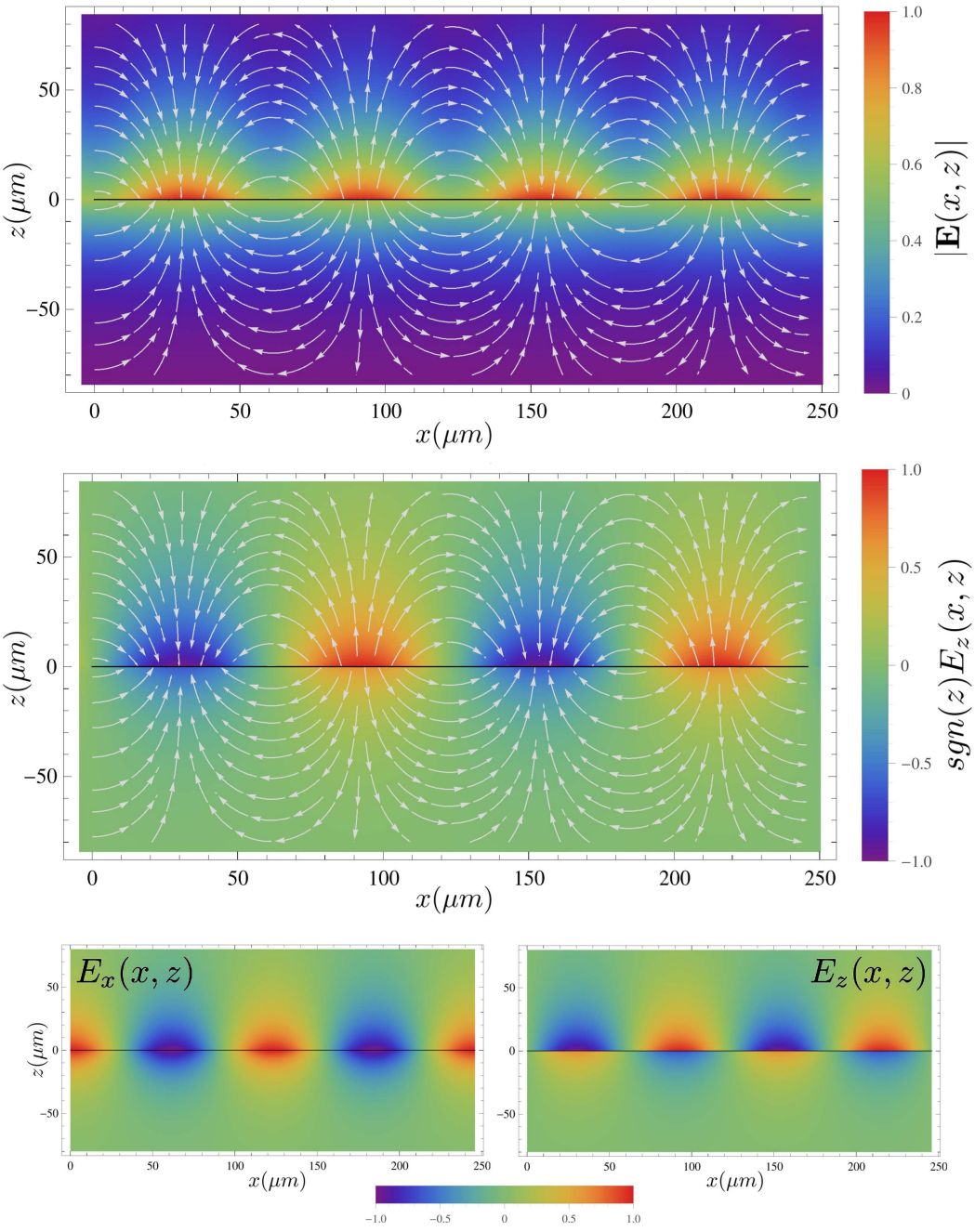


Figure 4.4: Graphical representations of the electric field (a.u.) of TM GSPs in an air/graphene/SiO_2 heterostructure, as depicted in figure 4.1 (note that here the plots are rotated with respect to figure 4.1). The graphene sheet is represented as a black horizontal line. We have used the following parameters: $\omega_c = 2\pi \times 1\text{THz}$, $q_c = 0.051\ \mu\text{m}$, $E_F = 0.45$ eV, $\gamma = 0$, $\epsilon_{\text{air}} = 1$ and $\epsilon_{SiO_2} = 3.9$.

4.1.3 A word on TE GSPs

Unlike common metals, graphene has the ability to support transverse electric (TE) surface plasmon-polariton modes [56]. In the following, we shall obtain the spectrum of TE GSPs and discuss the necessary conditions for their existence.

Here, we will be looking for solutions of Maxwell's equation of the type

$$\mathbf{E}_j(\mathbf{r},t) = E_{j,y}\hat{\mathbf{y}}\, e^{-\kappa_j|z|}e^{i(qx-\omega t)}\ , \tag{4.34}$$

$$\mathbf{B}_j(\mathbf{r},t) = (B_{j,x}\hat{\mathbf{x}} + B_{j,z}\hat{\mathbf{z}})\, e^{-\kappa_j|z|}e^{i(qx-\omega t)}\ . \tag{4.35}$$

where the relations between the fields' amplitudes are the same as in equations (3.20)-(3.22), and, as it is by now ordinary, $\kappa_j = \sqrt{q^2 - \epsilon_j\omega^2/c^2}$. In this case, the boundary conditions read

$$E_{1,y}(x,z)|_{z=0} = E_{2,y}(x,z)|_{z=0}\ , \tag{4.36}$$

$$B_{2,x}(x,z)|_{z=0} - B_{1,x}(x,z)|_{z=0} = \mu_0 J_y(x,y) = \mu_0\sigma_{yy}E_{2,y}(x,z)|_{z=0}\ , \tag{4.37}$$

which upon substituting the fields (4.34) and (4.35), satisfying the relations (3.20)-(3.22), yields the equation for the dispersion relation of TE SPPs in graphene,

$$\boxed{\kappa_1(q,\omega) + \kappa_2(q,\omega) = i\mu_0\omega\sigma(\omega)}\ , \tag{4.38}$$

where we have once again assumed that the local dynamic conductivity is isotropic. We note that equation (4.38) only has solutions if and only if the imaginary part of $\sigma(\omega)$ is negative. A non-zero real part of the conductivity introduces damping by making $\Im\{q\} \neq 0$. For conventional two-dimensional electron systems, e.g. in GaAs/AlGaAs quantum-well structures, the conductivity follows the Drude model, so that the imaginary part of the optical conductivity is always positive. Therefore, TE SPPs cannot be realized in 2DEGs. However, graphene's conductivity provides a much richer landscape: besides the Drude-like intraband contribution, there is another term accounting for interband electronic processes, which can be negative. Thus, whenever the net sum of both contributions yields $\Im\{\sigma\} < 0$, the excitation of TE GSPs

is possible – this occurs in the window of frequencies $1.667 < \hbar\omega/E_F < 2$, where interband transitions prevail [56, 80, 81].

We further note that the spectrum given by (4.38) needs to be computed analytically; notwithstanding, since the term on the right-hand side is small – being proportional to α – the TE GSPs dispersion does not depart much from the light line, i.e. $\hbar\omega \lesssim \hbar cq/\sqrt{\epsilon}$, which translates in poor confinement. This last feature makes them less interesting than TM modes, and thus we will consider only TM modes hereafter.

4.2 Double-Layer Graphene

In the last section we investigated the main features of SPPs in a single (continuous) graphene sheet. We have shown that GSPs frequencies typically lie between the THz and the mid-IR regions of the electromagnetic spectrum. In this section we will proceed with our studies of SPPs in graphene, taking one step further on the complexity ladder by considering a system with two graphene layers. This double-layer graphene structure consists in two graphene sheets, separated by a dielectric medium with relative permittivity ϵ_2 and thickness d, enclosed by two semi-infinite top and bottom dielectrics as illustrated in figure 4.5. Note that this is somewhat similar to the case of a dielectric/metal/dielectric heterostructure, in the sense that the system has two interfaces, each capable of sustaining SPPs on their own. Thus, based on what we have seen in section 3.2, we may already antecipate that when the graphene layers are sufficiently close to one another, the two individual GSPs will interact leading to the emergence of a pair of hybridized GSPs modes. Nonetheless, as in the present case the conductor is (doped) graphene, the corresponding plasmon-polaritons will inherit the remarkable plasmonic properties of graphene that we have outlined in the previous section.

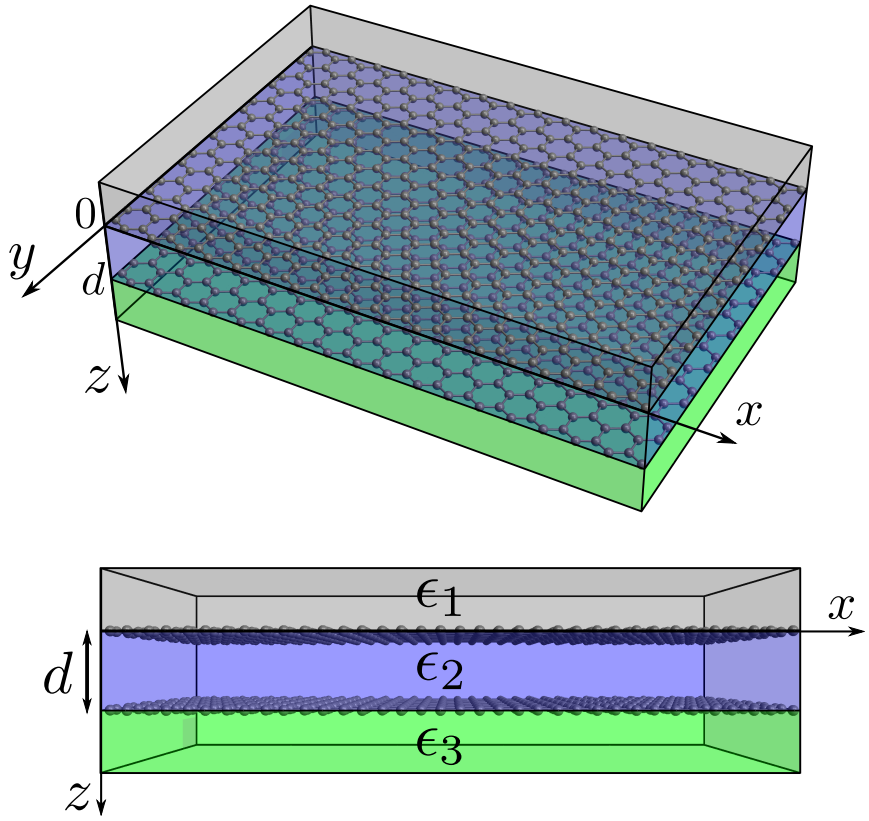


Figure 4.5: Double-layer graphene structure. The graphene sheets (placed at the planes defined by $z = 0$ and $z = d$) are separated by a dielectric slab of thickness d and relative permittivity ϵ_2. Medium 1 occupies the $z < 0$ half-space and the $z > d$ half-space is occupied by the dielectric medium 3.

4.2.1 Dispersion relation

With the purpose of computing the spectrum of GSPs in double-layer graphene, we assume solutions of Maxwell's equations in the (by now customary) form of,

$$\mathbf{E}_j(\mathbf{r}, t) = (E_{j,x}\hat{\mathbf{x}} + E_{j,z}\hat{\mathbf{z}})\, e^{-\kappa_j |z|} e^{i(qx-\omega t)} \,, \tag{4.39}$$

$$\mathbf{B}_j(\mathbf{r}, t) = B_{j,y}\hat{\mathbf{y}}\; e^{-\kappa_j |z|} e^{i(qx-\omega t)} \,, \tag{4.40}$$

for $j = 1$ ($z < 0$) and $j = 3$ ($z > d$) alone. Here we shall limit ourselves to the study of transverse magnetic modes (i.e. whose electric field lies in a plane perpendicular to the interfaces/graphene sheets). For the core dielectric

medium $0 < z < d$, we do not need to meet the requirement of vanishing fields at $z \to \pm\infty$, so that, in general, these can be written as a linear combination of exponentially growing "(+)" and exponentially decaying "(−)" electromagnetic waves, that is

$$\mathbf{E}_2(\mathbf{r},t) = \left\{ \left(E_{2,x}^{(+)}\hat{\mathbf{x}} + E_{2,z}^{(+)}\hat{\mathbf{z}}\right) e^{\kappa_2 z} \; + \; \left(E_{2,x}^{(-)}\hat{\mathbf{x}} + E_{2,z}^{(-)}\hat{\mathbf{z}}\right) e^{-\kappa_2 z} \right\} \; e^{i(qx-\omega t)} \; , \tag{4.41}$$

$$\mathbf{B}_2(\mathbf{r},t) = \left(B_{2,y}^{(+)} e^{\kappa_2 z} + B_{2,y}^{(-)} e^{-\kappa_2 z}\right) \hat{\mathbf{y}} \; e^{i(qx-\omega t)} \; . \tag{4.42}$$

The relations between the amplitudes of the magnetic field with respect to their corresponding electric-field amplitudes, are given by expressions (3.35) and (3.36) for $j = 1, 3$, and equations (3.41)-(3.44) for $j = 2$. Additionally, we have $\kappa_j = \sqrt{q^2 - \epsilon_j \omega^2/c^2}$ as before.

Assuming the same doping concentration in both graphene layers, the boundary conditions at $z = 0$ and $z = d$ read

$$E_{1,x} = E_{2,x}^{(+)} + E_{2,x}^{(-)} \; , \tag{4.43}$$

$$B_{1,y} = B_{2,y}^{(+)} + B_{2,y}^{(-)} + \mu_0 \sigma(\omega) E_{1,x} \; , \tag{4.44}$$

and

$$E_{2,x}^{(+)} e^{\kappa_2 z} + E_{2,x}^{(-)} e^{-\kappa_2 z} = E_{3,x} e^{-\kappa_3 z} \; , \tag{4.45}$$

$$B_{2,y}^{(+)} e^{\kappa_2 z} + B_{2,y}^{(-)} e^{-\kappa_2 z} - B_{3,y} e^{-\kappa_3 z} = \mu_0 \sigma(\omega) E_{3,x} e^{-\kappa_3 z} \; , \tag{4.46}$$

respectively. Equations (4.43)-(4.46) form a linear system, which may be casted in matrix form as

$$\begin{pmatrix} -1 & 1 & 1 & 0 \\ \frac{\epsilon_1}{\kappa_1} + i\frac{\sigma}{\omega\epsilon_0} & -\frac{\epsilon_2}{\kappa_2} & \frac{\epsilon_2}{\kappa_2} & 0 \\ 0 & e^{\kappa_2 d} & e^{-\kappa_2 d} & -e^{-\kappa_3 d} \\ 0 & \frac{\epsilon_2}{\kappa_2} e^{\kappa_2 d} & -\frac{\epsilon_2}{\kappa_2} e^{-\kappa_2 d} & \left(\frac{\epsilon_3}{\kappa_3} + i\frac{\sigma}{\omega\epsilon_0}\right) e^{-\kappa_3 d} \end{pmatrix} \begin{pmatrix} E_{1,x} \\ E_{2,x}^{(+)} \\ E_{2,x}^{(-)} \\ E_{3,x} \end{pmatrix} = 0 \; . \tag{4.47}$$

The dispersion relation of GSPs in a double-layer graphene structure can be obtained by solving $\det(\mathbf{M}) = 0$, where $\mathbf{M}$ is the matrix that appears in

equation (4.47). After some algebra, one arrives at

$$e^{\kappa_2 d}\left(\frac{\epsilon_3}{\kappa_3}+i\frac{\sigma}{\omega\epsilon_0}+\frac{\epsilon_2}{\kappa_2}\right)\left(\frac{\epsilon_1}{\kappa_1}+i\frac{\sigma}{\omega\epsilon_0}+\frac{\epsilon_2}{\kappa_2}\right)= e^{-\kappa_2 d}\left(\frac{\epsilon_3}{\kappa_3}+i\frac{\sigma}{\omega\epsilon_0}-\frac{\epsilon_2}{\kappa_2}\right)\left(\frac{\epsilon_1}{\kappa_1}+i\frac{\sigma}{\omega\epsilon_0}-\frac{\epsilon_2}{\kappa_2}\right) \ . \tag{4.48}$$

This is a transcendental equation, so that one needs to use numerical techniques in order to compute the dispersion relation. The plasmonic spectrum rendered by equation (4.48) is plotted in figure 4.6, and it clearly shows the two hybridized modes arising from the interaction among GSPs in opposite graphene sheets (provided that d is small enough to allow the "communication" between the evanescent tails of each individual GSP). This inter-layer Coulomb interaction splits the spectrum into two branches: one solution lying above the dispersion curve of SPPs in single-layer graphene, corresponding to the *optical mode*; and a lower frequency solution, corresponding to the *acoustic mode*. For the former, the electric-field component along the propagation direction, $E_x(z)$, is symmetric with respect to the $z = d/2$ plane (the charges in both layers oscillate in phase), while for the latter it is antisymmetric with respect to the same plane (the charge-density oscillations are in antiphase)[6]. Moreover, we note that the splitting of the spectrum is stronger for smaller values of d, as figure 4.6 illustrates.

As before, in the limit $\kappa_2 d \to \infty$, we recover the expressions for the dispersion relations corresponding to the individual, non-interacting GSPs in each graphene layer,

$$\left(\frac{\epsilon_3}{\kappa_3}+\frac{\epsilon_2}{\kappa_2}+i\frac{\sigma}{\omega\epsilon_0}\right)\left(\frac{\epsilon_1}{\kappa_1}+\frac{\epsilon_2}{\kappa_2}+i\frac{\sigma}{\omega\epsilon_0}\right)=0 \ , \tag{4.49}$$

which are equivalent to equation (4.13).

An interesting situation is that of a symmetric environment with $\epsilon_1 = \epsilon_3$. In this case it is possible to find simpler expressions for each solution, namely

$$\omega_{\text{opt}}: \quad \frac{\epsilon_2}{\kappa_2}\tanh(\kappa_2 d/2)+\frac{\epsilon_1}{\kappa_1}+i\frac{\sigma}{\omega\epsilon_0}=0 \ , \tag{4.50}$$

[6] At least in the case of a symmetrical dielectric environment, $\epsilon_1 = \epsilon_3$. If $\epsilon_1 \neq \epsilon_3$ phase-matching may be prevented in some circumstances.

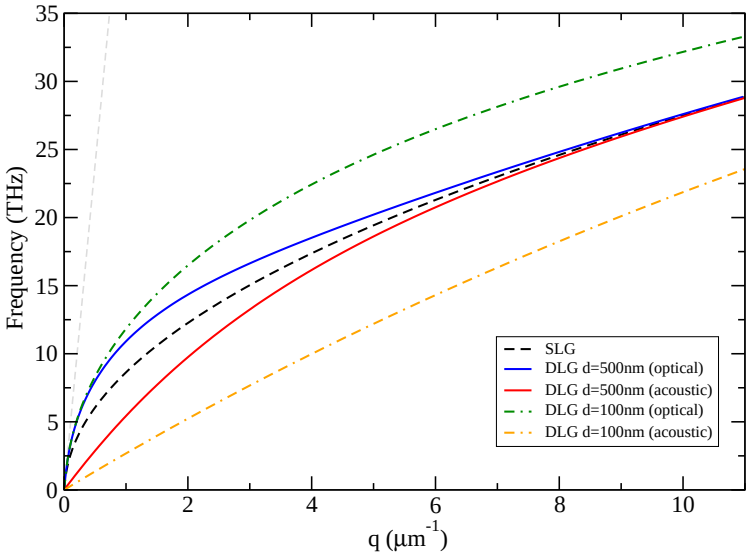


Figure 4.6: Spectrum of TM GSPs in a double-layer graphene structure. The interaction between SPPs in different graphene sheets splits the dispersion relation into two solutions: a higher frequency optical mode and a lower frequency acoustic mode. The dispersion curve of GSPs in single-layer graphene is shown as a black dashed curve for eye guidance. Parameters: $\epsilon_1 = \epsilon_2 = \epsilon_3 = 1$, $E_F = 0.45$ eV and $\gamma = 0$.

for the optical mode, and

$$\omega_{\text{ac}} : \quad \frac{\epsilon_2}{\kappa_2} \coth(\kappa_2 d/2) + \frac{\epsilon_1}{\kappa_1} + i\frac{\sigma}{\omega\epsilon_0} = 0 \ , \tag{4.51}$$

for the acoustic one.

Taking the non-retarded limit and assuming that the dielectrics are all made of the same material, i.e. $\epsilon \equiv \epsilon_1 = \epsilon_2 = \epsilon_3$, or within a naive "effective medium" approach, equation (4.48) reduces to

$$2\epsilon + i\frac{q\sigma}{\omega\epsilon_0}\left(1 \pm e^{-qd}\right) = 0 \ , \tag{4.52}$$

where the upper and lower signs correspond to the optical (symmetric) and acoustic (antisymmetric) solutions, respectively. The above expression could

also have been obtained from equations (4.50) and (4.51). If we consider that graphene's conductivity is roughly given by Drude's contribution with negligible damping, we can write an explicit formula for the GSPs frequency in double-layer graphene:

$$(\hbar\omega_{GSP})^2 \approx \frac{2\alpha}{\epsilon} E_F \hbar c q \left(1 \pm e^{-qd}\right) \ . \tag{4.53}$$

Naturally, for $qd \to \infty$ we recover the relation for the dispersion of GSPs in single-layer graphene.

Supplemented with the treatment outlined above, one could continue to stack as many graphener layers (separated by insulator slabs) as one wants [82, 83]. In general, for an arbitrary N-layer graphene configuration, the plasmon spectrum will consist in one optical branch and $N-1$ acoustic ones [84].

4.2.2 Field profile of GSPs in double-layer graphene

Analogously to what we did before in subsection 4.1.2, it is worthwhile to represent the full vectorial electromagnetic fields akin to GSPs modes in double-layer graphene. This will endow us with further insight on the characteristics of each one of the modes. To this end, we set $q_c = 1$ μm and then solve the dispersion relation (4.48) numerically, from which we end up with the pair of frequencies $\omega_{\rm opt}(q_c)$ and $\omega_{\rm ac}(q_c)$, corresponding to the optical and acoustic modes, respectively. Afterwards, one only needs to reconstruct the fields (4.39)-(4.42) accordingly, in a similar fashion to the case described in subsection 4.1.2 for monolayer graphene.

Figure 4.7 shows the resulting GSPs' electric field relative to the optical mode, whereas figure 4.8 displays the electric field corresponding to the acoustic mode. Clearly, the optical mode is made up of in-phase charge-density oscillations, while for the acoustic mode the charge-carriers in each graphene sheet oscillate out-of-phase. Notice that for the latter the inner medium experiences a large polarization, so that the charge densities on the two layers resemble a set of capacitors.

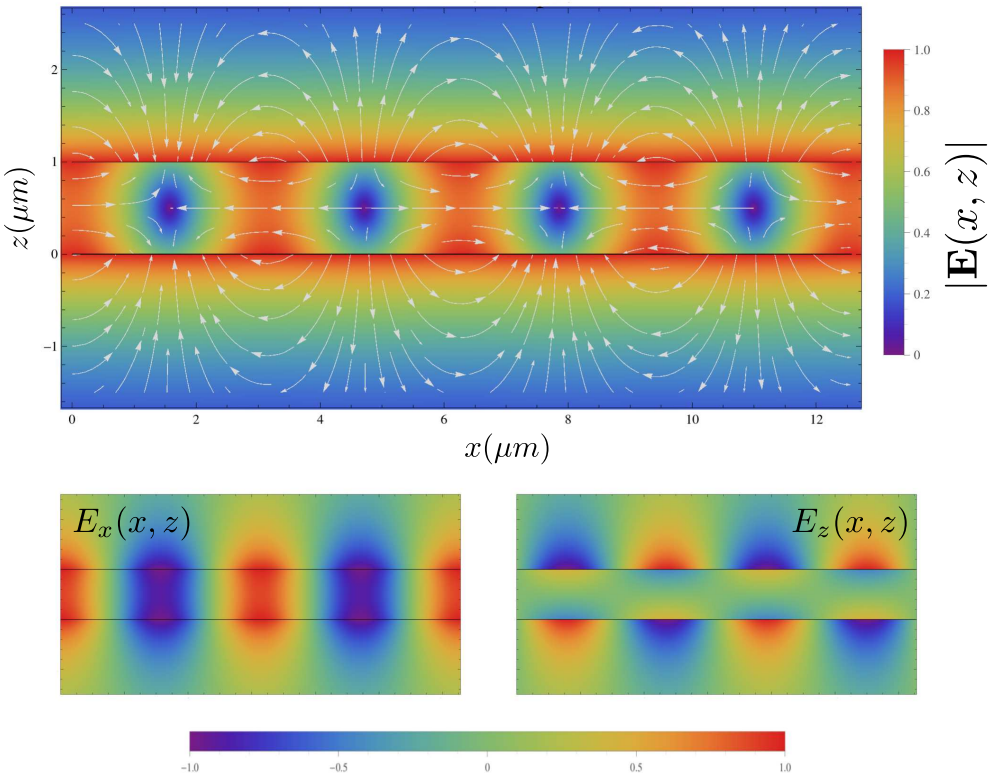


Figure 4.7: Illustration of the computed (vectorial) electric field corresponding to the optical mode, $\omega_{\text{opt}}(q_c)$. The top panels shows the respective field lines and the colour indicates its normalized magnitude. The panels at the bottom show density plots for each component separately (same xz-region as in the main figure). Parameters: $\epsilon_1 = \epsilon_3 = 1$, $\epsilon_2 = 4$, $d = 1$ μm, $E_F = 0.45$ eV and $\gamma = 0$.

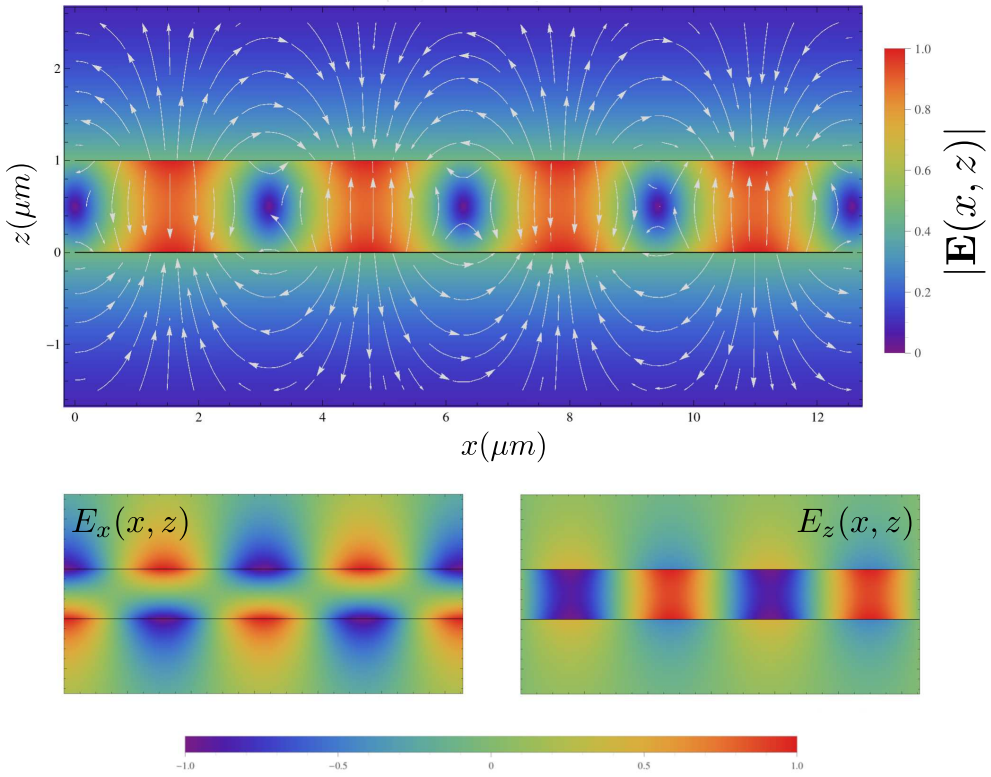


Figure 4.8: Same as in figure 4.7, but now relative to the acoustic mode, $\omega_{\rm ac}(q_c)$. Parameters: $\epsilon_1 = \epsilon_3 = 1$, $\epsilon_2 = 4$, $d = 1$ μm, $E_F = 0.45$ eV and $\gamma = 0$.

Chapter 5

Excitation of Graphene Surface Plasmons

In this Chapter we will briefly review several techniques for the excitation of GSPs. Recall from our previous discussion that, in general, it is not possible to couple an incident electromagnetic beam to a SPP in planar, extended graphene, due to a mismatch between the momentum of the impinging radiation and the GSP's momentum – the dispersion curve of the latter always lies to the right of the light line. This limitation is shared amongst graphene and ordinary metals. Thus, it should not come as a surprise that the very same mechanisms for exciting SPPs in metals also apply to the case of graphene.

5.1 Grating Coupling

The excitation of SPPs in graphene via grating coupling has been one of the most popular methods for exciting graphene's plasmon-polaritons [52, 53, 54, 85, 86, 87, 88]. The basic idea is to take advantage of the general principle from elementary optics that when a beam of light hits a grating structure, it gives rise to set of diffraction orders which carry "extra" momentum contributions, in multiples of $G = 2\pi/R$, defined by the grating period - see figure 5.1. Whenever a wavevector akin to a component of the diffracted

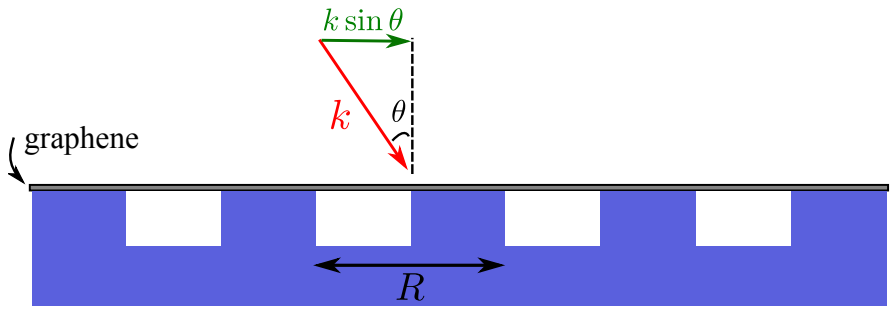


Figure 5.1: Example of a grating coupling scheme for exciting GSPs, in which a graphene sheet in placed on top of a patterned dielectric with period R.

light coincides to a certain SPP wavevector, the phase-matching condition[1]

$$q_{SPP} = k \sin\theta \pm nG \tag{5.1}$$

is fulfilled, with $k = \sqrt{\epsilon}\omega/c$ and $n \in \mathbb{Z}$, and excitation takes place. This condition is reciprocal, that is, when a propagating SPP enters in a grating-like region it can (re)couple to the radiation continuum.

We note that the configuration depicted in figure 5.1 is only one of many possible schemes for achieving grating coupling. That particular case was investigated analytically in Ref. [87]. In Chapter 7 we will consider yet another configuration, in which the grating is formed by graphene itself, patterned into an array of graphene ribbons. Hence, a detailed description of the coupling of electromagnetic radiation to GSPs using gratings can be found in the aforementioned chapter.

5.2 Prism Coupling

Another commom approach to overcome the kinematic limitation and to couple (p-polarized) photons to SPPs has been the excitation of SPPs via tunneling of evanescent waves originating from total internal reflection of light in a prism made of a higher-index dielectric (Kretschmann and Otto configurations). This can be attained by meeting the conditions: (i) ϵ_{prism}

[1]Note that this 1D condition can be straightforwardly generalized for two dimensions.

must be the higher than two dielectrics cladding the graphene layer; and (ii) the incident angle must be larger than the critical angle for total internal reflection, $\theta > \theta_c = \arcsin(\epsilon_{\text{diel.}}/\epsilon_{\text{prism}})$. Therefore, the wavevector of light is increased in the prism and it can now afford SPPs' excitation, whenever its in-plane component

$$q = \frac{\omega}{c}\sqrt{\epsilon_{\text{prism}}}\sin\theta \ , \tag{5.2}$$

matches the SPP wavevector. Figure 5.2 shows a diagrammatic representation of this technique[2]. Notice that depending on the impinging angle, θ, different wavevectors can be achieved within the shaded region between the light lines of the dielectric (here assumed to be the same, above and below graphene, for the sake of clarity) and the prism. Under this conditions

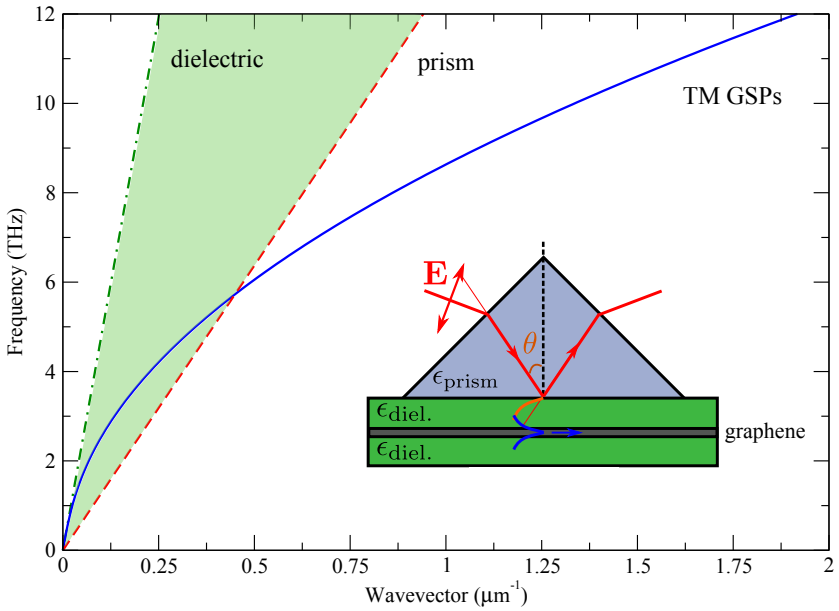


Figure 5.2: Schematic diagram depicting the principle behind the prism coupling technique for exciting GSPs. The inset depicts the coupling of light to GSPs, in the ATR regime, by evanescent tunneling. Doped graphene ($E_F = 0.45$ eV) is assumed to be cladded between one dielectric layer (top) and another semi-infinite dielectric (bottom) with $\epsilon_{\text{diel.}} = 1$. We further assumed that $\epsilon_{\text{prism}} = 14$.

[2]Neglecting the influence of the dielectric environment of the prism on the resonant condition.

SPP excitation is detected by observing the presence of a sharp minimum in reflectance – attenuated total reflection (ATR).

5.3 Near-field Excitation and Imaging of GSPs

The development of near-field optical microscopies opened up new possibilities to study the properties of SPPs directly and with nanometer resolution. This contrasts with the methods mentioned above, where excitation takes place over scales of the order of the illuminated spot size[3]. Under this scheme, the needed in-plane momentum is provided by the near-field evanescent components of light coming out from a very sharp tip of a SNOM (scanning near-field optical microscope) with aperture radius $r \ll \lambda_0$. Therefore, by bringing a graphene layer into the vicinity of the SNOM fiber tip, the excitation of GSPs with wavevectors up to $q \sim r^{-1}$ is possible via near-field coupling to the diffracted components of the light leaving the subwavelength aperture. These *locally* excited GSPs will propagate radially away from the source tip.

Recently, two independent research groups performed ground-breaking experiments on graphene plasmonics using a similar concept (though not exactly equivalent) [89, 90]. In their pioneering work, the experimentalists have been able not only to excite GSPs, but also to detect and image them. In this case, access to large wavevectors was achieved by illuminating the (sharp) oscillating tip of an atomic force microscope (AFM) with a focused infrared beam with $\lambda_0 = 11.2$ μm [89], thereby making the conducive tip behave as an antenna[4]. This scattering-type SNOM launches concentric ripples of GSPs propagating (while being damped) along a patch of gated graphene, until they are reflected at the sample edges (or defects). Thus, when the AFM apex is located at a distance $(n + 1/2)\lambda_p/2$ away from an edge, the reflected plasmon waves interfere constructively with the lauched plasmon waves, forming

[3]Which can be fairly macroscopic, or at least with dimensions comparable to the wavelength of the incoming radiation propagating in free space (i.e. diffraction-limited).

[4]Or, in other words, it induces an electric dipole at the AFM's tip.

fringes separated by half the plasmon wavelength, $\lambda_p/2$. The resulting standing (plasmon) waves constitute a convenient way to directly measure the GSP wavelength. Experimental measurements rendered plasmon wavelengths as small as $\lambda_p \approx 200$ nm [89], thus spatially concentrating electromagnetic radiation by a factor of $\lambda_0/\lambda_p = 56$. By tuning graphene's plasmonic properties using a back-gate, figures of merit in the interval $\lambda_0/\lambda_p = 50 - 60$ were reported [89].

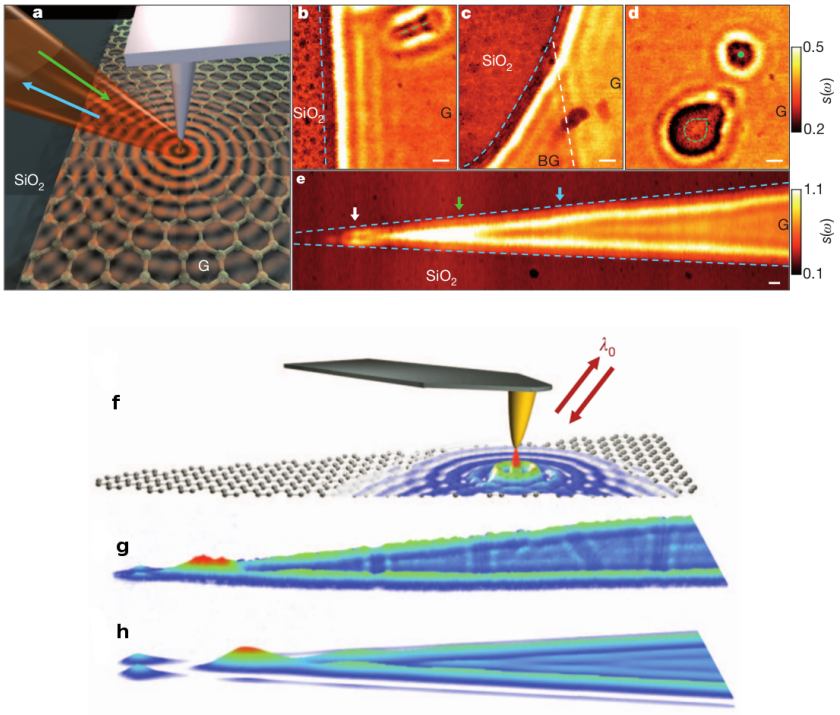


Figure 5.3: Infrared nano-imaging of GSPs. (a) illustration of the nano-imaging experimental setup. The launched GSPs are depicted as concentric red ripples propagating away from the AFM's apex upon illumination. The green and light-blue arrows indicate the incident and back-scattered light, respectively. (b – d) Recorded images of the interference patterns due to GSPs close to graphene edges or defects. (e) standing plasmon waves on a patch of graphene. (f) Diagram of the experimental configuration. (g) Experimentally obtained near-field amplitude image and (h) corresponding simulation based on the calculation of the local density of optical states. After Refs. [89] (a – e) and [90] (f – h).

Apart from the excitation capability, the other key feature that makes this technique particularly interesting is its ability to directly resolve and

image GSPs in real space (using the very same instrument, which in turn takes topographic data simultaneously). The so-called nano-imaging works by collecting the fields scattered by the tip. Since the back-scattered signal depends strongly on the distance between the tip shaft and the sample, the background and plasmonic contributions can be isolated by making the tip vibrate vertically at a given frequency (tappering mode), and then demodulating the detected signal. A schematic representation of the setup and nano-imaging technique is shown in figure 5.3.

5.4 Others

In the above we presented and reviewed the most recurrent mechanisms to effectively excite GSPs. Nonetheless, it should be noted that these are not the only available techniques.

For instance, surface plasmons can be readily excited using electron beams by means of electron energy loss spectroscopy (EELS). In fact, the first evidences of surface plasmons were obtained from electron beam experiments in the 1950s and 1960s [9, 10, 91]. Excitation takes places whenever one of the beam's electrons transfers energy, via inelastic scattering, to a resonant plasmon mode. By measuring the energy loss of the electron transmitted through the sample, the energy $\hbar\omega_{SPP}$ can be determined[5]. Moreover, if the scattered angle is also measured (angle-resolved EELS), one can combine this information to map the corresponding dispersion relation.

Other examples are the excitation of SPPs by light impinging on a randomly rough surface, a topological defect and/or surface features [16, 92, 93].

[5]Also, along with the SPP peak, another peak due to bulk plamons appears in the EELS spectrum at higher energies.

Chapter 6

Launching Plasmons using a Metal Contact

Another way of exciting graphene surface plasmon-polaritons (or SPPs in general) is to use a metallic contact placed on top of a graphene sheet. The presence of the contact will scatter an impinging electromagnetic wave and induce plasmons in the nearby graphene. Recently, applying a similiar reasoning, Alonso-González *et al* have experimentally demonstrated the excitation of GSPs using resonant metal antennas, consisting in micrometer-sized gold bars covering a graphene layer [94]. When illuminated with resonant light, these behave like an optical dipole which in turn drives the launch of plasmon-polaritons propagating through graphene.

Here we will consider a slightly different system, composed by an infinitely long metal stripe with width L, positioned on top of monolayer graphene. We will develop a theoretical platform [95] that aims to account for the system's response to an incoming electromagnetic wave and to describe the assisted launch of GSPs by the metal contact.

The system under consideration is depicted in figure 6.1. The graphene layer lies in the $z = 0$ plane and the metallic stripe is located on top of it, encompassing the $|x| < L/2$ region and centered at $x = 0$. We shall assume that the thickness of the metal contact is much smaller than the wavelength of the incident radiation, thus allowing us to treat the contact

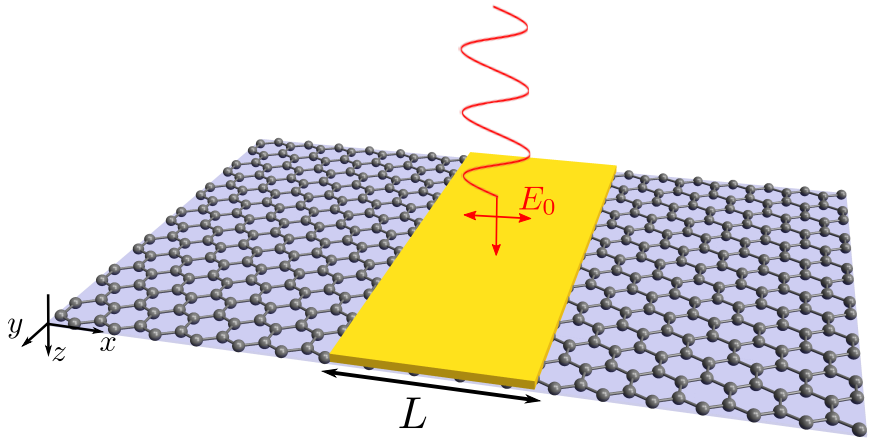


Figure 6.1: Scheme of a metal contact on graphene. The stripe has infinite length and width L. The whole system is illuminated with electromagnetic radiation linearly polarized along the width of the contact.

as a two-dimensional metal. Additionally, we further assume the limit of a highly conductive stripe, in which the system can be perceived as two disjoint graphene sheets linked through the metal contact. Let us now suppose that the structure is subjected to a frequency-dependent external electric field, in the form of a monochromatic electromagnetic wave which propagates along the positive z-direction, and has its polarization in the direction perpendicular to the metallic contact,

$$\mathbf{E}^{\text{ext}} = E_0 e^{i(k_z z - \omega t)} \hat{\mathbf{x}} \ , \tag{6.1}$$

with $k_z = \sqrt{\epsilon}\omega/c$, where ϵ refers to the relative permittivity of the embedding (homogeneous) medium. Then, under the assumptions outlined above, the linear response of the whole system can be written as

$$J_x(x) = \sigma_g(\omega) E_x(x,0) + [\sigma_m(\omega) - \sigma_g(\omega)]\, \Theta\left(L/2 - |x|\right) E_x(x,0) \ , \tag{6.2}$$

where we take the conductivities of graphene, σ_g, and of the metal, σ_m, as being independent of each other. Here, E_x stands for the x-component of the *total* electric field,

$$E_x = E_x^{\text{ext}} + E_x^{\text{ind}} \ , \tag{6.3}$$

which is the sum of the incident field with an induced field, arising from the system's response to the external perturbation. Note this is a function of both x and z. Due to the symmetry of the system, we will seek for solutions of the type $\mathbf{E} = (E_x, 0, E_z)$ and $\mathbf{B} = (0, B_y, 0)$. Moreover, since the structure possesses translational invariance along y-direction, we may write the x-component of the induced electric field as

$$E_x^{\rm ind}(x,z) = \int_{-\infty}^{\infty} E_x^{\rm ind}(q,z) e^{iqx - i\omega t} dq \ , \tag{6.4}$$

and similar relations apply for the other components, namely $E_z^{\rm ind}$, $B_y^{\rm ind}$ and also J_x. Hereafter, we will drop the $e^{-i\omega t}$ term in order to make the forthcoming equations simpler, but it should be noted that the harmonic time dependence is implicit. From Maxwell's equations,

$$\nabla \times \mathbf{E}^{\rm ind} = -\frac{\partial \mathbf{B}^{\rm ind}}{\partial t} \ , \tag{6.5}$$

$$\nabla \times \mathbf{B}^{\rm ind} = \frac{\epsilon}{c^2}\frac{\partial \mathbf{E}^{\rm ind}}{\partial t} + \mathbf{J} \ , \tag{6.6}$$

we obtain

$$B_y^{\rm ind}(q,z) = i\frac{\omega\epsilon}{c^2 k_q^2}\partial_z E_x^{\rm ind}(q,z) \ , \tag{6.7}$$

and

$$\partial_z^2 E_x^{\rm ind}(q,z) - k_q^2 E_x^{\rm ind}(q,z) = i\frac{k_q^2}{\omega\epsilon_0\epsilon} J_x(q)\delta(z) \ , \tag{6.8}$$

where $k_q^2 = q^2 - \epsilon\omega^2/c^2$ and ϵ_0 is the vacuum permittivity. Upon integration, equation (6.8) implies

$$\partial_z E_x^{\rm ind}(q,0^+) - \partial_z E_x^{\rm ind}(q,0^-) = i\frac{k_q^2}{\omega\epsilon_0\epsilon} J_x(q) \ , \tag{6.9}$$

provided that $E_x^{\rm ind}$ is continuous[1] across the boundary at $z = 0$. Further,

[1]Notice that this, along with equation (6.9) are equivalent to the usual boundary conditions we have seen in previous chapters.

equations (6.8) and (6.9) have solutions in the form of

$$E_x^{\text{ind}}(q,z) = -i\frac{k_q}{2\omega\epsilon_0\epsilon}J_x(q)e^{-k_q|z|} \ , \tag{6.10}$$

where k_q must be chosen in accordance with the following prescription

$$\begin{cases} k_q = \sqrt{q^2-\omega^2\epsilon/c^2} & \text{for} \quad q^2 > \omega^2\epsilon/c^2 \\ k_q = -i\sqrt{\omega^2\epsilon/c^2-q^2} & \text{for} \quad q^2 < \omega^2\epsilon/c^2 \end{cases} \ , \tag{6.11}$$

describing both evanescent waves and scattered outgoing (propagating) waves, respectively. We now introduce the Fourier transform of the current,

$$J_x(q) = \int_{-\infty}^{\infty}\frac{dx}{2\pi}J_x(x)e^{-iqx} \ , \tag{6.12}$$

which together with equation (6.10) enables us to write equation (6.4) as

$$E_x^{\text{ind}}(x,z) = -\frac{i}{4\pi\epsilon_0\epsilon\omega}\int_{-\infty}^{\infty}dqk_qe^{iqx-k_q|z|}\int_{-\infty}^{\infty}dx'J_x(x')e^{-iqx'} \ . \tag{6.13}$$

Recall that $J_x(x)$ is a function of the total electric field at $z = 0$, i.e. $E_x(x,0) = E_0 + E_x^{\text{ind}}(x,0)$, so that the computation of the induced field in equation (6.13) requires previous knowledge of $E_x^{\text{ind}}(x,0)$. Thus, in order to determine $E_x^{\text{ind}}(x,z)$, one needs find $E_x^{\text{ind}}(x,0)$ beforehand. To this end, plugging equation (6.2) into the definition (6.12), we obtain

$$J_x(q) = \sigma_g\left[E_0\delta(q) + E_x^{\text{ind}}(q,0)\right] + (\sigma_m-\sigma_g)\mathcal{I}(L,q) \ , \tag{6.14}$$

with

$$\mathcal{I}(L,q) = \int_{-L/2}^{L/2}\frac{dx'}{2\pi}E_x(x',0)e^{-iqx'} \ . \tag{6.15}$$

Using the result (6.14) in equation (6.10) for $z = 0$, we arrive to

$$E_x^{\text{ind}}(q,z=0) = -i\frac{k_q}{2\omega\epsilon_0\epsilon}\left[\sigma_gE_0\delta(q) + \sigma_gE_x^{\text{ind}}(q,0) + (\sigma_m-\sigma_g)\mathcal{I}(L,q)\right] \ , \tag{6.16}$$

which after some algebra reduces to

$$E_x^{\rm ind}(q,0) = \frac{1-\xi_q}{\xi_q}\left[E_0\delta(q) + \left(\frac{\sigma_m}{\sigma_g} - 1\right)\mathcal{I}(L,q)\right] \ , \tag{6.17}$$

where we have introduced the function

$$\xi_q = 1 + i\frac{\sigma_g k_q}{2\omega\epsilon_0\epsilon} \ . \tag{6.18}$$

Finally, transforming the expression for the induced field back to real space, while noting that $E_x^{\rm ind}(q,z) = E_x^{\rm ind}(q,0)e^{-k_q|z|}$, leads to

$$E_x^{\rm ind}(x,z) = \frac{1-\xi_0}{\xi_0}E_0 e^{ik_z|z|} + \left(\frac{\sigma_m}{\sigma_g} - 1\right)\int_{-\infty}^{\infty} dq \frac{1-\xi_q}{\xi_q}\mathcal{I}(L,q)e^{iqx-k_q|z|} \ . \tag{6.19}$$

As before, notice that to compute of $E_x^{\rm ind}(x,z)$ we must have determined $\mathcal{I}(L,q)$ [which in turn depends on $E_x^{\rm ind}(x,0)$]. We shall work towards that goal in what follows.

Approximate solution for $E_x^{\rm ind}(x,0)$ via Fourier expansion

Let us now take a step back and write the x-component of the *total* electric field at the $z=0$ plane, that is

$$\begin{aligned} E_x(x,0) &= E_0 + E_x^{\rm ind}(x,0) \\ &= \frac{1}{\xi_0}E_0 + \left(\frac{\sigma_m}{\sigma_g} - 1\right)\int_{-\infty}^{\infty} dq \frac{e^{iqx}}{\xi_q}\int_{-L/2}^{L/2}\frac{dx'}{2\pi}E_x(x',0)e^{-iqx'} \\ &\quad + \left(1 - \frac{\sigma_m}{\sigma_g}\right)\int_{-L/2}^{L/2} dx' E_x(x',0)\underbrace{\int_{-\infty}^{\infty}\frac{dq}{2\pi}e^{iq(x-x')}}_{\delta(x-x')} \ . \end{aligned} \tag{6.20}$$

Since $-L/2 < x' < L/2$, then the last term in equation (6.20) is non-zero only for $x = x' \in [-L/2, L/2]$, owing to the delta function. Therefore, from now on we will treat the electric field inside and outside the metal contact

separately. For the latter, the delta function does not contribute and we have

$$E_x^{\text{out}}(x,0) = \frac{1}{\xi_0}E_0 + \left(\frac{\sigma_m}{\sigma_g} - 1\right)\int_{-\infty}^{\infty} dq \frac{e^{iqx}}{\xi_q}\int_{-L/2}^{L/2}\frac{dx'}{2\pi}E_x^{\text{in}}(x',0)e^{-iqx'} \quad \text{with } |x| > L/2\ , \tag{6.21}$$

and for the field within the metal stripe we find

$$E_x^{\text{in}}(x,0) = \frac{\sigma_g}{\sigma_m}\frac{E_0}{\xi_0} + \left(1 - \frac{\sigma_g}{\sigma_m}\right)\int_{-\infty}^{\infty} dq \frac{e^{iqx}}{\xi_q}\int_{-L/2}^{L/2}\frac{dx'}{2\pi}E_x^{\text{in}}(x',0)e^{-iqx'} \quad \text{with } |x| < L/2\ . \tag{6.22}$$

Notice that in writing expressions (6.21) and (6.22) we have included the superscript "*in*" in the term $E_x^{\text{in}}(x',0)$ to emphasize that it corresponds to the field inside the metal contact, since the integration takes place only for $|x| < L/2$. Additionally, note that equation (6.22) represents an integral equation for the unknown function $E_x^{\text{in}}(x,0)$. On the other hand, we should stress that we can only determine E_x^{out} once we have calculated the electric field inside the metal stripe. Thus, in order to proceed, we must solve equation (6.22). With that in mind, we assume that $E_x^{\text{in}}(x,0)$ can be written as a Fourier expansion,

$$E_x^{\text{in}}(x,0) = \sum_{n=0}^{\infty} A_n \cos\left(\frac{2n\pi x}{L}\right)\ , \tag{6.23}$$

where we have chosen the cosines as basis functions due to the even symmetry of the problem. Inserting this representation into equation (6.22), we obtain

$$\sum_{n=0}^{\infty} A_n \cos\left(\frac{2n\pi x}{L}\right) = \frac{\sigma_g}{\sigma_m}\frac{E_0}{\xi_0} + \left(1 - \frac{\sigma_g}{\sigma_m}\right)\int_{-\infty}^{\infty} dq \frac{e^{iqx}}{\xi_q}\int_{-L/2}^{L/2}\frac{dx'}{2\pi}e^{-iqx'}\sum_{n=0}^{\infty} A_n \cos\left(\frac{2n\pi x'}{L}\right)\ . \tag{6.24}$$

Multiplying both sides of equation (6.24) by $\cos\left(\frac{2m\pi x}{L}\right)$ and integrating over $-L/2 \leq x \leq L/2$, results in

$$LA_0 = L\frac{\sigma_g}{\sigma_m}\frac{E_0}{\xi_0} + \left(1-\frac{\sigma_g}{\sigma_m}\right)\times \\ \times \sum_{n=0}^{\infty} A_n \int_{-\infty}^{\infty} dq \frac{e^{iqx}}{\xi_q} \int_{-L/2}^{L/2} dx \int_{-L/2}^{L/2} \frac{dx'}{2\pi} e^{-iqx'} \cos\left(\frac{2n\pi x'}{L}\right) \ ; \text{for } m = 0 \ , \tag{6.25}$$

and

$$\frac{L}{2}\sum_{n=0}^{\infty} A_n \delta_{n,m} = \left(1-\frac{\sigma_g}{\sigma_m}\right)\times \\ \times \sum_{n=0}^{\infty} A_n \int_{-\infty}^{\infty} dq \frac{e^{iqx}}{\xi_q} \int_{-L/2}^{L/2} dx \int_{-L/2}^{L/2} \frac{dx'}{2\pi} e^{-iqx'} \cos\left(\frac{2n\pi x'}{L}\right)\cos\left(\frac{2m\pi x}{L}\right) \ ; \text{for } m \neq 0 \ , \tag{6.26}$$

where we have used the integral identities arising from the orthogonality of this complete set of basis functions[2]. Performing the integrations over dx' and changing variables according to $u = qL$, equations (6.25) and (6.26) translate to

$$\frac{\sigma_g}{\sigma_m}\frac{E_0}{\xi_0} = A_0\left(1-\frac{4}{\pi}\left[1-\frac{\sigma_g}{\sigma_m}\right]\int_0^{\infty}\frac{du}{\xi_u}\frac{\sin^2(u/2)}{u^2}\right) \\ + \frac{4}{\pi}\left(1-\frac{\sigma_g}{\sigma_m}\right)\sum_{n=1}^{\infty}(-1)^{n+1}A_n\int_0^{\infty}\frac{du}{\xi_u}\frac{\sin^2(u/2)}{u^2-4n^2\pi^2} \ , \tag{6.27}$$

and

$$A_m\left(1-\frac{8}{\pi}\left[1-\frac{\sigma_g}{\sigma_m}\right]\int_0^{\infty}du\frac{u^2}{\xi_u}\frac{\sin^2(u/2)}{\left[u^2-4m^2\pi^2\right]^2}\right) \\ + \frac{8}{\pi}\left(1-\frac{\sigma_g}{\sigma_m}\right)\sum_{\substack{n=0\\ n\neq m}}^{\infty}(-1)^{n+m+1}A_n\int_0^{\infty}du\frac{u^2}{\xi_u}\frac{\sin^2(u/2)}{\left[u^2-4n^2\pi^2\right]\left[u^2-4m^2\pi^2\right]} = 0 \ , \tag{6.28}$$

[2]Explicitly, $\int_{-L/2}^{L/2}\cos\left(\frac{2n\pi x}{L}\right)\cos\left(\frac{2m\pi x}{L}\right)dx = \begin{cases}\frac{L}{2}\delta_{n,m} & \text{, if } n,m\neq 0\\ L & \text{, if } m=0\end{cases}$

respectively; here the function ξ_u now reads

$$\xi_u = 1 - \frac{E_F}{\hbar\omega}\frac{2\alpha\Omega_L}{\hbar\omega + i\hbar\gamma}\sqrt{u^2 - a^2}\ , \tag{6.29}$$

with the definitions $a = \sqrt{\epsilon}\frac{\hbar\omega}{\Omega_L}$ and $\Omega_L = \hbar c/L$, and where we have assumed a Drude-like conductivity for graphene, as given by expression (2.40). Together, equations (6.27) and (6.28) form a linear system of equations in terms of the Fourier coefficients, A_n. In other words, the above-mentioned expressions can be recasted as a matricial equation of the (typical) form $\mathbf{Ax} = \mathbf{b}$; that is, running the sums up to N, we have

$$\begin{pmatrix} C_0 & F_1 & F_2 & \cdots & \cdots & F_n \\ H_{0,1} & G_1 & H_{2,1} & \cdots & \cdots & H_{N,1} \\ \vdots & & \ddots & & & \vdots \\ H_{0,j} & \cdots & \cdots & G_j & \cdots & H_{N,j} \\ \vdots & & & & \ddots & \vdots \\ H_{0,N} & H_{1,N} & \cdots & \cdots & H_{N-1,N} & G_N \end{pmatrix} \begin{pmatrix} A_0 \\ A_1 \\ \vdots \\ A_j \\ \vdots \\ A_N \end{pmatrix} = \begin{pmatrix} \frac{\sigma_g}{\sigma_m}\frac{E_0}{\xi_0} \\ 0 \\ \vdots \\ 0 \\ \vdots \\ 0 \end{pmatrix} . \tag{6.30}$$

with

$$C_0 = 1 - \frac{4}{\pi}\left(1 - \frac{\sigma_g}{\sigma_m}\right)\int_0^\infty \frac{du}{\xi_u}\frac{\sin^2(u/2)}{u^2}\ , \tag{6.31}$$

$$F_n = \frac{4}{\pi}\left(1 - \frac{\sigma_g}{\sigma_m}\right)(-1)^{n+1}\int_0^\infty \frac{du}{\xi_u}\frac{\sin^2(u/2)}{u^2 - 4n^2\pi^2}\ , \tag{6.32}$$

$$G_m = 1 - \frac{8}{\pi}\left(1 - \frac{\sigma_g}{\sigma_m}\right)\int_0^\infty du\frac{u^2}{\xi_u}\frac{\sin^2(u/2)}{[u^2 - 4m^2\pi^2]^2}\ , \tag{6.33}$$

$$H_{n,m} = \frac{8}{\pi}\left(1 - \frac{\sigma_g}{\sigma_m}\right)(-1)^{n+m+1}\int_0^\infty du\frac{u^2}{\xi_u}\frac{\sin^2(u/2)}{[u^2 - 4n^2\pi^2][u^2 - 4m^2\pi^2]}\ . \tag{6.34}$$

Once the A_n's are determined from the solution of the matricial equation (6.30), we are able to construct the field inside the contact via

$$E_x^{\text{in}}(x, 0) = \sum_{n=0}^{N} A_n \cos\left(\frac{2n\pi x}{L}\right)\ , \tag{6.35}$$

[recall equation (6.23)] and then the field in graphene (outside the metal stripe) through equation (6.21), yielding

$$E_x^{\text{out}}(x,0) = \frac{1}{\xi_0}E_0 + \frac{2\eta_\sigma}{\pi}\sum_{n=0}^{N}(-1)^n A_n \int_0^\infty du \frac{\cos(ux/L)}{\xi_u}\frac{u\sin(u/2)}{u^2-4n^2\pi^2} \ . \quad (6.36)$$

where we have defined $\eta_\sigma = \sigma_m/\sigma_g - 1$. The first term in the previous equation represents the contribution coming from the uniform part of the structure. In the case where the contact is absent, this would be the only term[3]. Conversely, the second term in equation (6.36) accounts for the modification of the electric field induced by the metallic stripe. Also, note that the integral has poles whenever $\xi_u = 0$, corresponding to the excitation of plasmon-polaritons in graphene.

Results and discussion

Having the expressions for the fields, given by equations (6.35) and (6.36), we are now in position to investigate the behaviour of the in-plane electric field (at $z = 0$) in the system under consideration. Figure 6.2 shows the results obtained for both $E_x^{\text{in}}(x,0)$ and $E_x^{\text{out}}(x,0)$. Here we have plotted the fields for different contact widths, $L = f(\lambda)$, while keeping graphene's Fermi level constant - as well as the ratio $\sigma_m/\sigma_g \gg 1$ (highly conductive stripe) - for a fixed incident wavelength, λ_0. In the top panel we have represented the x-component of the electric field in graphene (i.e. outside the contact), which encompasses GSPs fields and also a contribution from the uniform part of the structure [described by the first term in equation (6.36)]. It is apparent from the figure that the system emits plasmon-polaritons travelling away from the metallic stripe exhibiting the characteristic subwavelength confinement and high field enhancement. For instance, in the case with $L = \lambda_0/2$ the GSP wavelength is about 19 times smaller than the wavelength of the impinging electromagnetic wave ($\lambda_p \simeq 0.052\lambda_0$), which is already a fair degree of confinement. Naturally, the plasmonic field weakens with increasing x/L due to

[3]Notice that if one replaces the contact by a patch of graphene ($\sigma_m \to \sigma_g$), restoring the system's homogeneity, the second term gives a null contribution.

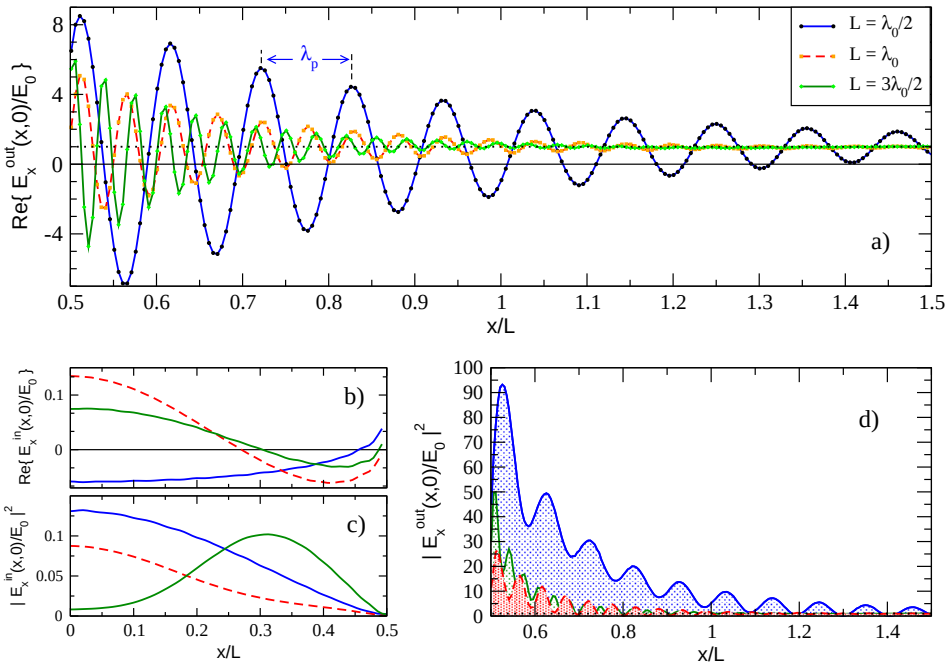


Figure 6.2: In-plane electric fields, both within the metal stripe, $E_x^{\text{in}}(x,0)$, and in graphene, $E_x^{\text{out}}(x,0)$, as a function of x/L for different contact widths. All fields were normalized with respect to the amplitude of the incident electromagnetic wave. The top panel shows the real part of $E_x^{\text{out}}(x,0)/E_0$ as given by equation (6.36), while the bottom right panel shows its absolute value squared. The fields inside the contact are plotted in the two panels at lower left. We used the following parameters: $\epsilon = 1$, $\lambda_0 = 10.2$ μm (corresponding to $\hbar\omega = 0.12$ eV or $\omega = 2\pi \times 30$ THz), $E_F = 0.44$ eV, $\hbar\gamma = 5$ meV and $\sigma_g/\sigma_m = 0.01$ (highly conductive stripe).

the Ohmic losses within graphene. Thus, at large distances away from the contact the field becomes indistinguishable from the response of the homogeneous system, so that $E_x^{\text{out}}(x,0)/E_0 \to \xi_0^{-1}$ (depicted in the figure as a black dotted line). Albeit not particularly enlightening, the field inside the stripe is portrayed in the two panels – b) and c) – at lower left. Every panel in figure 6.2 shows a strong dependence on the ratio L/λ_0, which is expected since the width of the contact is of the order of the impinging wavelength. In particular, we expect the absorption of light by the stripe to be a function

of the frequency (or wavelength), attaining a maximum efficiency whenever $L = (n+1/2)\lambda_0$ with $n = 0, 1, ...$, and minima for $L = n\lambda_0$. This can be seen in figure 6.2 by looking at panels c) and d) depicting the modulus squared of the fields – proportional to the electric field intensity – which show the highest values for odd multiples of $\lambda_0/2$. Even so, we note that the best configuration for exciting high-intensity GSPs via the metal antenna is when $L = \lambda_0/2$, which corresponds to the first resonance [cf. panel d) in figure 6.2]. For this reason, hereafter we will focus our attention on this particular case.

We now consider not only the in-plane field's fraction, but rather the induced electric field in the whole space. Therefore, using equations (6.19) and (6.10) and proceeding in the same fashion as before, the x-component of the induced field reads

$$E_x^{\mathrm{ind}}(x,z) = \frac{1-\xi_0}{\xi_0} E_0 e^{ik_z|z|} + \frac{2\eta_\sigma}{\pi} \sum_{n=0}^{\infty} (-1)^n A_n \int_0^\infty du \frac{1-\xi_u}{\xi_u} \frac{u \sin(u/2)}{u^2 - 4n^2\pi^2} \cos(ux/L) e^{-k_u|z|/L} \,. \tag{6.37}$$

Once more, we observe that the field expressed in equation (6.37) can be split into two distinct contributions. The first term describes the scattering of the incident electromagnetic wave by the uniform system, i.e. without the contact; thus, it is independent of the x coordinate and represents scattered waves propagating along the z-direction: with reflected waves for $z < 0$ and transmitted waves for $z > 0$. On the other hand, the last term characterizes the screening and the system's response to the inhomogeneity introduced by the metal stripe. For this reason, we shall denote the second term by E_x^{2D}, i.e.

$$E_x^{\mathrm{2D}}(x,z) \equiv \frac{2\eta_\sigma}{\pi} \sum_{n=0}^{\infty} (-1)^n A_n \int_0^\infty du \frac{1-\xi_u}{\xi_u} \frac{u \sin(u/2)}{u^2 - 4n^2\pi^2} \cos(ux/L) e^{-k_u|z|/L}. \tag{6.38}$$

In addition, we note that the above integral contains two different kinds of fields: those in the form of evanescent waves confined near the graphene sheet, when $u > a$; and those corresponding to propagating waves, when $u < a$ (the surface plasmons consist in the former type of fields).

At this point the only item missing in our list is the component of the induced field perpendicular to the structure, that is to say, $E_z^{\text{ind}}(x,z)$. We can retrieve this last piece of information working through Maxwell's equations, which link E_x^{ind}, B_y^{ind} and E_z^{ind}, namely

$$E_z^{\text{ind}}(x,z) = i\frac{c^2}{\omega\epsilon}\partial_x B_y^{\text{ind}}(x,z) \ , \tag{6.39}$$

and

$$B_y^{\text{ind}}(q,z) = i\frac{\omega\epsilon}{c^2 k_q^2}\partial_z E_x^{\text{ind}}(q,z) \tag{6.40}$$

$$= -\frac{\text{sgn}(z)}{2\epsilon_0 c^2} J_x(q) e^{-k_q|z|} \ , \tag{6.41}$$

where in the last step we used equation (6.10). Taking the inverse Fourier transform and inserting the previous expression into equation (6.39) yields

$$E_z^{\text{ind}}(x,z) = \frac{\text{sgn}(z)}{2\omega\epsilon_0\epsilon}\int_{-\infty}^{\infty} q J_x(q) e^{iqx - k_q|z|} dq \ . \tag{6.42}$$

Finally, using equation (6.14) for $J_x(q)$ and changing variables yet again to $u = qL$, one obtains (after some algebra):

$$E_z^{\text{ind}}(x,z) = -\,\text{sgn}(z)\frac{2\eta_\sigma}{\pi}\sum_{n=0}^{\infty}(-1)^n A_n \int_0^\infty du \frac{1-\xi_u}{\xi_u}\frac{\sin(ux/L)}{k_u}\frac{u^2\sin(u/2)}{u^2 - 4n^2\pi^2}e^{-k_u|z|/L}$$

$$\equiv E_z^{\text{2D}}(x,z) \ . \tag{6.43}$$

Notice that for the z-component of the induced field we have $E_z^{\text{ind}} = E_z^{\text{2D}}$, since we are restricting ourselves to the particular case of a normally incident wave with p-polarization. For the sake of completeness, let us make the remark that in the more general situation with an arbitrary angle of incidence, E_z^{ind} would have an extra contribution (analogous to the one in E_x^{ind})

describing scattered waves.

At this point we have complete knowledge of the induced field, and hence also of $\mathbf{E}^{2\mathrm{D}} = \left(E_x^{2\mathrm{D}}, 0, E_z^{2\mathrm{D}}\right)$. The components of the latter as a function of the spatial coordinates are shown in figure 6.3. Recall that this corresponds to the two-dimensional electric field in which GSPs are included. Furthermore, we note that the results depicted in figure 6.3 refer to the case where the width of the metal contact is $\lambda_0/2$, which corresponds to the configuration capable of achieving the highest efficiency to excite GSPs. In panel a) we have represented a two-dimensional plot of $\Re\{E_x^{2\mathrm{D}}/E_0\}$ in the $z = 0$ plane. Owing to the system's translational invariance along the y-direction, we observe a set of high- and low-intensity fringes parallel to the edge of the stripe, decaying as we move away from it. Note that for the chosen value of γ (which is rather reasonable), the decay experienced by the GSPs is rather weak as they can propagate for several plasmon-polaritons wavelengths. Also shown in the

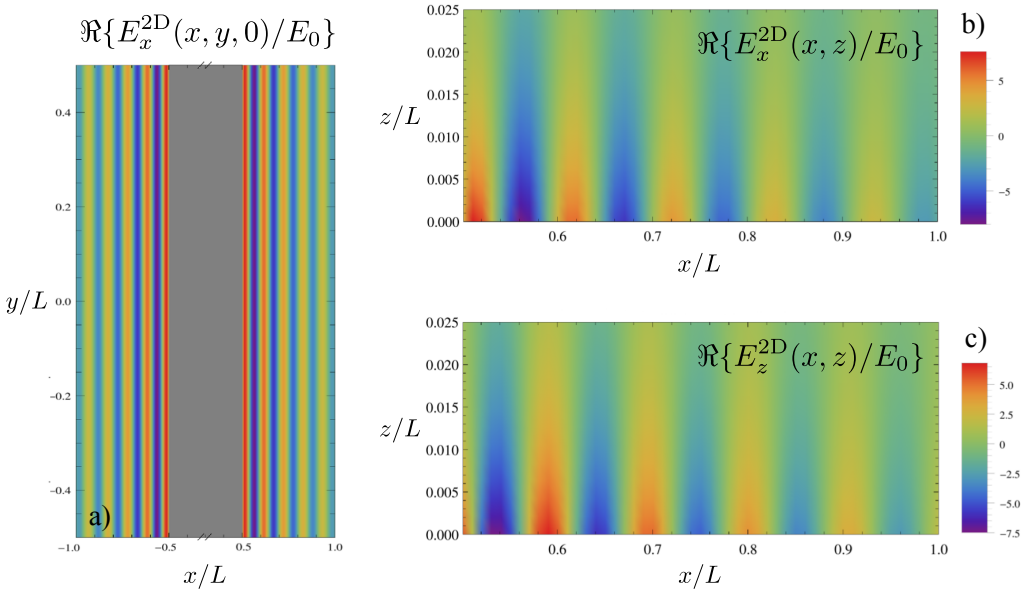


Figure 6.3: Real part of $E_x^{2\mathrm{D}}$ and $E_z^{2\mathrm{D}}$ normalized with respect to the incoming wave's amplitude. In panel a), notice the break on the x-axis. The rectangle in gray represents the contact. In all panels we considered $L = \lambda_0/2$, that is the condition for the first resonance of the antenna-like metallic stripe. The remaining parameters were the same as in figure 6.2.

figure is the dependence of $\Re\{E_x^{2D}/E_0\}$ and $\Re\{E_z^{2D}/E_0\}$ on the (x, z) coordinates. Both exhibith the typical plasmonic behaviour, with strong fields highly localized near the graphene layer and subwavelength confinement. In particular, from the numerical results we have obtained $\lambda_p = 0.052\lambda_0$ for the GSPs' wavelength. At the same time, from the figure we can see that the field at $z = 0.025L = 1.25 \times 10^{-2}\lambda_0$ in the dielectric is already about half of its top value. Together, these lead to a large concentration of electromagnetic energy within a very small volume.

While figure 6.3 depicts E_x^{2D} and E_z^{2D} separately, it is instructive to gather all this information into a vectorial representation of $\mathbf{E}^{2D}$. Taking this into consideration, we show in figure 6.4 the electric field lines corresponding to $\mathbf{E}^{2D}(x, z)$. These illustrate well the nature of plasmon-polaritons as collective oscillations in the density of charges, and support our interpretation of the problem confirming that this is indeed essentially a plasmonic field.

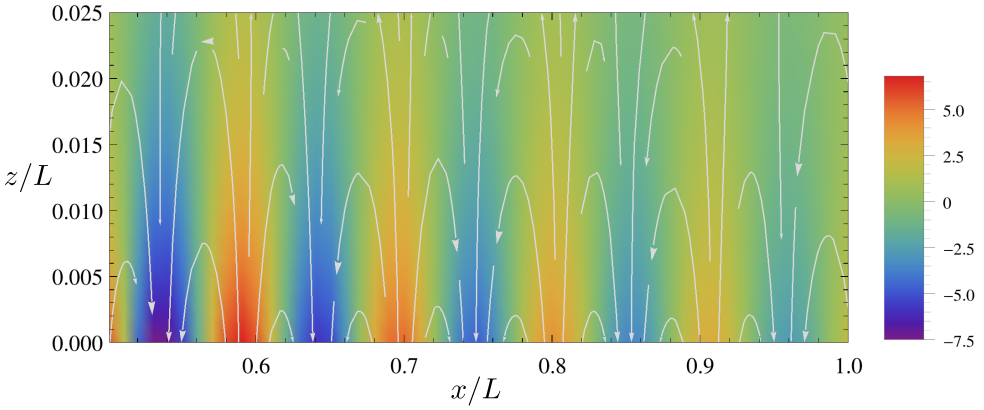


Figure 6.4: Representation of vectorial field $\mathbf{E}^{2D}(x, z)$ in terms of its field lines. These give us a hint of the regions where the concentration of charge carriers is higher (at a given moment, e.g. $t = 0$). The background and respective colorbar refers to the value of $\Re\{E_z^{2D}/E_0\}$ [cf. panel c) in figure 6.3].

Thus, our calculations demonstrate the ability to lauch GSPs using light and a highly conducive contact on graphene, endowing us with another method to excite plasmon-polaritons beyond the costumary techniques like prism or grating coupling.

Chapter 7

Plasmonics in Periodic Graphene-based Structures

The recent developments in nanofabrication techniques and theoretical/computational modelling have brought plasmonics to the nanoscale, leading to the birth of nanoplasmonics. Recently, the realization of surface plasmon-polaritons in graphene [52] has drawn a lot of attention, and research in graphene plasmonics is intense and likely to remain one of the hottest topics in nanophotonics in the forthcoming years. Particular interest has been given to the excitation of GSPs in periodic graphene-based structures, including corrugated graphene [50, 96], diffraction gratings, graphene plasmonic crystals and metamaterials [52, 53, 88], and also conductivity gratings (in which graphene's conductivity is periodically modulated) [86]. Among these are included arrays of graphene ribbons arranged periodically [52, 53, 88], which will be the main subject throughout this Chapter.

We will begin with a concise description of the theoretical framework in the most general case of a graphene sheet with a periodically modulated conductivity on a dielectric substrate. This can be achieved in several ways, such as: placing adsorbed atoms or molecules which modify the LDOS, via spatially-periodic electrical gating, inducing strain, and/or patterning an initially homogeneous graphene layer by employing nanofabrication methods. Here we will investigate the coupling of electromagnetic radiation to GSPs in

a periodic array of graphene ribbons [50, 52], by solving the scattering problem and computing the transmittance, reflectance and absorbance of plane waves impinging upon the aforementioned system. These results will then be compared against experimental results [52].

7.1 Theoretical Model

We note that although the theoretical model we will develop in the following lines will ultimately be applied to a periodic grating of graphene ribbons, the very same formalism is applicable to any arbitrary (2D) system with periodically modulated conductivity.

7.1.1 Setting up the model

Let us consider a generic bidimensional system with a spatially-dependent periodic conductivity, satisfying $\sigma(x) = \sigma(x + R)$. Here R defines the period of the structure, which can be seen as a one-dimensional (1D) crystal with lattice constant R, allowing us to define the corresponding reciprocal lattice vector, $G = 2\pi/R$. In resemblance to other periodic systems (e.g. an electron

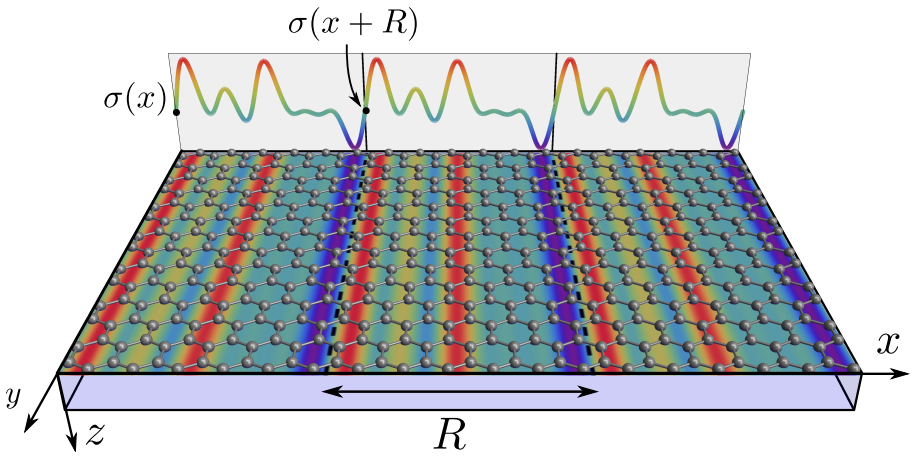


Figure 7.1: Schematic representation of a graphene sheet with an arbitrary spatially-dependent periodic conductivity, such that $\sigma(x) = \sigma(x + R)$, where R is the period of the system. The curve depicts an arbitrary periodic profile for the conductivity, while the colours reflect its corresponding value (a.u.).

subjected to a periodic potential in a solid), the electromagnetic fields follow Bloch's theorem. Therefore, we will seek for transverse magnetic SPP Bloch waves in the form of a Fourier-Floquet series, i.e.

$$\mathcal{E}_x^{(j)}(x,z) = \sum_{n=-\infty}^{\infty} E_{x,n}^{(j)} e^{i(q+nG)x} e^{-\kappa_{j,n}|z|} \ , \tag{7.1}$$

$$\mathcal{E}_z^{(j)}(x,z) = \sum_{n=-\infty}^{\infty} E_{z,n}^{(j)} e^{i(q+nG)x} e^{-\kappa_{j,n}|z|} \ , \tag{7.2}$$

$$\mathcal{B}_y^{(j)}(x,z) = \sum_{n=-\infty}^{\infty} B_{y,n}^{(j)} e^{i(q+nG)x} e^{-\kappa_{j,n}|z|} \ , \tag{7.3}$$

where the index $j = 1$ refers to the substrate ($z > 0$), and $j = 2$ to the top dielectric media ($z < 0$), whose electromagnetic properties are fully characterized by the relative permittivities ϵ_1 and ϵ_2, respectively. If we take the system as being linear, then each Fourier component is independent of the others, so that the following relations can be obtained from Maxwell's equations:

$$B_{y,n}^{(j)} = -i\,\mathrm{sgn}(z)\frac{\epsilon_j \omega}{c^2 \kappa_{j,n}} E_{x,n}^{(j)} \ , \tag{7.4}$$

$$B_{y,n}^{(j)} = -\frac{\epsilon_j \omega / c^2}{q + nG} E_{z,n}^{(j)} \ , \tag{7.5}$$

$$E_{z,n}^{(j)} = i\,\mathrm{sgn}(z)\frac{q + nG}{\kappa_{j,n}} E_{x,n}^{(j)} \ , \tag{7.6}$$

$$\kappa_{j,n} = \sqrt{(q + nG)^2 - \epsilon_j \omega^2 c^2} \ . \tag{7.7}$$

Notice the similarity between equations (7.4)-(7.7) and (4.8)-(4.10), where $q \to q + nG$ for each corresponding diffraction order. This is a natural consequence of the system's periodicity, since now the momentum can be defined up to a reciprocal lattice vector[1]. We proceed by introducing the boundary conditions of the problem (at $z = 0$), which require the continuity

[1]Note that a photon, an electron, etc, placed at a given q will *see* the same landscape as its counterpart at $q + nG$, for any $n \in \mathbb{Z}$.

of the tangential component of the electric field

$$\begin{aligned} &\mathcal{E}_x^{(2)}(x,0) - \mathcal{E}_x^{(1)}(x,0) = 0 \\ \Leftrightarrow &\sum_n \left[E_{x,n}^{(2)} - E_{x,n}^{(1)}\right] e^{inGx} = 0 \ , \end{aligned} \tag{7.8}$$

and the discontinuity of the magnetic field due to the presence of a surface charge density,

$$\begin{aligned} &\mathcal{B}_y^{(2)}(x,0) - \mathcal{B}_y^{(1)}(x,0) = \mu_0 \sigma(x) \mathcal{E}_x^{(1)}(x,0) \\ \Leftrightarrow &\sum_n \left[B_{y,n}^{(2)} - B_{y,n}^{(1)}\right] e^{inGx} = \mu_0 \sum_{m,l} \tilde{\sigma}_m E_{x,l}^{(1)} e^{i(m+l)Gx} \ , \end{aligned} \tag{7.9}$$

where the sums run for integers $\in \,]-\infty, \infty[$, and we have written the spatially modulated conductivity as a Fourier series,

$$\sigma(x) = \sum_m \tilde{\sigma}_m e^{imGx} \ , \tag{7.10}$$

with

$$\tilde{\sigma}_m = \frac{1}{R} \int_0^R \sigma(x) e^{-imGx} dx \ , \tag{7.11}$$

akin to the periodicity of the system. In what follows, it is convenient to redefine the index in the RHS of equation (7.9) as $m = n - l$. Then, equations (7.8) and (7.9) can be rewritten as

$$E_{x,n}^{(2)} - E_{x,n}^{(1)} = 0 \ , \tag{7.12}$$

$$B_{y,n}^{(2)} - B_{y,n}^{(1)} = \mu_0 \sum_l \tilde{\sigma}_{n-l} E_{x,l}^{(1)} \ . \tag{7.13}$$

Combining these expressions and making use of relation (7.4), we arrive at

$$\left(\frac{\epsilon_1}{\kappa_{1,n}} + \frac{\epsilon_2}{\kappa_{2,n}} \right) E_{x,n}^{(1)} + \frac{i}{\omega \epsilon_0} \sum_l \tilde{\sigma}_{n-l} E_{x,l}^{(1)} = 0 \ , \tag{7.14}$$

which is a non-linear eigenvalue problem, whose eigenvalue is the frequency, ω. The solution of equation (7.14) yields the band structure of the polaritonic spectrum in a system where graphene's conductivity is periodic.

Unfortunately, for the configuration of interest in this work – that of a periodic array of graphene ribbons – the numerical solution of the eigenvalue problem is poorly convergent, due to the sharp discontinuity of the conductivity across the edges of the ribbons. However, for systems with continuous variations of the conductivity, the plasmonic spectrum can be readily obtained; the case of a graphene sheet with cosine-modulated conductivity was adressed in Refs. [50, 97] using this technique.

7.1.2 The scattering problem

In contrast to the case of an homogeneous system, here the momentum is defined up to a reciprocal lattice vector [recall our discussion after equations (7.4)-(7.7) and (4.8)-(4.10)]; thus, the system's periodicity provides the extra momentum contribution needed to excite SPPs, as their momentum is larger than the one carried by the incident light beam.

Let us now consider the scattering of electromagnetic radiation impinging on a graphene sheet with periodically modulated conductivity and its coupling to GSPs in the form of Bloch-type surface waves. Since the system is periodic, its translational symmetry allows us to use Bloch's theorem to write the electromagnetic fields. For transverse magnetic (p-polarized) waves these can be written as

$$\mathcal{E}_x^{(j)}(x,z) = E_x^{inc} e^{iqx} e^{ik_z z}\delta_{j,2} + \sum_n E_{x,n}^{(j)} e^{i(q+nG)x} e^{-\kappa_{j,n}|z|} \ , \tag{7.15}$$

$$\mathcal{E}_z^{(j)}(x,z) = E_z^{inc} e^{iqx} e^{ik_z z}\delta_{j,2} + \sum_n E_{z,n}^{(j)} e^{i(q+nG)x} e^{-\kappa_{j,n}|z|} \ , \tag{7.16}$$

$$\mathcal{B}_y^{(j)}(x,z) = B_y^{inc} e^{iqx} e^{ik_z z}\delta_{j,2} + \sum_n B_{y,n}^{(j)} e^{i(q+nG)x} e^{-\kappa_{j,n}|z|} \ , \tag{7.17}$$

where $q = k\sin\theta$, $k_z = k\cos\theta$ and $\kappa_{j,n} = \sqrt{(q+nG)^2 - \epsilon_j\omega^2/c^2}$ with $k = \sqrt{\epsilon_2}\omega/c$ and $G = 2\pi/R$. The indices $j = 1, 2$ refer to the substrate and to the top dielectric media, respectively, with dielectric constants ϵ_1 and ϵ_2. We consider that light comes from medium 2. Note that whenever $(q+nG)^2 > \epsilon_j\omega^2/c^2$ we have an electromagnetic wave confined to the interface (surface electromagnetic wave), while for $(q+nG)^2 < \epsilon_j\omega^2/c^2$ we have a propagating

wave. The relations between the amplitudes of the n-th component of the electric and magnetic fields are once again given by expressions (7.4)-(7.7). In order to meet the boundary conditions, we must impose

$$E_x^{inc} + E_{x,0}^{(2)} = E_{x,0}^{(1)} \quad ; \quad \text{for } n = 0 \ , \tag{7.18}$$

$$E_{x,n}^{(2)} = E_{x,n}^{(1)} \quad ; \quad \text{for } n \neq 0 \ , \tag{7.19}$$

and

$$B_{y,0}^{(1)} - B_y^{inc} - B_{y,0}^{(2)} + \mu_0 \sum_l \tilde{\sigma}_{-l} E_{x,l}^{(1)} = 0 \quad ; \quad \text{for } n = 0 \ , \tag{7.20}$$

$$B_{y,n}^{(1)} - B_{y,n}^{(2)} + \mu_0 \sum_l \tilde{\sigma}_{n-l} E_{x,l}^{(1)} = 0 \quad ; \quad \text{for } n \neq 0 \ , \tag{7.21}$$

where the Fourier components of the conductivity follow the same prescription as before [see, for instance, equation (7.10)]. Equations (7.18)-(7.21), after some algebra and indentifications, reduce to the following system of equations

$$\left(\frac{\epsilon_1}{\kappa_{1,0}} + \frac{\epsilon_2}{\kappa_{2,0}} \right) E_{x,0}^{(1)} + \frac{i}{\omega \epsilon_0} \sum_l \tilde{\sigma}_{-l} E_{x,l}^{(1)} = i \frac{2\epsilon_2}{k_z} E_x^{inc} \ , \tag{7.22}$$

$$\left(\frac{\epsilon_1}{\kappa_{1,n}} + \frac{\epsilon_2}{\kappa_{2,n}} \right) E_{x,n}^{(1)} + \frac{i}{\omega \epsilon_0} \sum_l \tilde{\sigma}_{n-l} E_{x,l}^{(1)} = 0 \ . \tag{7.23}$$

We note that this system can be casted as a matricial equation, whose solutions (for a given ω) are just the amplitudes of the electric field[2]. These shall be obtained numerically using LAPACK's implemented routines for linear algebra[3]. Having computed the fields, we are now able to calculate the transmittance and reflectance of light by the structure, which read

$$\mathcal{T} = \sum_n \mathcal{T}_n \qquad \text{with} \qquad \mathcal{T}_n = \frac{\epsilon_1}{\epsilon_2} \frac{k_z}{|\kappa_{1,n}|} \left| \frac{E_{x,n}^{(1)}}{E_x^{inc}} \right|^2 \ , \tag{7.24}$$

[2]For numerical purposes, it is useful to normalize the field amplitudes in the system constituted by equations (7.22) and (7.23) with respect to E_x^{inc}.

[3]We note that the convergence of the numerical solution for the scattering problem is good, even for the rather "extreme" case of a grating of graphene ribbons, in constrast to the computation of the polaritonic bandstructure via equation 7.14.

and

$$\mathcal{R} = \sum_n \mathcal{R}_n \qquad \text{with} \qquad \mathcal{R}_n = \frac{k_z}{|\kappa_{2,n}|} \left| \frac{E^{(2)}_{x,n}}{E^{inc}_x} \right|^2 , \tag{7.25}$$

respectively[4]. From these, we define the absorbance as

$$\mathcal{A} = 1 - \mathcal{T} - \mathcal{R} , \tag{7.26}$$

where we should stress that in this expressions *only* the diffraction orders corresponding to propagating modes should be taken into account.

7.2 Applications and Results

In the previous section we developed a theoretical model describing the interaction of electromagnetic radiation with single-layer graphene whose conductivity is a periodic function. Here, we will apply this formalism to the specific case of a periodic arrangement of graphene micro-ribbons, and compare our results with experimental data from Ref. [52].

7.2.1 Periodic array of graphene ribbons

The first experimental demonstration of the existence of surface plasmon-polaritons in graphene was achieved by Ju *et al* in 2011, using a periodic array of graphene micro-ribbons, dubbed as a metamaterial by the authors [52]. Shorty after that, a theoretical account for the experiment was given [88], and since then an increasing number of publications followed [50, 53, 54, 96]. However, the results found in the literature are somewhat sparse and most of the theoretical work describing real experiments was based on finite element or FDTD numerical solutions obtained from commercial codes. Although these usually yield good results, they are computationally demanding, time-consuming and it is harder to get a "*feeling*" on the physics of the problem.

In what follows, we aim to fill this gap by employing the analytical theory discussed in the previous section, to the case of a periodic set of graphene

[4]For a detailed derivation of the expressions for $\mathcal{T}$ and $\mathcal{R}$, please refer to section's A.1 of Appendix A.

ribbons forming a grating-like structure as depicted in figure 7.2.

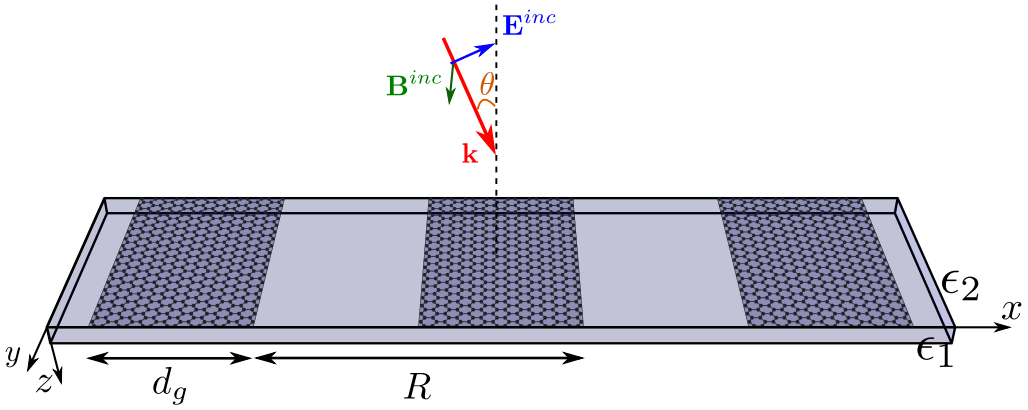


Figure 7.2: Illustration of a p-polarized plane wave impinging on a periodic array of graphene ribbons. The size of the unit cell is R and the width of the ribbons d_g. The substrate and capping layer are assumed to be semi-infinite dielectrics.

Notice that the formalism we have built in section 7.1 is completely general, so that now we only need to specify what are the Fourier coefficients of the conductivity, which enter in the linear system composed by following pair of equations [cf. expressions (7.22) and (7.23)]

$$\left(\frac{\epsilon_1}{\kappa_{1,0}} + \frac{\epsilon_2}{\kappa_{2,0}}\right) E^{(1)}_{x,0} + \frac{i}{\omega\epsilon_0}\sum_l \tilde{\sigma}_{-l} E^{(1)}_{x,l} = i\frac{2\epsilon_2}{k_z} E^{inc}_x \ , \tag{7.27}$$

$$\left(\frac{\epsilon_1}{\kappa_{1,n}} + \frac{\epsilon_2}{\kappa_{2,n}}\right) E^{(1)}_{x,n} + \frac{i}{\omega\epsilon_0}\sum_l \tilde{\sigma}_{n-l} E^{(1)}_{x,l} = 0 \ . \tag{7.28}$$

Recalling equation (7.11), we have

$$\tilde{\sigma}_l = \frac{\sigma_g}{R}\int_0^R s(x) e^{-ilGx} dx \ , \tag{7.29}$$

where $s(x)$ is determined by the spatial configuration of the system and we shall assume a bulk-like conductivity for the graphene ribbons[5]. As noted in subsection 2.3.1, in the terahertz and mid-IR spectral range and for standard

[5]This should be a valid approximation (at least) as long as $d_g k_F \gg 1$ and/or $d_g \gg l_{mfp}$, where $k_F = E_F/(\hbar v_F)$ is graphene's Fermi momentum and l_{mfp} the mean free path of the charge carriers. In addition, a study [98] suggested that quantum finite-sized and edge effects in graphene plasmons are only significant for ribbons smaller than 20 nm, which is well below the width of the structures considered in this work.

levels of doping ($E_F \gg k_B T$ and $2E_F > \hbar\omega$), graphene's conductivity reduces to Drude's contribution, (2.40). Thus, hereafter we will assume that $\sigma_g = \sigma_g^{\text{Drude}}$ unless otherwise stated.

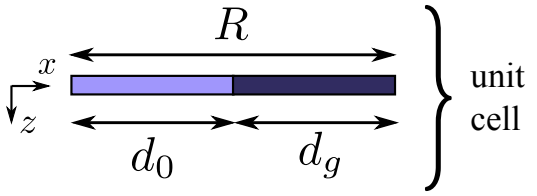


Figure 7.3: Unit cell of the strucured portrayed in figure 7.2 - side view.

Let us consider the unit cell of our periodic system, which may be divided into one region where graphene is absent, with width d_0, and another region of size d_g occupied by the graphene ribbon – see, for instance, figure 7.3. Then, the geometrical factor $s(x)$ can be written in terms of the Heaviside step function,

$$s(x) = \Theta(x - d_0) \ , \tag{7.30}$$

describing the sharp discontinuity in the conductivity. Hence, from equation (7.29) we obtain

$$\tilde{\sigma}_0 = \frac{\sigma_g}{R} \int_0^R \Theta(x - d_0) dx = \sigma_g \frac{d_g}{R} \ , \tag{7.31}$$

for the zero-th coefficient, and

$$\begin{aligned} \tilde{\sigma}_l &= \frac{\sigma_g}{R} \int_0^R \Theta(x - d_0) e^{-ilGx} dx \\ &= \frac{\sigma_g}{l\pi} \sin\left(l\pi d_g / R\right) e^{il\pi d_g / R} \ , \end{aligned} \tag{7.32}$$

for the l-th Fourier component ($l \neq 0$). Provided with the coefficients for the conductivity, we are now able to solve the linear system formed by equations (7.27) and (7.28). From the corresponding numerical solution, we then compute the transmittance, reflectance and absorbance of electromagnetic radiation through the structure using expressions (7.24)-(7.26). Figure 7.4 shows these quantities for different values of the damping parameter. The resulting spectra consist in a set of well-defined GSPs resonances, corresponding to different Bragg vectors (diffraction orders). These GSP-assisted effects yield

dramatic changes in the spectra when compared with the case of a pristine (unpatterned) graphene sheet. For instance, it is apparent from the figure that for a grating of graphene ribbons the absorbance at resonant frequencies is higher than in the case of a continuous graphene layer. As it shall

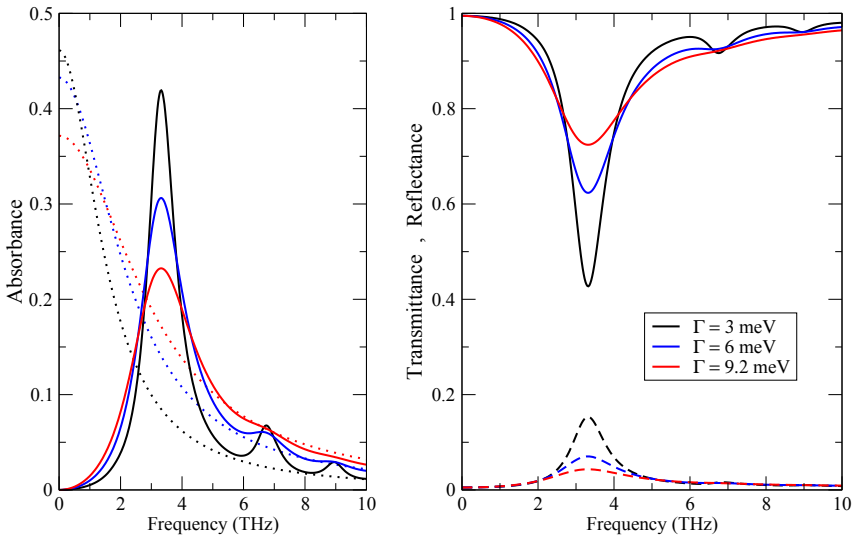


Figure 7.4: Absorbance, transmittance and reflectance of a p-polarized wave through a periodic structure of graphene ribbons for varying $\Gamma = \hbar\gamma$. Left panel: absorbance for a grid of graphene ribbons (continuous curve) and for uniform graphene (dotted curve). Right panel: transmittance (continuous) and reflectance (dashed curve). The remaining parameters are: $E_F = 0.45$ eV, $d_g = 4$ μm, $R = 8$ μm, $\epsilon_1 = 4$, $\epsilon_2 = 3$, $\theta = 0$ (normal incidence).

be clearer further ahead, this enhancement in absorbance corresponds to the coupling of electromagnetic radiation to Bloch GSPs modes – GSP-induced absorption. Additionally, notice that peaks in absorbance (and reflectance) go hand in hand with dips in transmittance. Also, not surprisingly, small values of Γ render sharp peaks in absorbance, with these becoming successively broader and less pronounced as Γ increases.

Let us now explore the dependence of the absorption spectra on the different parameters of the problem. We begin by studying how the GSPs resonances change with varying carrier density, n_e. The results are displayed

in figure 7.5. From the left panel, it is clear that for larger electronic densities, the resonances are stronger and shift towards higher frequencies. In order to be more quantitative, in the right panel of figure 7.5 we have plotted the GSP frequency (corresponding to the first resonance) as a function of the doping level, to which we have fitted a function of the type $f(n_e) \propto n_e^b$, having obtained $b = 0.249 \simeq 1/4$ for the exponent (fitting parameter)[6]. This

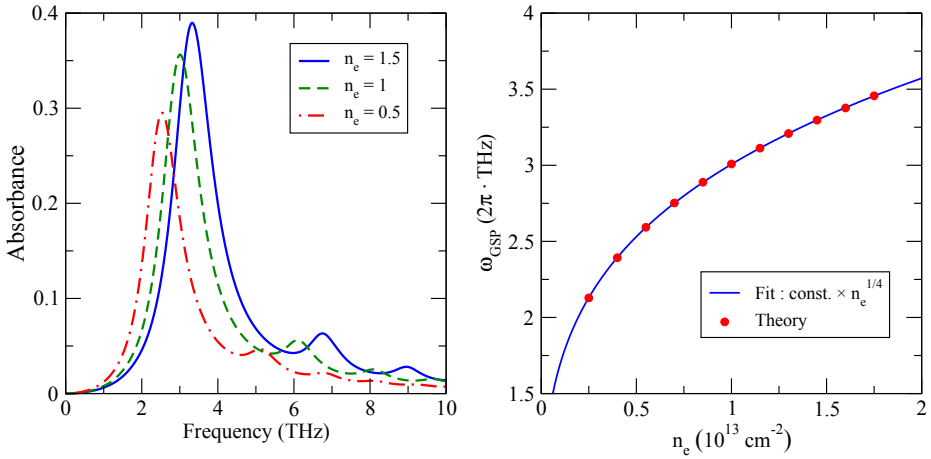


Figure 7.5: Dependence of the GSP frequency on the electronic density. Left panel: Absorbance spectrum for different values of n_e. Right panel: resonant frequencies – retrieved from our analytic theory (points) – for several values of n_e, and corresponding fitting function, $f(n_e) \propto n_e^b$ with $b = 0.249 \simeq 1/4$. Parameters: $\Gamma = 3.7$ meV, $d_g = 4$ μm, $R = 8$ μm, $\epsilon_1 = 4$, $\epsilon_2 = 3$, $\theta = 0$.

therefore demonstrates that the observed resonances scale with the density of charge carriers as

$$\omega_{\text{res}} \propto n_e^{1/4} \ , \tag{7.33}$$

which is a specific signature of GSPs. Furthermore, figure 7.6 (left panel) presents absorbance curves for arrays of graphene ribbons with different periods, R, while keeping the ratio $d_g/R = 0.5$ constant. Here, we observe a blueshift on the GSPs resonances for decreasing values of R. This can be understood by noting that the plasmon-polariton wavevector is approximately

[6]The fitting function was obtained using *Mathematica*'s built-in routines, which employ a least-squares method.

given by $q_{GSP} = (2m-1)\pi/d_g$, with $m = 1, 2, ...$, due to the symmetry of the incident field[7] [52, 53, 99]. Hence, the first, stronger resonance corresponds to the excitation of a localized plasmon with $q = \pi/d_g$, followed by a set of weaker higher-order peaks at higher frequencies, with $q = (2m-1)\pi/d_g$ for $m \geq 2$. Moreover, the panel at the right in figure 7.6 clearly demonstrates

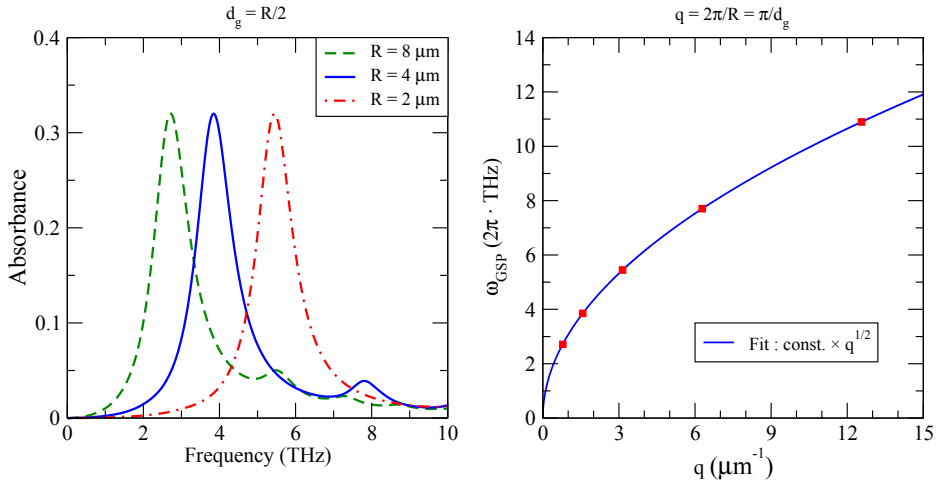


Figure 7.6: Dependence of the GSP frequency on the periodicity of the system and plasmon dispersion for the first resonance. Left panel: Absorbance spectrum for different values of grating period, R. Right panel: resonant frequencies – obtained using our analytic theory (squares) – as a function of the wavevector $q = 2\pi/R = \pi/d_g$ (fundamental plasmon mode); the curve represents the function fitting the data, namely $\omega_{GSP} \propto q^b$ with $b = 0.5001 \simeq 1/2$. Parameters: $d_g = R/2$, $E_F = 0.3$ eV, $\Gamma = 3.7$ meV, $\epsilon_1 = 4$, $\epsilon_2 = 3$, $\theta = 0$.

that the GSP resonances follow the $\sqrt{q}$ dispersion, in agreement with experimental results on plasmons in graphene ribbons [52, 53]. Note that this somewhat expected, since we have already shown in Chapter 4 that in the non-retarded regime (satisfied as long as $q \approx G \gg k$), we have

$$\hbar\omega_{GSP} \approx \sqrt{\frac{4\alpha}{\epsilon_1+\epsilon_2} E_F \hbar c q}\ , \tag{7.34}$$

for homogeneous graphene. In fact, as an exercise, let us consider the parameters corresponding to the blue curve in figure 7.6 to estimate the plasmon

[7] For a thorough discussion, please refer to section A.2 of Appendix A.

frequency via equation (7.34):

$$\hbar\omega_{GSP} \approx \sqrt{\frac{4}{137\times 7}0.3\times 0.2\times\frac{2\pi}{4}} \simeq 19.8 \text{ meV} \rightarrow 4.8 \text{ THz} \, . \tag{7.35}$$

Nonetheless, we find that this expression overestimates the GSP resonant frequency, since the fundamental mode in figure 7.6 appears at 3.9 THz instead. This should not come as a surprise, because in this situation the graphene plasmons are "dressed" by the grating; in other words, the relation (7.34) does not capture the details of the polaritonic bandstructure.

Finally, for the sake of completeness, we have summarized in figure 7.7 the effect of different filling factors, d_g/R, and varying incident angle, on the absorbance spectrum for an array of graphene ribbons. Notice that the

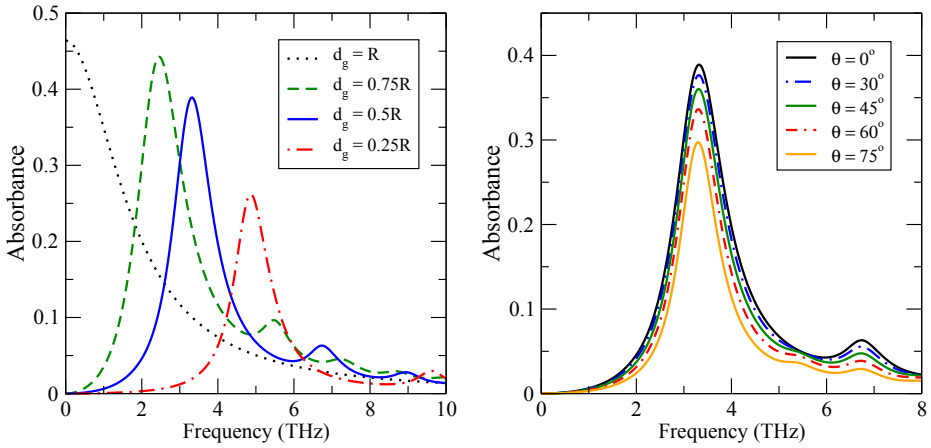


Figure 7.7: Left panel: Absorbance (at normal incidence) of a grid of graphene ribbons for different filling factors, d_g/R, with $R = 8$ μm; the black dotted line corresponds to the case of an unpatterned graphene sheet. Right panel: dependence on the incident angle, for fixed $R = d_g/2 = 8$ μm. The remaining parameters are: $E_F = 0.45$ eV, $\Gamma = 3.7$ meV, $\epsilon_1 = 4$, $\epsilon_2 = 3$.

plasmonic resonances undergo a redshift as the filling factor approaches unity. Here, the absorbance spectrum presents itself as a featureless Drude peak akin to Ohmic losses – dotted black curve. Further, larger d_g/R ratios attain higher absorbance values owing to the increase of the effective area covered by

graphene within the unit cell. With regards to the angle of incidence, figure 7.7 shows a weak dependence on this parameter, that being substantial only for large incident angles (i.e. at grazing incidence). Likewise, the position of the resonances remains essentially unchanged, inasmuch as $q = |k \sin\theta + nG| \approx |nG|$ (for odd integers n).

7.2.2 Theory *versus* experiment

So far we have covered virtually every aspect of our theoretical model: we set up the formalism and explored its results within a vast parameter space. In addition, we have demonstrated that our theory correctly describes the excitation of GSPs in graphene ribbons, yielding results consistent with those found in the literature [50, 52, 53, 55, 88]. Still, the ultimate test for any theory must be the direct comparison of its results against actual experimental data. With that in mind, here we will present several spectra computed under the same conditions found in the experiments performed by Ju *et al* [52]. This will show to what extent our theory is capable to account for the experimental results.

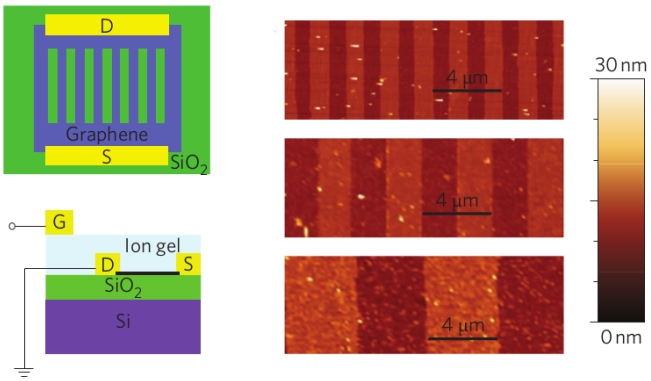
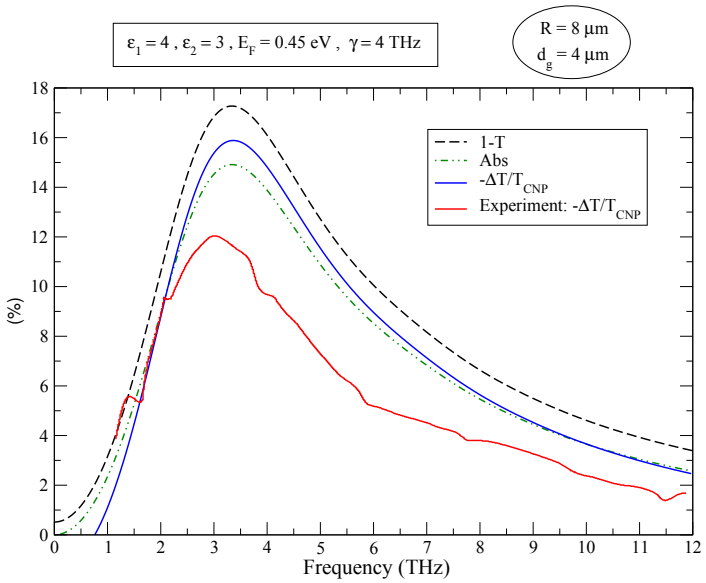


Figure 7.8: Left: illustration of the experimental setup, consisting in a periodic array of graphene micro-ribbons on a SiO_2/Si substrate. The carrier concentration can be controlled using an ion gel top gate. Right: AFM measurements of the fabricated samples, with $d_g = R/2 = 4$ μm, 2 μm and 1 μm. Adapted from Ref. [52].

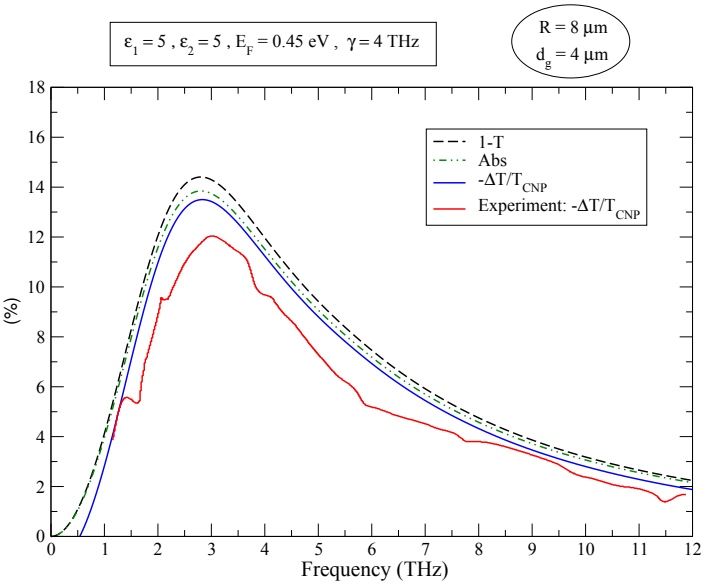
The experimental setup – consisting in a series of graphene micro-ribbons

in a grating-like configuration – is portrayed in figure 7.8, along with atomic force microscopy (AFM) images of the fabricated samples. As shown in the figure, these structures have widths of 4, 2 and 1 micrometers, and the ratio $d_g = 0.5R$ was kept constant. It should be noted that the spectra in Ref. [52] represent the change in transmittance relative to the one taken at the "charge neutral point" (CNP), that is $-\Delta T/T_{CNP}$ with $\Delta T = T - T_{CNP}$. At the CNP, the chemical potential, μ, is zero; thus, in order to effectively compare the theoretical results with the measured spectra, we must use the full expression for the conductivity of graphene, as given by Kubo's formula [cf. equations (2.35) and (2.36)]), since both conditions $|\mu| \gg k_B T$ and $2|\mu| > \hbar\omega$ break down at the CNP. Hereafter, we shall assume $T = 300$ K and a scattering rate of 4 THz, as indicated in the reference. Also, at this point it is worth to mention that GSPs can interact with surface optical (SO) phonons on polar substrates, such as SiO_2 or hBN [53, 85]. This can be modelled by describing their dielectric functions as Lorentz oscillators (instead of a real constants), using the respective SO phonon resonant frequencies. However, for graphene on SiO_2, plasmon-phonon hybridization is only important at frequencies $\omega \gtrsim \omega_{\text{sop}} \approx 24$ THz (lowest frequency mode), well above the frequency range contemplated in this work, thereby allowing us to safely set $\epsilon_{SiO_2} = 4$.

Let us first consider the sample with $d_g = 4$ μm. In figure 7.9a we compare the theoretical curves, obtained using parameters matching the experimental conditions (see caption for details), with experimental data extracted from Ref. [52]. For completeness, we have also plotted, along with the transmittance relative to the CNP, $-\Delta T/T_{CNP}$, the absorbance and extinction spectrum. The figure shows a rather good agreement between theory and experiment, with a prominent plasmon resonance around 3 THz. Explicitly, our calculations rendered $\omega_{GSP}^{\text{theo}} \approx 3.3$ THz, whereas the measured peak is centered at $\omega_{GSP}^{\text{exp}} \approx 3$ THz. Therefore, the only perceptible difference concerns the resonance strength, with theory predicting a peak value about 4 % higher. There are a couple of reasons that may contribute to this slight deviation. First, we note that our model assumes that both dielectrics are semi-infinite – we took $\epsilon_1 = 4$ (SiO_2) and $\epsilon_2 = 3$ (ion gel) –, neglecting the influence of the



(a) Results for $\epsilon_1 = 4$ (SiO_2) and $\epsilon_2 = 3$ (ion gel).



(b) Results obtained by adopting the effective medium approach with $\epsilon = 5$.

Figure 7.9: Transmittance change spectrum, $-\Delta T/T_{CNP} = 1 - T/T_{CNP}$, for an array of graphene micro-ribbons with width $d_g = 4$ μm (and period $R = 8$ μm): theory (blue curve) and experimental data (red curve) [52]. Also plotted are the extinction (1-T) and absorbance (Abs) spectra. As in the experiment, we take $\gamma = 4$ THz, $\theta = 0$ (normal incidence) and $n_e = 1.5 \times 10^{13}$ cm^{-2}, which corresponds to $E_F = \hbar v_F \sqrt{\pi n_e} \approx 0.45$ eV.

Si and also eventual multiple reflections within the finite-sized SiO_2 layer[8]. On the other hand, on the experimental side, the authors of the experiment described in Ref. [52] mention that there was a small part of the beam transmitted through unpatterned graphene in the outskirts of the structure, adding a small background contribution owing to free carrier absorption. The authors state that this extra-contribution was subtracted from the measured data, based on fittings from numerical calculations employing finite element analysis. However, the degree of fidelity of this procedure remains unclear, and perhaps it may have overestimated (or not) the contribution from free carrier absorption. Furthermore, the above-mentioned computational simulations suggested that an effective dielectric environment with $\epsilon = 5$ could be used in order to account for the electromagnetic properties of the different dielectrics[9]. The results corresponding to this case are presented in figure 7.9b, in an attempt to encompass not only the effects of the heterogeneous SiO_2/Si substrate, but also the intricate nature of the optical constants of ion liquids [100]. The figure clearly shows a fair improvement with respect to the previous case (which was already quite good), demonstrating an excellent agreement between our analytical results and experimental data.

Finally, the spectrum of the normalized[10] change in transmittance relative to the CNP, for the different micro-ribbon widths considered in the experimental work, is depicted in figure 7.10. Once again, we have assumed $\epsilon = 5$ in our calculations[11]. The figure provides further evidence of the outstanding agreement between theory (dashed curves) and experiment (continuous curves), with the former following closely the experimental data. The mea-

[8]Taking $q_{GSP} \approx \pi/d_g$, we can estimate the penetration in the dielectrics, in the non-retarded regime, as $\zeta = \Re\{\kappa\}^{-1} \sim q^{-1} \approx 1$ μm. This is about three times larger than thickness of the SiO_2 layer, so that some influence due to the Si part of the substrate is to be expected.

[9]This seems to be reasonable, given that the dielectric constants of ion gel, SiO_2 and Si are 2-4 [100], 4 and 11 [75], respectively (in the THz spectral range).

[10]Although the spectra are normalized, as presented in Ref. [52], we expect a similar behaviour as in figure 7.9b.

[11]In addition, we note that in figure 7.10 we have used $v_F \approx 1.1 \times 10^6$ m/s, as extracted from experimental data taken from Ref. [52], to determine the Fermi energy from the carrier concentration, n_e. This value for the velocity of massless Dirac fermions is reported elsewhere [78], and is a signature of band renormalization owing to many-body interactions [101].

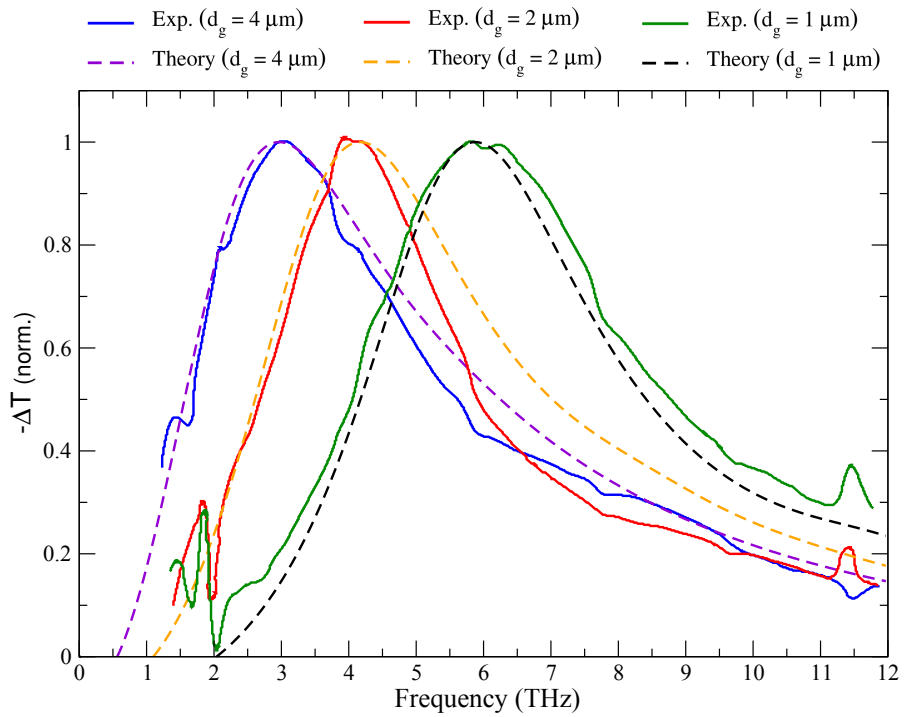


Figure 7.10: Normalized spectra of $-\Delta T$ for arrays of ribbons with different widths: 4, 2 and 1 μm. The computed analytical (dashed) curves are superimposed to the spectra obtained experimentally (continuous curves) for adequate comparison. We adopted $\epsilon = 5$, with the remaining parameters matching the conditions of the experiment, namely $\gamma = 4$ THz, $\theta = 0$ and $n_e = 1.5 \times 10^{13}$ cm^{-2} $\Rightarrow E_F = \hbar v_F \sqrt{\pi n_e} \approx 0.497$ eV (with $v_F = 1.1 \times 10^6$ m/s).

sured (computed) GSPs resonant frequencies are at 3 (2.9), 4.1 (4) and 6 (5.6) THz for arrays with ribbon widths of 4, 2 and 1 μm, respectively, exhibiting the predicted $\omega_{GSP} \propto d_g^{-1}$ scaling behaviour.

Our results and subsequent analysis testify the ability of our analytical theory to explain the experimental results, without the need to use lengthy, computationally demanding full-wave numerical simulations based either on finite element methods or FDTD. Moreover, the theoretical framework developed over this Chapter constitutes a promising playground for engineering plasmonic micro/nanostructures and metamaterials with tailored plasmonics

properties, taking advantage of graphene's tunability and strong light-matter interactions. We expect an even stronger GSP-induced absorption for samples with lower electron scattering rates, which will eventually become available with the continuous improvement of fabrication techniques.

Chapter 8

Concluding Remarks

In the present thesis, we have covered several important aspects of the emerging field of graphene plasmonics.

We started by reviewing the basic properties of SPPs sustained at dielectric-metal interfaces, setting the stage for the discussion of SPPs in doped graphene. We then derived the dispersion relation of SPP in graphene, both in single-layer graphene and double-layer graphene. We have seen that even for these simple geometries, the spectrum needs to be obtained by numerical means. From the corresponding solutions, it was clear that GSP-excitation is not feasible by simply striking light directly on graphene, since the dispersion curve always lies to the right of the light line. Therefore, in Chapter 5 we have gave examples of the most popular methods to couple three dimensional light beams with GSPs.

Motivated by a recent experiment reporting the excitation of GSPs using a metallic antenna [94], in Chapter 6 we have conducted a theoretical study on a similar system consisting in an infinitely long, highly conducting metal stripe placed on top of a graphene layer. Resonant excitation of GSPs was achieved whenever the ribbon width coincided with an odd multiple of half wavelengths (of the incident radiation), yielding subwavelength confinements of the order of $\lambda_p = 0.052\lambda_0$.

Finally, in Chapter 7 we developed a general theoretical framework for describing the excitation of GSPs in systems where the graphene's conductiv-

ity is periodically modulated. In particular, we have employed our analytical model to the case of a periodic array of graphene ribbons, since this setup has been extensively studied experimentally. We then confronted our theoretical results against experimental data [52], having observed an outstanding agreement between theory and experiment, thereby validating the model.

Appendix A

Supplementary Material for Chapter 7

A.1 Derivation of the expressions for the transmittance and reflectance

In Chapter 7, subsection 7.1.2, we claimed that the expressions for the transmittance and reflectance in terms of the electric-field amplitudes were given by equations (7.24) and (7.25), respectively. In what follows, we shall present a detailed derivation for these, as they constitute important physical quantities for the problem under consideration in the above-mentioned Chapter. With that end, we introduce the Poynting vector (for non-magnetic media)

$$\mathbf{S} = \frac{1}{\mu_0}\mathbf{E} \times \mathbf{B} \ , \tag{A.1}$$

which describes the flux of electromagnetic energy per unit area. Assuming that both $\mathbf{E}$ and $\mathbf{B}$ can be written in terms of harmonic functions, $e^{-i\omega t}$, one may write the time-averaged Poynting vector as

$$\langle \mathbf{S} \rangle_t = \frac{1}{2\mu_0} \Re \left\{ \mathbf{E} \times \mathbf{B}^* \right\} \ , \tag{A.2}$$

which for a TM wave polarized in the xz-plane reads

$$\langle \mathbf{S} \rangle_t = \frac{1}{2\mu_0} \Re \left\{ E_x B_y^* \hat{\mathbf{z}} - E_z B_y^* \hat{\mathbf{x}} \right\} \ . \tag{A.3}$$

Thus, for the incident wave, we obtain

$$\langle S_z \rangle_t^{\text{inc}} \equiv S_z^{inc} = \frac{\omega \epsilon_2 \epsilon_0}{2k_z} |E_x^{inc}|^2 \ , \tag{A.4}$$

along the z-direction. Similarly, for the reflected and transmitted waves corresponding to n-th diffraction order, we have[1]

$$\langle S_{z,n} \rangle_t^{\text{ref}} \equiv S_{z,n}^{(2)} = -\frac{\omega \epsilon_2 \epsilon_0}{2|\kappa_{2,n}|} |E_{x,n}^{(2)}|^2 \ , \tag{A.5}$$

and

$$\langle S_{z,n} \rangle_t^{\text{trans}} \equiv S_{z,n}^{(1)} = \frac{\omega \epsilon_1 \epsilon_0}{2|\kappa_{1,n}|} |E_{x,n}^{(1)}|^2 \ , \tag{A.6}$$

respectively. We note that in writing equations (A.5) and (A.6) we have assumed that $\kappa_{j,n}$ is purely imaginary, i.e. only propagating waves should be considered. For real $\kappa_{j,n}$, we get $S_{z,n}^{(1)} = S_{z,n}^{(2)} = 0$, meaning that that particular diffraction order carries no energy (along $\hat{\mathbf{z}}$) as expected for evanescent waves. Having obtained equations (A.4)-(A.6), we are now able to compute the reflectance

$$\mathcal{R}_n = \left| \frac{S_{z,n}^{(2)}}{S_z^{inc}} \right| = \frac{k_z}{|\kappa_{2,n}|} |r_n|^2 \ , \tag{A.7}$$

and transmittance

$$\mathcal{T}_n = \left| \frac{S_{z,n}^{(1)}}{S_z^{inc}} \right| = \frac{\epsilon_1}{\epsilon_2} \frac{k_z}{|\kappa_{1,n}|} |t_n|^2 \ , \tag{A.8}$$

[1]Notice the minus sign in the expression for the reflected waves, indicating a power flow along the negative z-direction. Conversely, the transmitted waves carry energy in the positive direction along the z-axis.

for each n-th wave, where we have introduced the corresponding reflection and transmission amplitudes, given by

$$r_n = \frac{E^{(2)}_{x,n}}{E^{inc}_x} \ , \tag{A.9}$$

$$t_n = \frac{E^{(1)}_{x,n}}{E^{inc}_x} \ , \tag{A.10}$$

respectively. Therefore, we have demonstrated that equations (A.7) and (A.8) are equivalent to the relations (7.25) and (7.24) presented in subsection 7.1.2.

As previously mentioned, only diffraction orders corresponding to propagating modes should be included in the sums figuring in equations (7.25) and (7.24). In particular, it is worth pointing out that for the parameters chosen in this work, we have found that solely the specular ($n = 0$) reflectance and transmittance represent propagating modes; these read

$$\mathcal{R}_0 = |r_0|^2 \ , \tag{A.11}$$

$$\mathcal{T}_0 = \frac{\epsilon_1}{\epsilon_2} \frac{\cos\theta}{\sqrt{\epsilon_1/\epsilon_2 - \sin^2\theta}} |t_0|^2 \ , \tag{A.12}$$

with the latter being valid only for $\epsilon_1 > \epsilon_2$ or $\theta < \theta_c = \arcsin\left(\sqrt{\epsilon_1/\epsilon_2}\right)$.

A.2 A closer look on the modes contributing to each one of the resonances

We have seen in section 7.2 that the absorbance spectrum for a grating of graphene ribbons displays a prominent peak accompanied by a set of weaker, higher-order resonances. Here, we shall restrict ourselves to the case where $d_g = R/2$ (and $\theta = 0$), as this is the configuration considered in experiments so far [52, 53, 54]. From the symmetry point of view, and using previous knowledge of the electromagnetic response (within the quasi-static limit) of a two-dimensional metallic stripe, we expect that only modes corresponding

to $q \approx |nG| = n\pi/d_g$ with $n = 1, 3, 5, ...$ will couple significantly to GSPs, due to the symmetry of the incident field, i.e. $\mathbf{E}^{inc} = E_x^{inc}\hat{\mathbf{x}} = \text{const.}$ [99]. In order to investigate how each one of the harmonics contribute to a particular resonance in this more complex geometry, we show in figure A.1 the amplitude squared for the modes corresponding to $n = \pm 1, \pm 2, ..., \pm 5$. First, we note

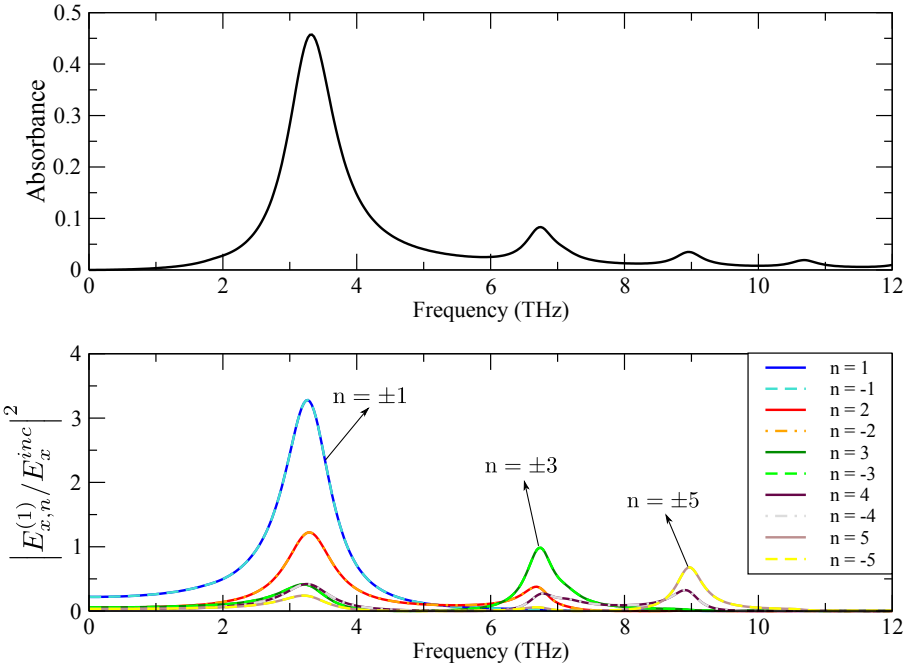


Figure A.1: Modulus squared of the amplitudes, $\left|E_{x,n}^{(1)}/E_x^{inc}\right|^2$, for modes with $n = \pm 1, \pm 2, \pm 3, \pm 4, \pm 5$. These illustrate the relative contribution of different harmonics to the observed resonances (bottom panel). The top panel shows the respective absorbance spectrum. We have used the following parameters: $R = d_g/2 = 8$ μm, $E_F = 0.45$ eV, $\Gamma = 2$ meV, $\epsilon_1 = 4$, $\epsilon_2 = 3$, $\theta = 0$.

that the spectral weights associated with different harmonics are located at the resonant frequencies which show up in the absorbance spectrum. More importantly, however, is that only certain modes contribute significantly to a specific peak. For instance, it is apparent from the figure that the major contributions to the first three resonances come from the (odd) harmonics $n = \pm 1, \pm 3, \pm 5$, as indicated in the figure by the arrows. In comparison, the even modes have much smaller spectral weights. Also, notice that there is no

peak associated with $n = \pm 2$ between the ones corresponding (essentially) to $n = \pm 1$ and ± 3. Finally, we note that only modes with $|n| \geq 6$ will contribute to the last resonance visible in figure A.1 (top panel).

Thus, all of the above suggests that it is indeed reasonable to assign the wavevector $q \approx (2m-1)\pi/d_g$ with $m = 1, 3, 5, ...$ to the m-th GSP resonance.

Bibliography

[1] A. Sommerfeld. *Über die Fortpflanzung elektrodynamischer Wellen an längs eines Drahtes.* Ann. der Physik und Chemie, **67**:pp. 233–290, 1899.

[2] J. Zenneck. *Uber die Fortpflanztmg ebener elektro-magnetischer Wellen langs einer ebenen Leiterflache und ihre Beziehung zur drahtlosen Telegraphie.* Annalen der Physik, **23**:pp. 846–866, 1907.

[3] R. W. Wood. *On a remarkable case of uneven distribution of light in a diffraction grating spectrum.* Philosophical Magazine, **4**:pp. 396–402, 1902.

[4] Lord Rayleigh. *On the Dynamical Theory of Gratings.* Proc. R. Soc. Lond. A, **79**:pp. 399–416, 1907.

[5] U. Fano. *The Theory of Anomalous Diffraction Gratings and of Quasi-Stationary Waves on Metallic Surfaces (Sommerfeld's Waves).* J. Opt. Soc. Am., **31**:pp. 213–222, 1941.

[6] S. Enoch and N. Bonod (editors). *Plasmonics: From Basics to Advanced Topics.* Springer Series in Optical Sciences, New York, 2012.

[7] A. Hessel and A. A. Oliner. *A New Theory of Wood's Anomalies on Optical Gratings.* Applied Optics, **4**:pp. 1275–1297, 1965.

[8] R. H Ritchie *et al. Surface-Plasmon Resonance Effect in Grating Diffraction.* Phys. Rev. Lett., **21**:pp. 1530–1533, 1968.

[9] C. J. Powell and J. B. Swan. Origin of the characteristic electron energy losses in aluminum. *Phys. Rev.*, **115**:869, 1959.

[10] R. H. Ritchie. Plasma losses by fast electrons in thin films. *Phys. Rev.*, **106**:874, 1957.

[11] E. Kretschmann and H. Raether. *Radiative decay of nonradiative surface plasmon excited by light.* Z. Naturf. A, **23**:pp. 2135–2136, 1968.

[12] A. Otto. *Excitation of nonradiative surface plasma waves in silver by the method of frustrated total reflection.* Z. Phys., **216**:pp. 398–410, 1968.

[13] J. R. Sambles, G. W. Bradberya, and F. Yang. *Optical excitation of surface plasmons: An introduction.* Contemporary Physics, **32**:pp. 173–183, 1991.

[14] T. W. Ebbesen *et al. Extraordinary optical transmission through subwavelength hole arrays.* Nature, **391**:pp. 667–669, 1998.

[15] L. Martín-Moreno *et al. Theory of Extraordinary Optical Transmission through Subwavelength Hole Arrays.* Phys. Rev. Lett., **86**:1114, 2001.

[16] Stefan A. Maier. *Plasmonics: Fundamentals and Applications.* Springer, New York, 2007.

[17] William L. Barnes, Alain Dereux, and Thomas W. Ebbesen. *Surface plasmon subwavelength optics.* Nature, **424**:pp. 824–830, 2003.

[18] William L. Barnes. *Surface plasmon–polariton length scales: a route to sub-wavelength optics.* J. Opt. A: Pure Appl. Opt., **8**:S87, 2006.

[19] A. V. Kabashin *et al. Plasmonic nanorod metamaterials for biosensing.* Nature Materials, **8**:pp. 867 – 871, 2009.

[20] Y. Liua and X. Zhang. *Metamaterials: a new frontier of science and technology.* Chem. Soc. Rev., **40**:pp. 2494–2507, 2011.

[21] Lee Billings. *Exotic optics: Metamaterial world.* Nature, **500**:pp. 138–140, 2013.

[22] Ekmel Ozbay. *Plasmonics: Merging Photonics and Electronics at Nanoscale Dimensions.* Science, **311**:pp. 189–193, 2006.

[23] Alexandre G. Brolo. *Plasmonics for future biosensors.* Nature Photonics, **6**:pp. 709–713, 2012.

[24] A. J. Haes *et al. Plasmonic Materials for Surface-Enhanced Sensing and Spectroscopy.* MRS Bulletin, **30**:pp. 368–375, 2005.

[25] P. J. Reece. *Plasmonics: Finer optical tweezers.* Nature Photonics, **2**:pp. 333–334, 2008.

[26] M. L. Juan, M. Righini, and R. Quidant. *Plasmon nano-optical tweezers.* Nature Photonics, **5**:pp. 349–356, 2011.

[27] M. A. Green and S. Pillai. *Harnessing plasmonics for solar cells.* Nature Photonics, **6**:pp. 130–132, 2012.

[28] S. V. Boriskina, H. Ghasemi, and G. Chen. *Plasmonic materials for energy: From physics to applications.* Materials Today, **16**:pp. 375–386, 2013.

[29] S. S. Aćimović *et al. LSPR Chip for Parallel, Rapid, and Sensitive Detection of Cancer Markers in Serum.* Nano Lett., **14**:pp. 2636–2641, 2014.

[30] Y. B. Zheng *et al. Molecular plasmonics for biology and nanomedicine.* Nanomedicine, **7**:pp. 51–770, 201.

[31] Tuan Vo-Dinh *et al. Plasmonic nanoprobes: from chemical sensing to medical diagnostics and therapy.* Nanoscale, **5**:pp. 10127–10140, 2013.

[32] P. Berini and I. De Leon. *Surface plasmon–polariton amplifiers and lasers.* Nature Photonics, **6**:pp. 16–24, 2012.

[33] Ren-Min Ma *et al.* *Plasmon lasers: coherent light source at molecular scales.* Laser Photon. Rev., **7**:pp. 1–21, 2013.

[34] A. Archambault *et al.* *Surface plasmon Fourier optics.* Phys. Rev. B, **79**:195414, 2009.

[35] P. A. Huidobro *et al.* *Transformation Optics for Plasmonics.* Nano Lett., **10**:pp. 1985–1990, 2010.

[36] K. F. MacDonald *et al.* *Ultrafast active plasmonics.* Nature Photonics, **3**:pp. 55–58, 2009.

[37] M. Kauranen and A. V. Zayats. *Nonlinear plasmonics.* Nature Photonics, **6**:pp. 737–748, 2012.

[38] M. S. Tame *et al.* *Quantum plasmonics.* Nature Physics, **9**:pp. 329–340, 2013.

[39] Z. Jacob and V. M. Shalaev. *Plasmonics Goes Quantum.* Science, **28**:pp. 463–464, 2011.

[40] D. E. Chang *et al.* *Quantum Optics with Surface Plasmons.* Phys. Rev. Lett., **97**:53002, 2006.

[41] R. W. Heeres, L. P. Kouwenhoven, and V. Zwiller. *Quantum interference in plasmonic circuits.* Nature Nanotechnology, **8**:pp. 719–722, 2013.

[42] J. S. Fakonas *et al.* *Two-plasmon quantum interference.* Nature Photonics, **8**:pp. 317–320, 2014.

[43] G. Di Martino *et al.* *Observation of Quantum Interference in the Plasmonic Hong-Ou-Mandel Effect.* Phys. Rev. Applied, **1**:034004, 2014.

[44] Y.-J. Cai *et al.* *High-Visibility On-Chip Quantum Interference of Single Surface Plasmons.* Phys. Rev. Applied, **2**:014004, 2014.

[45] A. N. Grigorenko, M. Polini, and K. S. Novoselov. *Graphene plasmonics.* Nature Photonics, **6**:pp. 749–758, 2012.

[46] K. S. Novoselov *et al. Electric Field Effect in Atomically Thin Carbon Films.* Science, **306**:pp. 666–669, 2004.

[47] A. K. Geim. *Graphene: Status and Prospects.* Science, **324**:pp. 1530–1534, 2009.

[48] A. H. Castro Neto, F. Guinea, N. M. R. Peres, K. S. Novoselov, and A. K. Geim. *The electronic properties of graphene.* Rev. Mod. Phys., **81**, 2009.

[49] M. Jablan, H. Buljan, and M. Soljačić. *Plasmonics in graphene at infrared frequencies.* Phys. Rev. B, **80**:245435, 2009.

[50] Yu. V. Bludov, A. Ferreira, N. M. R. Peres, and M. I. Vasilevskiy. A primer on surface plasmon-polaritons in graphene. *Int. J. Mod. Phys. B*, **27**:1341001, 2013.

[51] M. Jablan, M. Soljačić, and H. Buljan. *Plasmons in Graphene: Fundamental Properties and Potential Applications.* Proc. IEEE, **101**:pp. 1689 – 1704, 2013.

[52] L. Ju *et al. Graphene plasmonics for tunable terahertz metamaterials.* Nature Nanotechnology, **6**:pp. 630–634, 2011.

[53] H. Yan *et al. Damping pathways of mid-infrared plasmons in graphene nanostructures.* Nature Photonics, **7**:pp. 394–399, 2013.

[54] Jared H. Strait *et al. Confined plasmons in graphene microstructures: Experiments and theory.* Phys. Rev. B, **87**:241410(R), 2013.

[55] F. Javier García de Abajo. *Graphene Plasmonics: Challenges and Opportunities.* ACS Photonics, **1**:pp. 135–152, 2014.

[56] S. A. Mikhailov and K. Ziegler. *New Electromagnetic Mode in Graphene.* Phys. Rev. B, **99**:016803, 2007.

[57] Daniel M. Mittleman. *Frontiers in terahertz sources and plasmonics.* Nature Photonics, **7**:pp. 666–669, 2013.

[58] P. Tassin, T. Koschny, and C. M. Soukoulis. *Graphene for Terahertz Applications*. Science, **341**:pp. 620–621, 2013.

[59] T. Lowand P. Avouris. *Graphene Plasmonics for Terahertz to Mid-Infrared Applications*. ACS Nano, **8**:pp. 1086–1101, 2014.

[60] J. Clerk Maxwell. *A Dynamical Theory of the Electromagnetic Field*. Philosophical Transactions of the Royal Society of London, **155**:pp. 459–512, 1865 (following a presentation to the Royal Society in December, 1864).

[61] Steven Weinberg. *The Quantum Theory of Fields, Vols. 1, 2 and 3*. Cambridge University Press, New York, 1996.

[62] John David Jackson. *Classical Electrodynamics*. Wiley, New York, 3rd. edition edition, 1998.

[63] P. Drude. *Zur Elektronentheorie der Metalle*. Annalen der Physik, **306**:pp. 566–613, 1990.

[64] N. W. Ashcroft and N. D. Mermin. *Solid State Physics*. Saunders College, New York, 1st edition edition, 1976.

[65] Changgu Lee, Xiaoding Wei, Jeffrey W. Kysar, and James Hone. *Measurement of the Elastic Properties and Intrinsic Strength of Monolayer Graphene*. Science, **321**(5887):pp. 385–388, 2008.

[66] Alexander A. Balandin *et al. Superior Thermal Conductivity of Single-Layer Graphene*. Nano Lett., **8**:pp. 902–907, 2008.

[67] K. I. Bolotin *et al. Ultrahigh electron mobility in suspended graphene*. Solid State Communications, **146**:pp. 351–355, 2008.

[68] N. M. R. Peres. *Colloquium: The transport properties of graphene: An introduction*. Rev. Mod. Phys., **82**, 2010.

[69] L. A. Falkovsky and A. A. Varlamov. *Space-time dispersion of graphene conductivity*. Eur. Phys. J. B, **56**:pp. 281–284, 2007.

[70] L. A. Falkovsky. *Optical properties of graphene.* Journal of Physics: Conference Series, **129**:012004, 2008.

[71] T. Stauber, N. M. R. Peres, and A. K. Geim. *Optical conductivity of graphene in the visible region of the spectrum.* Phys. Rev. B, **78**:085432, 2008.

[72] B. Wunsch, T. Stauber, F. Sols, and F. Guinea. *Dynamical polarization of graphene at finite doping.* New J. Phys., **8**:318, 2006.

[73] V. P. Gusynin, S. G. Sharapov, and J. P. Carbotte. *On the universal ac optical background in graphene.* New J. Phys., **11**:095013, 2009.

[74] P. B. Johnson and R. W. Christy. *Optical Constants of the Noble Metals.* Phys. Rev. B, **6**:pp. 4370–4379, 1972.

[75] Edward D. Palik. *Handbook of Optical Constants of Solids.* Academic Press, 1st edition, 1997.

[76] J. A. Dionne, L. A. Sweatlock, H. A. Atwater, and A. Polman. *Planar metal plasmon waveguides: frequency-dependent dispersion, propagation, localization, and loss beyond the free electron model.* Phys. Rev. B, **72**:075405, 2005.

[77] R. B. Pettit *et al. Measurement of surface-plasmon dispersion in oxydized aluminum films.* Phys. Rev. B, **8**:3116, 1975.

[78] Z. Q. Li *et al. Dirac charge dynamics in graphene by infrared spectroscopy.* Nature Physics, **4**:pp. 532–535, 2008.

[79] Frank Stern. *Polarizability of a Two-Dimensional Electron Gas.* Phys. Rev. Lett., **18**:546, 1967.

[80] A. N. Grigorenko, M. Polini, and K. S. Novoselov. *Graphene plasmonics.* Nature Photonics, **6**:pp. 749–758, 2012.

[81] Tobias Stauber. *Plasmonics in Dirac systems: from graphene to topological insulators.* J. Phys.: Condens. Matter, **26**:123201, 2014.

[82] Chandra S. R. Kaipa *et al.* *Enhanced transmission with a graphene-dielectric microstructure at low-terahertz frequencies.* Phys. Rev. B, **85**:245407, 2012.

[83] T. Zhan *et al.* *Transfer matrix method for optics in graphene layers.* J. Phys.: Condens. Matter, **25**:215301, 2013.

[84] J. J. Zhu, S. M. Badalyan, and F. M. Peeters. *Plasmonic excitations in Coulomb-coupled N-layer graphene structures.* Phys. Rev. B, **8**:085401, 2013.

[85] Victor W. Brar *et al.* *Hybrid Surface-Phonon-Plasmon Polariton Modes in Graphene/Monolayer h-BN Heterostructures.* Nano Lett., **14**(7):pp. 3876–3880, 2014.

[86] Yu. V. Bludov, N. M. R. Peres, and Mikhail I. Vasilevskiy. Graphene-based polaritonic crystal. *Phys. Rev. B*, **85**:245409, 2012.

[87] N. M. R. Peres *et al.* Exact solution for square-wave grating covered with graphene: surface plasmon-polaritons in the terahertz range. *J. Phys.: Condens. Matter*, **25**:125303, 2013.

[88] A. Yu. Nikitin, F. Guinea, F. J. Garcia-Vidal, and L. Martin-Moreno. *Surface plasmon enhanced absorption and suppressed transmission in periodic arrays of graphene ribbons.* Phys. Rev. B, **85**:081405(R), 2012.

[89] Z. Fei *et al.* Gate-tuning of graphene plasmons revealed by infrared nano-imaging. *Nature*, **487**:pp. 82–85, 2012.

[90] J. Chen *et al.* Optical nano-imaging of gate-tunable graphene plasmons. *Nature*, **487**:pp. 77–81, 2012.

[91] Y. Y. Teng and E. A. Stern. Plasma radiation from metal grating surfaces. *Phys. Rev. Lett.*, **19**:511, 1967.

[92] H. Raether. *Surface Plasmons on Smooth and Rough Surfaces and on Gratings.* Springer Tracts in Modern Physics, New York, 1st edition edition, 1988.

[93] A. V. Zayats *et al.* *Nano-optics of surface plasmon polaritons.* Physics Reports, **408**:pp. 131–314, 2005.

[94] P. Alonso-González *et al.* Controlling graphene plasmons with resonant metal antennas and spatial conductivity patterns. *Science*, **344** (6190):pp. 1369–1373, 2014.

[95] A. Satou and S. A. Mikhailov. Excitation of two-dimensional plasmon polaritons by an incident electromagnetic wave at a contact. *Phys. Rev. B*, **75**:045328, 2007.

[96] T. M. Slipchenko *et al.* Analytical solution for the diffraction of an electromagnetic wave by a graphene grating. *J. Opt.*, **15**:114008, 2013.

[97] N. M. R. Peres *et al.* Light scattering by a medium with a spatially modulated optical conductivity: the case of graphene. *J. Phys.: Condens. Matter*, **24**:245303, 2012.

[98] Sukosin Thongrattanasiri, Alejandro Manjavacas, and F. Javier García de Abajo. Quantum finite-size effects in graphene plasmons. *ACS Nano*, **6**:pp. 1766–1775, 2012.

[99] S. A. Mikhailov and N. A. Savostianova. Microwave response of a two-dimensional electron stripe. *Phys. Rev. B*, **71**:035320, 2005.

[100] Kohji Yamamoto, Masahiko Tani, and Masanori Hangyo. *Terahertz Time-Domain Spectroscopy of Imidazolium Ionic Liquids.* J. Phys. Chem. B, **111**:pp. 4854–4859, 2007.

[101] Valeri N. Kotov *et al.* *Electron-Electron Interactions in Graphene: Current Status and Perspectives.* Rev. Mod. Phys., **84**:1067, 2012.